DETECTION OF NONDETERMINISTIC LINEAR CHIRPS IN NON-GAUSSIAN NOISE BACKGROUND

by

Mohamed Abou Bakr Othman

A dissertation submitted to the faculty of
The University of Utah
in partial fulfillment of the requirements for the degree of

Doctor of Philosophy

Department of Electrical and Computer Engineering

The University of Utah

December 2014

The University of Utah Graduate School

STATEMENT OF DISSERTATION APPROVAL

The dissertation of   **Mohamed Abou Bakr Othman**

has been approved by the following supervisory committee members:

Behrouz Farhang Boroujeny	, Chair	**8/27/2014**
		Date Approved
John Belz	, Member	
		Date Approved
Neal Patwari	, Member	**8/27/2014**
		Date Approved
Rong-Rong Chen	, Member	**8/27/2014**
		Date Approved
Thomas Schmid	, Member	
		Date Approved

and by   **Gianluca Lazzi**   , Chair/Dean of

the Department/College/School of   **Electrical and Computer Engineering**

and by David B. Kieda, Dean of The Graduate School.

ABSTRACT

Chirp signals arise in many applications of digital signal processing. In this dissertation, we address the problem of detection of chirp signals that are encountered in a bistatic radar which we are developing for remote sensing of cosmic ray induced air showers. The received echoes from the air showers are characterized by their large Doppler shift (several tens of MHz), and very short sweep period ($\sim 10 \ \mu s$). This makes our astrophysical problem a challenging one, since a very short sweep period is equivalent to a very low energy chirp signal. Furthermore, the related parameters of the received echoes are nondeterministic since they are tied to the physical parameters of the air showers that are stochastic in nature. In addition, our problem is characterized by the rarity of the expected chirp-echoes to be received, few events per week, and thus, background noise reception is the case most of the time. The primary focus of this research is to address these challenges and find an optimized detection approach under the existing receiver environment which contains non-Gaussian noise and is characterized by low signal-to-noise ratio (SNR).

Matched filters are commonly used in radar systems when the chirp signal is known. In our first method, we revisit this context and use a matched filter as a basis of building a rake-like receiver that consists of a set of filters matched to quantized chirp rates, logarithmically distributed within the chirp-rate interval of interest. We examine the detection capability of the proposed structure through extensive theoretical and numerical analysis. Theoretical analysis and simulation results prove that the proposed detector has high detection capability for a range of chirp slopes in a low SNR environment.

A major source of false-alarms was found to be due to sudden noise spikes that cover wide frequency bands. These transient signals have high amplitudes and occur at random time instants. This leads to erroneous detection decision. We study the influence of amplitude limiting the noisy signal on reducing the received false-alarms and enhancing the detection performance of the proposed rake-like receiver.

In our second method, we use Hough transform (HT), which is widely used in the area of image processing for the purpose of finding parameterized patterns, as a basis of building a robust detection technique. We examine the detection capability of the proposed structure

through theoretical and numerical analysis. Our results prove that the proposed detector has high detection capability for a range of chirp slopes in a low SNR environment.

The introduced detection algorithms are implemented over a Virtex-5 FPGA. National Instruments modules are used as a high-performance custom hardware. Due to rarity of received echoes, we emulate the expected radar echoes to evaluate the system performance. The detection performance of the emulated echoes is examined using the implemented receiver at the field. Also, we compare the performance of both detectors.

CONTENTS

LIST OF FIGURES

ix

LIST OF TABLES

ACKNOWLEDGMENTS

I am also thankful to the University of Utah for giving my the opportunity to experience the best learning processes and interesting courses.

Last but not least, I would like to thank my family for all their love and encouragement. I owe a dept of heartfelt gratitude to my parents, Abou Bakr and Maha, and sisters, Rehab and Aya, for their continuous encouragement, constant prayers and ultimate support. Thanks to my parents for raising me, for sharing my moments of triumph, for bearing with me during challenges, and for never losing confidence in me. Both sacrificed quite a lot to get me to this point in my education and life. Thanks to my amazing father for shaping my personality and leading by example in all life aspects. He has always offered the best wisdom and advice, and I can't imagine where I would be without him. Thanks to my loving mother, my best friend, for her continuous support and encouragement in all my pursuits. I can't express my gratitude for her in words, whose unconditional love has been my greatest strength. For this and much more, I dedicate this dissertation to them.

CHAPTER 1

INTRODUCTION

1.1 Background and Motivation

The study of high energy cosmic rays is a very important and challenging physical problem. It is considered to be a major step forward in understanding the fundamental nature of the universe [1]. The term "cosmic rays" is given to high energetic particles of extra-terrestrial origin, that continually strike the Earth's atmosphere. Cosmic rays can have energies of over 10^{18}eV, which is much higher than the energy produced by terrestrial particle accelerators. The source of these particles yet remains an interesting mystery to be solved. When cosmic rays experience collisions with atoms of the upper atmosphere (about 10 km above the ground), they create extensive air showers (EAS), a cascade of "secondary" particles that propagate through the atmosphere towards the earth's surface. EAS resulting from cosmic rays produce ionization columns which are detected by such conventional observatories as ground surface-detector arrays and fluorescence detectors. Currently, the Telescope Array (TA) detector, which has been operating in Utah since 2007, employs two detection mechanisms: three fluorescence detectors (FDs) that record the ultraviolet light (UV) emitted from EAS, and a grid of scintillation detectors (SDs) that measures the flux of secondary charged particles arriving at the surface [2]. Fluorescence detection is costly and has a low duty cycle (about 10%), since the observations can only be made on clear moonless nights. Scintillation detectors operate with 100% duty cycle, but must cover hundreds or thousands of square kilometers in order to obtain reasonable detection rates. For example, the world's two largest detectors now in operation, the Telescope Array (Utah) [3] and the Auger Observatory (Argentina) [4], utilize ground arrays covering 800 km^2 and 3,000 km^2, respectively. Therefore, a clear motivation exists for moving towards a simpler and more efficient technique such as radar.

Our research group, the Telescope Array RAdar (TARA) project, is working on a novel approach based on bistatic radar technology [5]. This technique is promising and if successful, it will allow the next generation of cosmic ray observatories to be built at a

fraction of the cost required by current technologies.

TARA is co-located with the TA detector, a conventional cosmic ray detector, which happens to be located in a low-noise environment; this way, radar echoes can coincide with real events found in reconstructed TA data. Co-location with a conventional detector allows for definitive coincidence studies to be performed. If coincidences are detected, the conventional detector's information on the air shower geometry will allow direct comparison of radar echo signals with the predictions of air shower radio frequency (RF) scattering models.

Fig. 1.1(a) includes a map illustrating the location of the radar transmitter and receiver relative to the conventional Telescope Array detector. Fig. 1.1(b) and (c) show the TARA transmitter and receiver antenna arrays, respectively, which are currently in operation. TARA transmitter operates in a vacant VHF band and consists of broadband log-periodic antennas, designed to zoom the transmit beam on the part of the sky that is more likely to give a strong reflection from air showers. Multiple receive antennas are used to provide a space diversity gain.

1.2   The Research Problem

The motivation beyond radar detection of cosmic ray air showers lies in the large ionization densities, at the core of the air shower, which can reflect radio frequencies that lie in the low VHF band. Research studies have shown that the radar cross section is greatest in the forward scattering direction [6]. Thus, bistatic radar is advantageous in detecting weak returning echoes, in comparison with monostatic or ranging radar. Based on the physical features of our radar target, returning echoes are excepted to be characterized by a rapid phase modulation-induced frequency shift, covering several tens of MHz in a period of 10 to 15 μsec. These signals sweep linearly from a high to low frequency, this can be modeled as a linear-downward chirp. Also, the related parameters of the received echoes are nondeterministic, since they are tied to the physical parameters of the air showers which are affected by the energy of the underlying particle and its angle of arrival as it reaches the earth's atmosphere. Thus, unlike most of the existing chirp applications, we are interested in the detection of chirp echoes of variable parameters, center frequencies and frequency rates, within a relatively wide band. In addition, our detection threshold is required to be set as low as possible in order to enhance the ability of detecting signals of signal-to-noise ratio (SNR) in the negative dB range.

Besides the above mentioned challenges, our problem is characterized by the rarity of the expected chirp-echoes to be received, few events per week, and thus, background noise
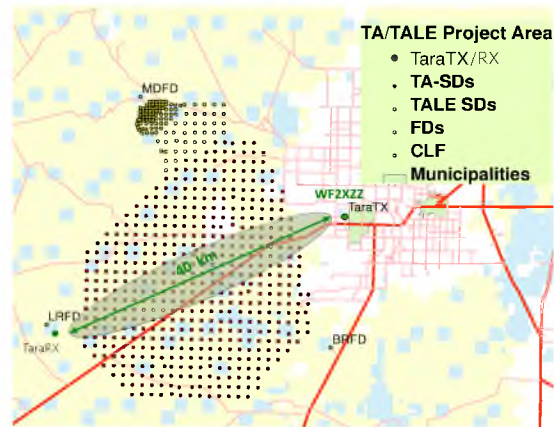
Figure 1.1: Illustrative diagram for the TARA observatory. (a) Map of TARA observatory sites (transmitter and receiver) along with the Telescope Array (TA) detector facilities. The transmitter broadcasts as station WF2XZZ near Hinckley, Utah, towards a receiver site located at the TA Long Ridge Fluorescence Detector. The sounding radiation illuminates the air over the central portion of the TA Surface Detector array. (b) Transmitter antenna array. (c) Receiver antenna array.

reception is the case most of the time. Based on our radar environment, background noise is punctuated with persistent single-frequency tones that might originate from different sources around the receiver unit including the radar carrier signal (54.1MHz). These deceptive tones are powerful, which, may accordingly, lead to positive false-alarms. The other major source of false-alarm is the sudden noise spikes that cover wide frequency bands. These spurious signals cause an erroneous radar detection decision by exceeding the detection threshold.

All these challenges that confront our radar system make the problem of interest unique and give rise to the need for robust signal processing technique as well as a detailed analysis that this research strives for.

1.3   Research Contributions

Research contributions of this dissertation can be summarized as follows:

1. A strategy is proposed for the detection of chirp signals with nondeterministic chirp rates based on the method of matched filtering. We propose a rake-like receiver that consists of a bank of filters matched to a number of quantized chirp rates. Through analytical results, we show that distributing the matched filters logarithmically within the chirp-rate interval of interest is a near optimal selection. We examine the detection capability of the proposed structure through extensive theoretical and numerical analysis. Theoretical analysis and simulation results prove that the proposed detector has high detection capability for a range of chirp slopes under low SNR environment. This work in presented in [7].

2. One major source of false-alarm in our application is the sudden noise spikes that cover wide frequency bands. We propose adding an amplitude limiter prior to the bank of filters to alleviate the effect of the high amplitude spikes. This enables us to bring down the detection threshold and thus obtain better detection performance. This work is presented in [8].

3. Proposed receiver is implemented over a Virtex-5 FPGA. National Instruments modules are used as a high-performance custom hardware. Due to the rarity of received echoes, we emulate the expected radar echoes to evaluate the system performance. The detection performance of the emulated echoes is examined using the implemented receiver at the field. This work is presented in [9] and [10].

4. Linear chirp signals have a unique signature in time-frequency domain. This property motivated us to study the detection of linear chirps using this interesting domain. We propose a detection algorithm based on Hough transform for detecting our radar received echoes that can deal with the existing receiver environment. The detection capability of the proposed structure is examined through theoretical and numerical analysis. Proposed receiver is implemented using system-on-chip design in a similar way to the first method. This work is presented in [11].

5. As a member of TARA collaboration, I participated in constructing the world's first bistatic radar observatory for Ultra-High Energy Cosmic Rays (UHECR). Construction was completed during summer 2013. TARA is co-located with the Telescope Array, the largest conventional cosmic ray detector in the Northern Hemisphere, in radio-quiet

Western Utah. TARA employs an 8MW Effective Radiated Power (ERP) VHF transmitter and smart receiver system in an effort to detect the scatter of sounding radiation by UHECR-induced atmospheric ionization. TARA seeks to demonstrate bistatic radar as a useful new remote sensing technique for UHECRs.

I was lead coordinator and responsible for the construction, design, implementation, and testing of the receiver side in the project. This work is presented in [5], [10], [12], [13], and [14].

1.4 Dissertation Outline

This dissertation is divided into seven chapters. Chapter 1, this chapter, describes the motivation behind this dissertation, characterizes the research, and summarizes our research contributions. In Chapter 2, we present a review of relevant literature. Chapter 3 illustrates our first method, the rake-like receiver. A thorough analysis of the proposed method under a white-Gaussian noise background is also presented. In Chapter 4, we introduce our bistatic radar experiment and the experimental results. In Chapter 5, we present the proposed amplitude limiter and discuss the corresponding radar system performance. In Chapter 6, we introduce the Hough transform based detector. Finally, conclusions and future directions are given in Chapter 7.

CHAPTER 2

REVIEW OF LITERATURE

Linear chirp signals are ubiquitous in nature. They can be observed in many areas, such as echolocation (bats) [15], geophysics [16], underwater explorations [17], and gravitational waves in astrophysics [18]. Also, they are frequently encountered in various areas of signal processing, such as sonar [19], radar [20], and spread spectrum communications [21, 22]. Some of these applications rely on chirp signal transmission as in the case of sonar [19], while others model the received signal after doppler spread as chirp signals, e.g., in synthetic aperture radars (SARs) [23], and heart sound signals [24].

In a radar problem, the transmitted signal will be subject to a phase shift induced by the distance and relative motion between the target and the receiver. Thus, a chirp signal can be observed. The phase angle of the chirp reflects the related parameters of the radar target including the speed and range. In the literature, various techniques have been developed for the estimation of chirp parameters, including the doppler frequency shift [25] and the doppler frequency rate [26]. In the current phase of our radar application, our main interest lies in the detection of the received chirp echoes produced by cosmic ray induced air showers. Our main goal is simply to find an approach that counteracts the challenges and provides a reasonably high performance under the existing challenges and our hardware limitation.

Different techniques have been developed for the detection of linear chirp signals. The developed methods may target the detection problem in different domains: time-domain or frequency domain or joint time-frequency domain.

The time-domain methods include several adaptive algorithms that approach the detection problem as a recursive least squares (RLS) algorithm [27], or a least mean square (LMS) algorithm [28], and a multiple frequency tracker [29]. However, these adaptive techniques suffer performance degradation under low-SNR conditions [30].

Matched filters are one of the most commonly used time-domain methods in radar systems. Basically, a matched filter correlates a known *deterministic* signal with the received signal in order to maximize the peak output SNR when a noisy radar echo is passed through

it. In other radar applications, matched filters are used as pulse compression filters [31]. If the parameters of the radar chirp echoes are known, the optimal detector in stationary white-Gaussian noise is proven to be a matched filter followed by a threshold comparison [32]. Passing the chirp echo through its corresponding matched filter should result in a high peak at the output of the filter. This output is known as the chirp autocorrelation function which is well studied in many contexts, e.g., [32]. Neyman-Pearson criterion, or likelihood ratio test, is commonly used in evaluating the detection performance of the matched filter for the case of deterministic chirp signal [33]. In the case of multiple deterministic chirp signals, generalized likelihood ratio test (GLRT) detector is considered where a bank of matched filters are used, [33]. A mismatch of chirp rates between the received signal and the matched filter will result in phase error and thus, a loss in the output peak value.

In our application, as mentioned before, we lack the knowledge of received signal parameters and thus, mismatch of the chirp rate between the received chirp signal and the matched filter(s) at the receiver is unavoidable.

The assumption of white-Gaussian noise is frequently used in the study of radar and communication systems to greatly simplify their analysis. For various applications, the Gaussian noise assumption is justified, such as microwave terrestrial or satellite links; however, in other cases, including ours, background noise turns out to be impulsive and thus of a non-Gaussian nature. The main reason for this is that signal background may get disturbed by external interference sources with an impulsive nature that is well above the background level. These sources could be either natural, such as lightening strikes, or man-made, like power-line communications or electric motors. In radar applications, the detection threshold may be raised in order to avoid excessive false-alarms which deteriorate the detection performance of the radar receiver. In radar literature, there are various methods that tackled this problem through using band-pass limiters [34, 35] or nonlinear functions [36, 37]. However, to our knowledge, none of these methods consider the detection problem of nondeterministic chirp signals after mitigating the effect of impulsive noise.

In this dissertation, we work out two different solutions for this problem. First, we introduce an amplitude limiter that alleviates the effect of transient background. Second, we introduce a smart time-frequency domain method that can efficiently filter the existing noGaussian components to a great extent.

Discrete Fourier transform (DFT) is considered as a standard and useful tool for spectrum analysis in the area of digital signal processing that is typically implemented in an efficient way using fast Fourier transform (FFT). Fourier transform provides the corresponding

magnitude and phase of the signal spectral content. However, it does not provide a time distribution of the spectral components which we would need for linear chirp signals to look at the change of frequency versus time. In the past, more advanced techniques have also been developed to overcome the limitations of matched filters. These methods approach the detection problem in the time-frequency plane. They exploit the hidden features of the chirp signals in the time-frequency plane by applying a transformation such as the short-time Fourier transform (STFT) or the Wigner distribution (WD) to obtain the time-frequency information. Among them, Page's test [38], the expectation-maximization (EM) algorithm [39], and Hough transform (HT) [40] are more broadly used. Other two-dimensional techniques include Radon transform [41] and Radon-Fourier transform [42]. These methods are suitable for detecting chirp signals in nonstationary noise backgrounds where false-alarms can be significantly reduced. While these approaches are more robust than the method of matched filters, a major drawback is the direct relation between computational complexity and chirp signal bandwidth.

In this dissertation, we consider Hough transform as a basis for the detection of chirp signals with nondeterministic parameters (center-frequencies and chirp-rates). We introduce additions to the proposed detector that optimize the detection performance and greatly reduce the computational complexity to become feasibly implemented.

CHAPTER 3

RAKE-LIKE RECEIVER FOR CHIRP DETECTION

3.1 Problem Statement

In our radar problem, we are interested in detecting the presence or absence of a chirp signal in a white-Gaussian noise background. The chirp signal of interest is a linear down-chirp with *known* start (high) frequency f_H Hz, *known* end (low) frequency f_L Hz, and *unknown* chirp rate of κ Hz/sec. An example of the signal of interest is shown in Fig. 3.1. Assuming that it is centered around time $t = 0$, such a chirp signal is mathematically written as

$$c_\kappa(t) = \text{rect}\left(\frac{t}{T_\kappa}\right)\cos(2\pi f_C t - \pi\kappa t^2) \tag{3.1}$$

where $T_\kappa = (f_H - f_L)/\kappa$ is the chirp duration in seconds, $f_C = (f_H + f_L)/2$, and $\text{rect}(\cdot)$ denotes the rectangular function.

For the purpose of our study in this dissertation, we consider a signal

$$x(t) = c_\kappa(t) + \nu(t) \tag{3.2}$$

where $\nu(t)$ is an additive white-Gaussian noise with variance σ_ν^2, and the time variable t ranges from $-\infty$ to $+\infty$. We also assume that $x(t)$ is passed through a filter with the impulse response $c_{\kappa_0}(-t)$, i.e., a filter that is matched to a chirp signal with the parameters f_H, f_L, and κ_0. When the magnitude of the matched filter output passes a set threshold, it is declared that a chirp has been detected. There are two possibilities: First, the case when the detection has originated from the chirp signal $c_\kappa(t)$. Second, the case when the detection has originated from the background noise $\nu(t)$. In the first case, we say correct detection has occurred, and in the second case, we say a false detection has occurred. A third case that will be also studied in this chapter is when the presence of noise misleads the detector so that the presence of chirp is not detected. We refer to this as missed-detection. In the rest of this chapter, we develop mathematical formulations that lead to expressions
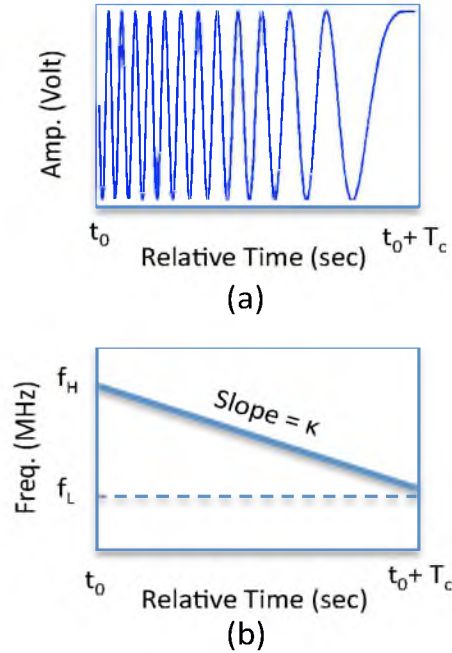
Figure 3.1: Linear down-chirp signal. (a) Signal in time-domain. (b) Signal in time-frequency domain.

for the probabilities of *correct detection*, *false detection*, and *missed-detection*. Development of these results requires mathematical tools that are developed next.

3.2 Characterizing the Filtered Components

The goal in this section is to characterize the filtered signal

$$y(t) = x(t) \star h(t) \tag{3.3}$$

where $\star$ denotes linear convolution, and $h(t) = c_{\kappa_0}(-t)$. More specifically, we are interested in the filtered chirp component

$$y_c(t) = \int_{-\infty}^{\infty} c_\kappa(\tau) h(t-\tau) d\tau, \tag{3.4}$$

and the filtered noise component

$$y_\nu(t) = \int_{-\infty}^{\infty} \nu(t) h(t-\tau) d\tau, \tag{3.5}$$

of $y(t) = y_c(t) + y_\nu(t)$.

3.2.1 Filtered Chirp Component

Considering the general case, where $\kappa \neq \kappa_0$, one finds

$$y_c(t) = \int_{-\infty}^{\infty} \text{rect}(\frac{\tau}{T_\kappa}) \, \text{rect}(\frac{t-\tau}{T_{\kappa_0}}) \cos(2\pi f_C \tau - \pi\kappa\tau^2) \cos(2\pi f_C(t-\tau) - \pi\kappa_0(t-\tau)^2) d\tau. \quad (3.6)$$

This may be rearranged as

$$\begin{aligned} y_c(t) &= \frac{1}{4} \int_{-\infty}^{\infty} \text{rect}(\frac{\tau}{T_\kappa}) \, \text{rect}(\frac{t-\tau}{T_{\kappa_0}}) \left(e^{j(2\pi f_C \tau - \pi\kappa\tau^2)} + e^{-j(2\pi f_C \tau - \pi\kappa\tau^2)} \right) \\ &\qquad \times \left(e^{j(2\pi f_C(t-\tau)+\pi\kappa_0(t-\tau)^2)} + e^{-j(2\pi f_C(t-\tau)+\pi\kappa_0(t-\tau)^2)} \right) d\tau \\ &= \frac{1}{2} \int_{-\infty}^{\infty} \text{rect}(\frac{\tau}{T_\kappa}) \, \text{rect}(\frac{t-\tau}{T_{\kappa_0}}) \Big(\cos\left(2\pi f_C t - \pi\kappa\tau^2 + \pi\kappa_0(t-\tau)^2\right) \\ &\qquad + \cos\left(2\pi f_C t - 4\pi f_C \tau + \pi\kappa\tau^2 + \pi\kappa_0(t-\tau)^2\right) \Big) d\tau. \quad (3.7) \end{aligned}$$

For typical values of κ and κ_0, the output signal component is dominated by the first term and the effect of the second term is negligible. Accordingly, $y_c(t)$ can be approximated as

$$y_c(t) \approx \frac{1}{2} \int_{-\infty}^{\infty} \text{rect}(\frac{\tau}{T_\kappa}) \, \text{rect}(\frac{t-\tau}{T_{\kappa_0}}) \cos\left(2\pi f_C t - \pi\kappa\tau^2 + \pi\kappa_0(t-\tau)^2\right) d\tau. \quad (3.8)$$

Assuming κ is greater than κ_0, and letting $\delta\kappa = \kappa - \kappa_0$, after some algebraic manipulations, we obtain

$$y_c(t) = \frac{1}{2} \int_{-\infty}^{\infty} \text{rect}(\frac{\tau}{T_\kappa}) \, \text{rect}(\frac{t-\tau}{T_{\kappa_0}}) \cos\left(\pi\delta\kappa \left(\tau + \frac{\kappa_0 t}{\delta\kappa}\right)^2 - \phi(t)\right) d\tau \quad (3.9)$$

where $\phi(t) = \pi t \left(2f_C + \kappa_0 t + \frac{\kappa_0^2 t}{\delta\kappa}\right)$. Furthermore, noting that the duration of $h(t)$ is longer than that of $c_\kappa(t)$, (3.9) can be written as

$$y_c(t) = \frac{1}{2} \int_{-\frac{T_\kappa}{2}}^{\frac{T_\kappa}{2}} \cos\left(\pi\delta\kappa \left(\tau + \frac{\kappa_0 t}{\delta\kappa}\right)^2 - \phi(t)\right) d\tau \, . \quad (3.10)$$

This result can be simplified as

$$y_c(t) = \frac{1}{\sqrt{4\pi\delta\kappa}} \left\{ \cos(\phi(t)) \int_{\theta_1(t)}^{\theta_2(t)} \cos(u^2) du - \sin(\phi(t)) \int_{\theta_1(t)}^{\theta_2(t)} \sin(u^2) du \right\} \quad (3.11)$$

where

$$\theta_1(t) = \sqrt{\pi\delta\kappa} \left(\frac{\kappa_0 t}{\delta\kappa} - \frac{T_\kappa}{2}\right) \quad (3.12)$$

and

$$\theta_2(t) = \sqrt{\pi\delta\kappa} \left(\frac{\kappa_0 t}{\delta\kappa} + \frac{T_\kappa}{2}\right). \quad (3.13)$$

Also,

$$\int_{\theta_1(t)}^{\theta_2(t)} \cos(u^2) du = \sqrt{\frac{\pi}{2}} \left(C\left(\sqrt{\frac{2}{\pi}} \theta_2(t)\right) - C\left(\sqrt{\frac{2}{\pi}} \theta_1(t)\right) \right) \quad (3.14)$$

and

$$\int_{\theta_1(t)}^{\theta_2(t)} \sin(u^2)du = \sqrt{\frac{\pi}{2}} \left(S\left(\sqrt{\frac{2}{\pi}}\theta_2(t)\right) - S\left(\sqrt{\frac{2}{\pi}}\theta_1(t)\right) \right) \tag{3.15}$$

where $C(x)$ and $S(x)$ are Fresnel cosine and sine integrals [[43], pp.887, Eq. (8.250)], respectively. Substituting (3.14) and (3.15) in (3.11), we get

$$\begin{aligned} y_c(t) &= \frac{1}{\sqrt{8\delta\kappa}} \Bigg\{ \cos(\phi(t)) \left[C\left(\sqrt{\frac{2}{\pi}}\theta_2(t)\right) - C\left(\sqrt{\frac{2}{\pi}}\theta_1(t)\right) \right] \\ &\quad - \sin(\phi(t)) \left[S\left(\sqrt{\frac{2}{\pi}}\theta_2(t)\right) - S\left(\sqrt{\frac{2}{\pi}}\theta_1(t)\right) \right] \Bigg\} . \end{aligned} \tag{3.16}$$

3.2.2 Filtered Gaussian Noise

The output noise component $y_\nu(t)$ is defined as

$$y_\nu(t) = \int_{-\infty}^{\infty} \nu(\tau)h(t-\tau)d\tau . \tag{3.17}$$

Filtered noise is a Gaussian process with zero-mean and covariance function $r(t)$ which is defined as

$$r(t) = \int_{-\infty}^{\infty} y_\nu(\tau)y_\nu(\tau-t)d\tau . \tag{3.18}$$

Assuming unit noise variance, i.e., $\sigma_\nu^2 = 1$, $r(t)$ is simplified to the autocorrelation function of the chirp signal $c_\kappa(t)$. This can be easily deduced from (3.16) by setting $\kappa = \kappa_0$. The result simplifies to

$$r(t) = \frac{(T_\kappa - |t|)}{2} \cos\left(2\pi f_{\rm C}t\right) \operatorname{sinc}\left(\kappa t\left(T_\kappa - |t|\right)\right) . \tag{3.19}$$

3.3 Detection Analysis

For the radar setup introduced in Section 3.1, there are two signal conditions - either noise only or signal-plus-noise and two possible outcomes from the threshold comparison - either filtered output exceeds a threshold or it does not. Ideally, we wish to correctly detect a chirp, when it exists. For the signal model (3.2), this is the case, when t is around zero. Also, we wish not to detect anything when the chirp is absent. We term the probability of signal-plus-noise exceeding threshold as probability of correct detection (PCD). The complement of PCD is termed as probability of missed-detection (PMD). Also, we term the average rate of erroneous detection decisions caused by filtered noise as *false-alarm rate* (FAR).

Our strategy is to choose the threshold (γ) that, for a given signal-to-noise ratio, leads to a PCD close to one, while keeping a reasonable (small) value of FAR. The threshold

selection is subject to compromise between aiming at high detection efficiency to avoid missing real radar events and maintaing a low level of false-alarms to keep less storage (low system cost) and accelerating the offline processing of the stored data. We start our analysis by investigating the relation between (γ, FAR) and then (γ, PCD).

3.3.1 False-Alarm Rate

When the chirp is absent, the detection problem is reduced to noise reception and $y(t)$ reduces to $y_\nu(t)$. In our triggered data acquisition system, $|y_\nu(t)|$ is compared to a threshold level γ. When $|y_\nu(t)|$ exceeds γ, a positive false-alarm is generated. In order to mitigate false-alarms, the detection threshold γ should be set high which comes at the expense of missing the detection of a low-level chirp, if present. Thus, it is desirable to have a detection threshold that minimizes PMD while keeping FAR below a certain level.

The problem of FAR is that of determining the level-crossing rate (LCR) of $y_\nu(t)$. According to a theorem from Rice, [44], the average number of up-crossings of the filtered Gaussian signal $y_\nu(t)$ through a threshold level γ per second is given by

$$N_\eta = \frac{1}{2\pi} \lambda^{1/2} e^{-\frac{\eta^2}{2}} \; , \tag{3.20}$$

where $\lambda = -r''(0)/r(0)$ and $r''(0)$ is the second derivative of the covariance function $r(t)$ at $t = 0$. η is the normalized threshold level, i.e., $\eta = \gamma/\sigma_{y_\nu}$, where $\sigma_{y_\nu}^2$ is the variance of the output noise component $y_\nu(t)$.

Using the evaluated autocorrelation formula (3.19), λ can be evaluated as shown in Appendix A. This leads to

$$\lambda = \left((2\pi f_C)^2 + \frac{(\pi B)^2}{3} \right), \tag{3.21}$$

where $B = f_H - f_L$.

Noting that a false-alarm occurs every time $y_\nu(t)$ exceeds γ or drops below $-\gamma$, one finds that

$$
\begin{aligned}
\text{FAR} &= 2N_\eta \\
&= \frac{1}{\pi} \sqrt{\left((2\pi f_C)^2 + \frac{(\pi B)^2}{3} \right)} \; e^{-\frac{\eta^2}{2}} \; .
\end{aligned}
\tag{3.22}
$$

It is interesting to note that FAR is a function of center frequency and bandwidth of the chirp. Also, FAR is independent of the noise variance σ_ν^2. It is a function of the normalized threshold level η. This means that our detector follows the constant false-alarm rate (CFAR) criterion by using an adaptive threshold (γ) that tracks noise variations.

3.3.2 Probability of Correct Detection

Analysis of PCD based on continuous time signals turns out to be a difficult task. Thus, here, we resort to an analysis of PCD in discrete time. Assuming that a sufficiently high sampling rate is selected, the result will be very close to those of continuous time.

Assuming a sampling interval T_s, the equivalent discrete time of the chirp signal $c_\kappa(t)$ is obtained as

$$c_{\kappa,n} = \cos\left(2\pi f_C n T_s - \pi\kappa(nT_s)^2\right), \quad n = -N/2, \ldots, 0, \cdots, N/2 - 1, \tag{3.23}$$

where $N = 2\lfloor (T_\kappa/2)/T_s \rfloor$. A similar results is applicable for $c_{\kappa_0,n}$, where κ is replaced by κ_0 and N by N_0. Let $\mathbf{y}$ denote the $2N_0 + 1$ vector of samples of $y(t)$ over the interval[1] $(-T_{\kappa_0}, T_{\kappa_0})$. Similarly, the corresponding vectors of samples of $y_c(t)$ and $y_\nu(t)$ are denoted as $\mathbf{y}_c$ and $\mathbf{y}_\nu$, respectively. In case the chirp signal is present, $\mathbf{y} = \mathbf{y}_c + \mathbf{y}_\nu$ is a Gaussian vector with mean of $\mathbf{y}_c$ and an autocorrelation matrix $\mathbf{R}$ whose elements are samples of the autocorrelation function $r(t)$ of (3.19). On the other hand, when the chirp signal is absent, $\mathbf{y} = \mathbf{y}_\nu$ is a Gaussian vector with zero mean and autocorrelation matrix $\mathbf{R}$.

To derive an equation for PCD, we note that

$$\text{PCD} = 1 - \text{PMD} \tag{3.24}$$

and

$$\text{PMD} = p_Y\left(\forall n : |y_n| \leq \gamma\right) \tag{3.25}$$

where $\forall$ denotes 'for all'. Accordingly, PMD is calculated as

$$\text{PMD} = \frac{1}{\sqrt{\det\{2\pi\mathbf{R}\}}} \int_{-\gamma}^{\gamma} \cdots \int_{-\gamma}^{\gamma} e^{-\frac{1}{2}(\mathbf{y}-\mathbf{y}_c)^T \mathbf{R}^{-1}(\mathbf{y}-\mathbf{y}_c)} d\mathbf{y} \tag{3.26}$$

where $d\mathbf{y}$ is the shorthand notation for $dy_{N_0} \cdots dy_0 \cdots dy_{-N_0}$. Changing integration variable $\mathbf{y}$ to $\mathbf{z} = \mathbf{y} - \mathbf{y}_c$, we obtain

$$\text{PMD} = \frac{1}{\sqrt{\det\{2\pi\mathbf{R}\}}} \int_{-\gamma-y_{c,-N_0}}^{\gamma-y_{c,-N_0}} \cdots \int_{-\gamma-y_{c,N_0}}^{\gamma-y_{c,N_0}} e^{-\frac{1}{2}\mathbf{z}^T \mathbf{R}^{-1}\mathbf{z}} d\mathbf{z}. \tag{3.27}$$

This is a standard integral and various numerical methods for its evaluation are available in the literature. Here, we follow the method described by Genz in [45]. To keep this

---

[1]One may note the deterministic part of $y(t)$ (assuming that κ and κ_0 are known) stretches over the interval $\left(-\frac{T_\kappa + T_{\kappa_0}}{2}, \frac{T_\kappa + T_{\kappa_0}}{2}\right)$. Here, since we assume κ_0 is a known parameter, but κ is a random variable (but, usually close to κ_0), for the simplicity of the derivations, but without any significant loss in the accuracy of the results, we consider a length $2T_{\kappa_0}$ of $y(t)$, centered around $t = 0$.

chapter self-contained, a summary of the relevant derivations of Genz's method is presented in Appendix B. This leads to the following simplified expression for PMD.

$$\text{PMD} = (b_{-N_0} - a_{-N_0}) \int_0^1 (b_{-N_0+1} - a_{-N_0+1}) \int_0^1 (b_{-N_0+2} - a_{-N_0+2}) \cdots (b_{N_0} - a_{N_0}) \int_0^1 d\mathbf{c}$$

(3.28)

where $d\mathbf{c}$ is the shorthand notation for $dc_{N_0} \cdots dc_0 \cdots dc_{-N_0}$. In addition,

$$a_i = \Phi \left(\left[-\gamma - y_{c,i} - \sum_{j=-N_0}^{i-1} l_{i,j} \Phi^{-1}(b_j + (b_j - a_j)c_j) \right] / l_{i,i} \right), \quad i = -N_0 + 1, \ldots, 0, \cdots, N_0$$

(3.29)

and

$$b_i = \Phi \left(\left[\gamma - y_{c,i} - \sum_{j=-N_0}^{i-1} l_{i,j} \Phi^{-1}(b_j + (b_j - a_j)c_j) \right] / l_{i,i} \right), \quad i = -N_0 + 1, \ldots, 0, \cdots, N_0$$

(3.30)

where

$$a_{-N_0} = \Phi \left(\left(-\gamma - y_{c,-N_0} \right) / l_{-N_0,-N_0} \right)$$

(3.31)

and

$$b_{-N_0} = \Phi \left(\left(\gamma - y_{c,-N_0} \right) / l_{-N_0,-N_0} \right).$$

(3.32)

The function $\Phi(\cdot)$ is defined in (B.7). The innermost integral in (3.28) is equal to unity and thus, the number of integration variables is reduced from $2N_0 + 1$ to $2N_0$.

The above integral can be computed using a variety of numerical integration methods. Here, we use Monte Carlo integration method, based on uniform sampling. We follow the subregion adaptive method described in [46]. This leads to the algorithm presented in Table 3.1. We present details of the Monte Carlo integration method in Appendix C.

3.4   Chirp Detector

In this section, we develop a method of systematically choosing the parameters of a bank filters matched to a set of chirp rates in order to assure a high probability of correct detection while keeping a low level of false-alarm rate. Without loss of generality, we consider our radar application as a specific example that our design will be applied to. For the echoes being reflected from cosmic ray induced air showers, the chirp rates of interest belong to

Table 3.1: Summary of the Monte Carlo Integration Method.

Input:	$\mathbf{y}_c, \mathbf{R}$
Parameters:	Threshold: γ, Number of iterations: $N_{\max}$, Variance of the result: σ^2
Output:	PMD and PCD

1. Compute lower triangular Cholesky matrix $\mathbf{L} = [l_{i,j}] \ \forall(i,j)$, of $\mathbf{R} = \mathbf{LL}^T$.

2. Set $a_{-N_0} = \Phi\left(\left(-\gamma - y_{c,-N_0}\right)/l_{-N_0,-N_0}\right)$,
   $b_{-N_0} = \Phi\left(\left(\gamma - y_{c,-N_0}\right)/l_{-N_0,-N_0}\right)$.

3. Initialize: $n = 1, \mathrm{PMD}(1) = 0, \sigma_e^2(n) = $ a large value, $\Psi(-N_0) = (b_{-N_0} - a_{-N_0})$.

4. **while** $\{\sigma_e^2(n) > \sigma^2 \text{ AND } n < N_{max}\}$
   {

   - Generate uniformly-distributed random vector $[c_{-N_0}, \cdots, c_{N_0-1}]$ ϵ [0,1]

   - **For** $i = -N_0 + 1 : N_0$
       Set $u_{i-1} = \Phi^{-1}(b_{i-1} + (b_{i-1} - a_{i-1})c_{i-1})$
       Compute $a_i = \Phi\left(\left[-\gamma - y_{c,i} - \sum_{j=-N_0}^{i-1} l_{i,j}u_j\right]/l_{i,i}\right)$
       Compute $b_i = \Phi\left(\left[\gamma - y_{c,i} - \sum_{j=-N_0}^{i-1} l_{i,j}u_j\right]/l_{i,i}\right)$
       $\Psi(i) = (b_i - a_i)\Psi(i-1)$
     End

   - Let $\delta = \frac{1}{n}(\Psi(N_0) - \mathrm{PMD}(n))$

   - Update the integral: $\mathrm{PMD}(n+1) = \mathrm{PMD}(n) + \delta$

   - Update the variance: $\sigma_e^2(n+1) = \frac{n-1}{n}\sigma_e^2(n) + \delta^2$

   - Increment n

   }

5. $\mathrm{PCD} = 1 - \mathrm{PMD}$

the interval $\mathcal{K} = [-3, -1]$ MHz/μs. We decide on the number and locations of the matched filters in this interval and the threshold parameter γ that leads to a small probability of false-alarm; the probability of correct detection remains very close to one.

Consider a received chirp signal with an arbitrary chirp rate κ, that lies within the chirp-rate interval $\mathcal{K}$, and a filter matched to the chirp rate κ_0. In Fig. 3.2, we graphically demonstrate the output of the matched filter. When κ equals κ_0, the output of the matched filter exhibits a sharp peak in response to the chirp waveform. When $\kappa \neq \kappa_0$, the sharp peak
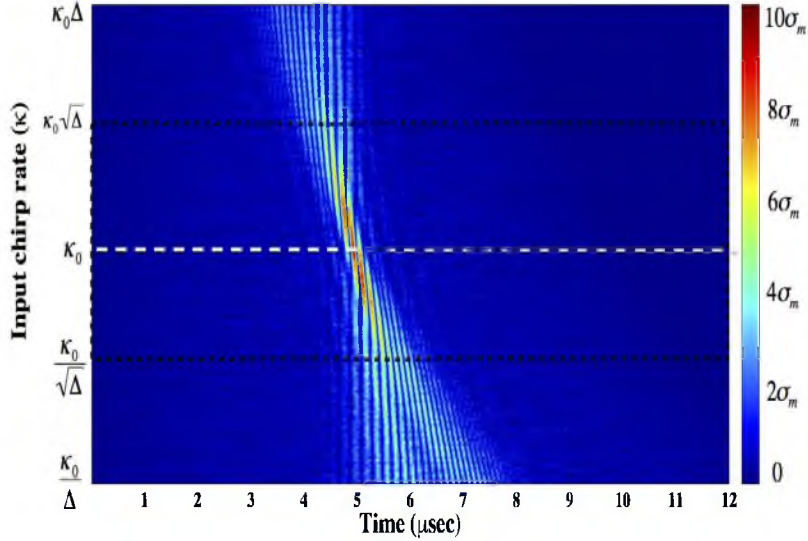
Figure 3.2: Color map indicating the detection of a range of chirp rates using a single matched filter.

in the matched filter output spreads out and disappears as the difference between κ and κ_0 increases. To quantify the peak degradation as the mismatch between κ and κ_0 increases, we graphically demonstrate the peak output of the matched filter using (3.16) for a range of κ values within an interval around κ_0. Fig. 3.3 depicts the percentage of peak degradation for a range of logarithmically distributed κ values around κ_0. This result clearly shows that the matched filter correlates well with chirp signals whose chirp-rate is within a range from κ_0. Specifically, chirp signals with $\frac{\kappa_m}{\sqrt{\Delta}} < \kappa < \kappa_m\sqrt{\Delta}$ results in a peak with an absolute value greater than 80% of the peak output, when $\kappa = \kappa_0$, where Δ denotes the logarithmic step between two chirp-rates.

Following the above observation, to ensure at least one reasonably high matched filter output, hence, to avoid a miss-detection, we consider a detector that uses a bank of M filters, matched to a number of quantized chirp rates, κ_1, κ_2, $\cdots$, κ_M, logarithmically distributed as depicted in Fig. 3.4, within the interval of interest. If we consider 80% of the peak output as still an acceptable peak, according to the result presented in Fig. 3.3, the parameter M and the equally spaced chirp rates κ_1, κ_2, $\cdots$, κ_M should be elected within the interval $\mathcal{K} = [-3, -1]$ MHz/μs, such that
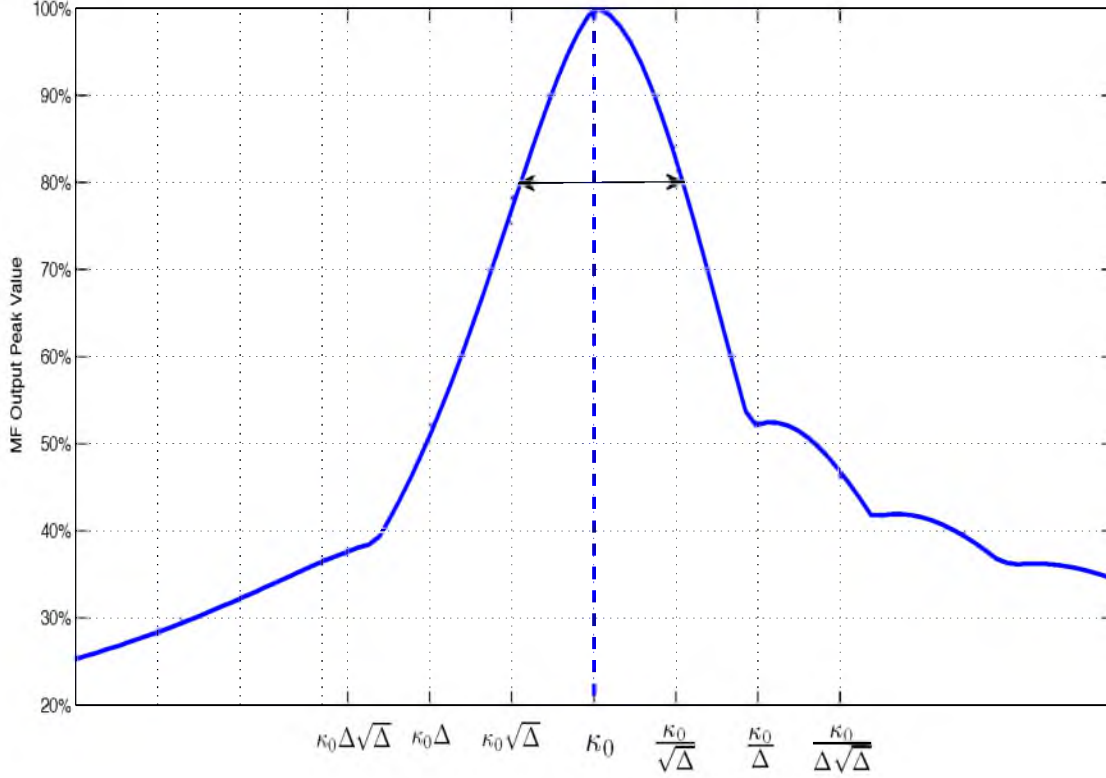
Figure 3.3: Matched filter output peak value degradation in percentage.

$$\begin{cases} \dfrac{\kappa_1}{-1} \le \sqrt{\Delta} \\[2mm] \dfrac{\kappa_{m+1}}{\kappa_m} \le \Delta, \text{ for } m = 1, 2, \cdots, M-1 \\[2mm] \dfrac{-3}{\kappa_M} \le \sqrt{\Delta}. \end{cases} \tag{3.33}$$

The solution to this problem can be easily worked out. The result is $M = 5$ and the following are chirp rates in MHz/μs

$$\kappa_1 = -1.1161, \kappa_2 = -1.3904, \kappa_3 = -1.7321, \kappa_4 = -2.1577, \kappa_5 = -2.6879$$

A functional block diagram of the detection process is illustrated in Fig. 3.5. A decision is made at the output of the matched filter-bank by comparing magnitudes of the elements of $\mathbf{y_1}, \mathbf{y_2}, \cdots, \mathbf{y_M}$, each, against the corresponding threshold levels $\gamma_1, \gamma_2, \cdots, \gamma_M$, respectively. Threshold levels are defined as n_γ units of the signal level (equivalently, noise standard deviation) at the output of each filter, denoted by σ_m for the mth matched filter. Every time a trigger condition is met, an event (the presence of chirp) is announced.

For each recorded event, we are interested in testing between two exclusive hypotheses: (i) the *null hypothesis* denoted as H_0 and (ii) the *alternative hypothesis* denoted as H_1. H_0

-3 MHz/μs

κ_M

κ_{M-1}

$\updownarrow \leq \sqrt{\Delta}$

$\Delta \geq \dfrac{\kappa_{m+1}}{\kappa_m}$

κ_2

κ_1

-1 MHz/μs
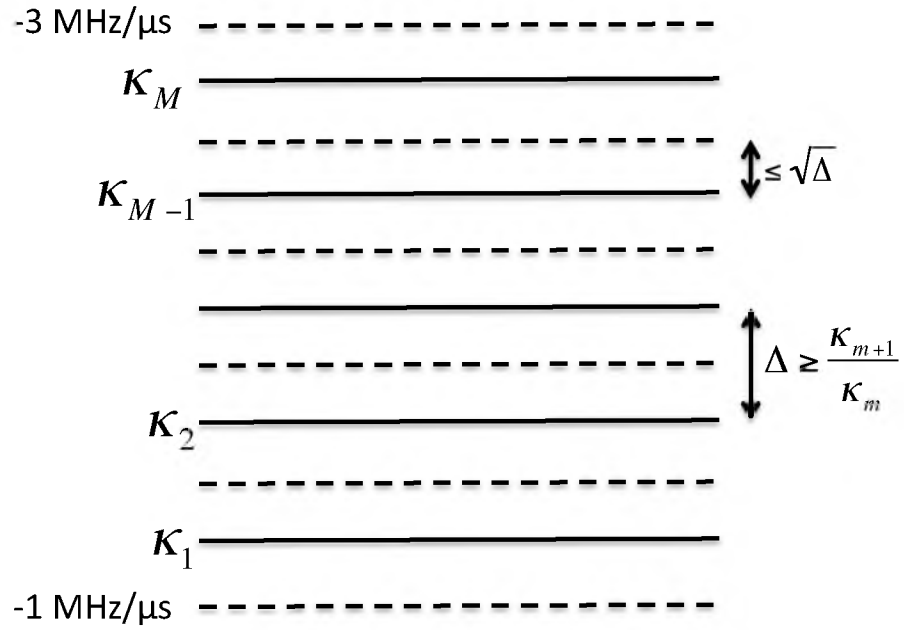
Figure 3.4: Chirp rate parameter logarithmic distribution over the set of matched filters

MF(1)
K_1 MHz/μsec y_1

MF(2)
K_2 MHz/μsec y_2

x
Input

MF(M-1)
K_{M-1} MHz/μsec y_{M-1}

MF(M)
K_M MHz/μsec y_M

Magnitude
Detection
and
Threshold
Comparison

Decision
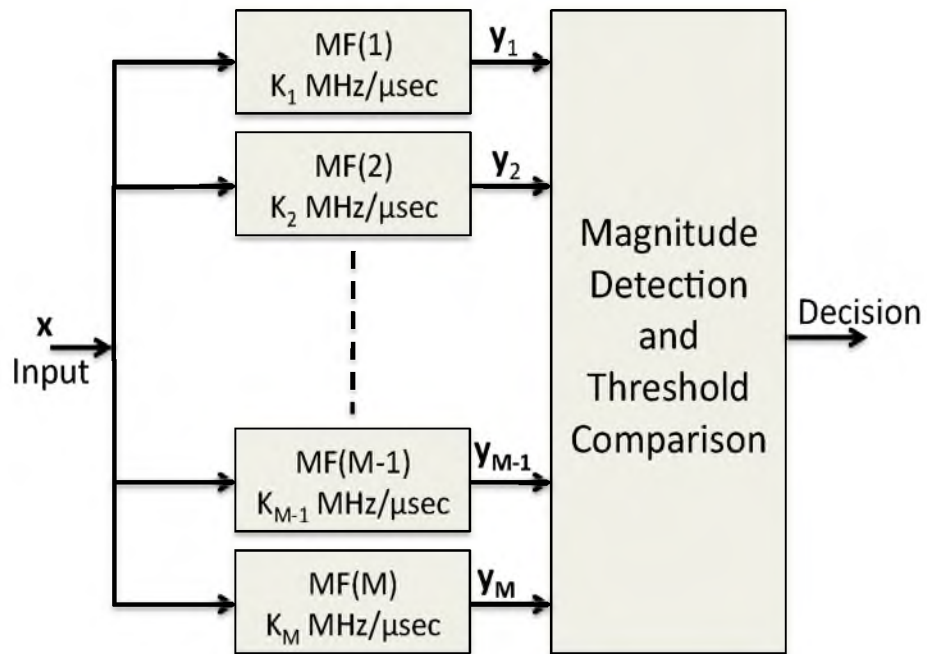
Figure 3.5: Block diagram of the chirp detector.

and H_1 correspond to the cases of chirp absence and chirp presence, respectively.

3.4.1 H_0: Chirp Signal Absence

When the chirp signal is absent, the false-alarms generated by a bank of matched filters is the sum of false-alarms generated by all the filters. These alarms would be independent, if the signals at the outputs of matched filters were a set of independent processes. In that case, for small values of FARs, one could say the total number of false-alarms is equal to the sum of false-alarms originated form each matched filter. Accordingly, one finds that

$$\text{FAR} = \sum_{m=1}^{M} \text{FAR}_m \tag{3.34}$$

where FAR_m is the false-alarm rate originated from the mth matched filter.

Clearly, the assumption that the matched filter outputs are a set of independent processes cannot be true as all filters are excited by the same input. Nevertheless, we argue that (3.34) will be approximately valid, if the Gaussian processes at the matched filters outputs (in the absence of a chirp) are approximately uncorrected. In the next section, through computer simulation tests, we find that (3.34) is quite an accurate approximation.

3.4.2 H_1: Chirp Signal Presence

Following (3.25), in presence of a bank of M matched filters, PMD is formulated as

$$\text{PMD} = p_Y(\forall n : |y_1[n]| \leq \gamma_1, \cdots, |y_M[n]| \leq \gamma_M | H_1). \tag{3.35}$$

A complete analysis of (3.35) turned out to be a difficult task. Here, to continue, we assume that the matched filters outputs are a set of independent random processes and later confirm the accuracy of this assumption through computer simulations. With this assumption, one finds that

$$\text{PMD} \quad \approx \quad \prod_{m=1}^{M} \text{PMD}_m \tag{3.36}$$

where

$$\text{PMD}_m = p_{Y_m}(\forall n : |y_m[n]| \leq \gamma_m | H_1). \tag{3.37}$$

The numerical results presented in the following section show that (3.36) is indeed an accurate approximation for the matched filter bank design that was presented above.

3.5   Numerical Analysis

In this section, we present numerical results that are obtained from the analytical formulations of the previous sections to demonstrate the detection performance of the

proposed detector. These results are also validated by comparing them with simulation results. In evaluating (3.28) using the Monte Carlo integration method, we set $N_{max} = 100$ and $\sigma^2 = 10^{-7}$.

Before we proceed with the presentation of our numerical results, we make the following observations. It is clear from (3.22) and (3.28) that the performance of the proposed detector, for each SNR value, depends on the threshold level γ. The FAR decreases as γ increases. Also, PCD increases as γ decreases. On the other hand, since the goal is to design a system with low FAR and PCD of close to one, for a given SNR, one should choose a γ that results in a compromise between a low FAR, while keeping PCD close to one. For the problem of particular interest to us, we wish to reduce FAR as much as possible while not missing any detection of air shower incidents.

We present results of FAR and PCD for different SNR values in the range of $[-25, 10]$ dB. All numerical results are based on the matched filter bank detector that was designed in the previous section.

3.5.1 False-Alarm Rate

Equation (3.22) provides an expression for the FAR at the output of a single matched filter. As seen, it is a function of the chirp center frequency and bandwidth as well as the normalized threshold level $\eta = \gamma/\sigma_\nu$. However, it is independent of the chirp rate κ. Therefore, in the bank of M matched filters that we use in our design, for a given η, FAR_m will be the same for $m = 1, 2, \cdots, M$.

Fig. 3.6 shows the simulated and analytical results of FAR for a single matched filter output as well as the collective FAR from the bank of five matched filters in our design. As predicted by (3.34), the latter is similar to the former, but shifted vertically by a factor of $M = 5$.

We see that the simulation results match the theoretical results perfectly for the single matched filter case. However, for a bank of matched filters, we notice a deviation of the simulation results from the theoretical results at lower threshold values. This can be understood as the joint probability of false-alarm between different filters is relatively high at low threshold values, which is being neglected in our theoretical framework.
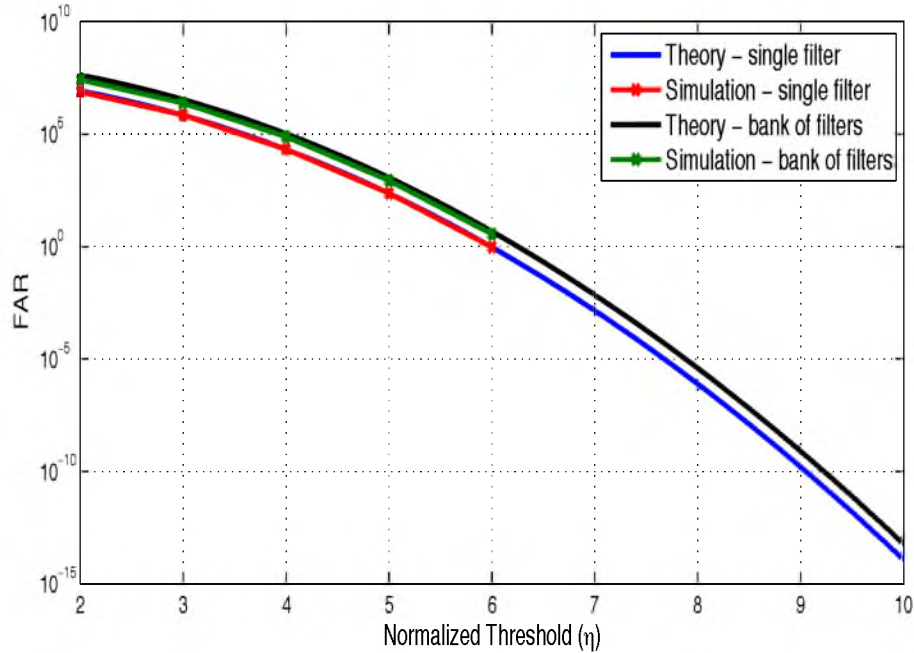
Figure 3.6: Comparison of the simulated and analytical false-alarm rate over a filtered AWGN process.

3.5.2 Probability of Detection

3.5.2.1 Detection Performance to Matched Chirps

In order to grasp a better understanding of the detection properties of the proposed detector, we start by looking at chirp signals that are perfectly matched to one of the filters in the filter bank. Fig. 3.7 presents the probability of detection under the matching case, for the five chirp slopes. The results are based on the expression given in (3.28) and simulation results. These results clearly prove the validity of our theoretical calculations. In addition, we see that PCD decreases as the chirp slope increases. This can be understood, if one notes that a larger chirp slope corresponds to a shorter chirp duration and, hence, a smaller correlation/signal peak at the filter output. This observation suggests that the chirps with smaller slopes are more likely to be seen in the proposed detectors.

3.5.2.2 Detection Performance to Mismatched Chirps

In order to appreciate the performance advantage of the proposed detector, we have to understand the limitation of the detection performance under the worst case scenario. Hence, we consider the case of receiving a linear chirp signal with a mismatched chirp slope and examine the resulting detection performance. In particular, we desire to see the effect of the maximum mismatch on the detection performance. For five matched
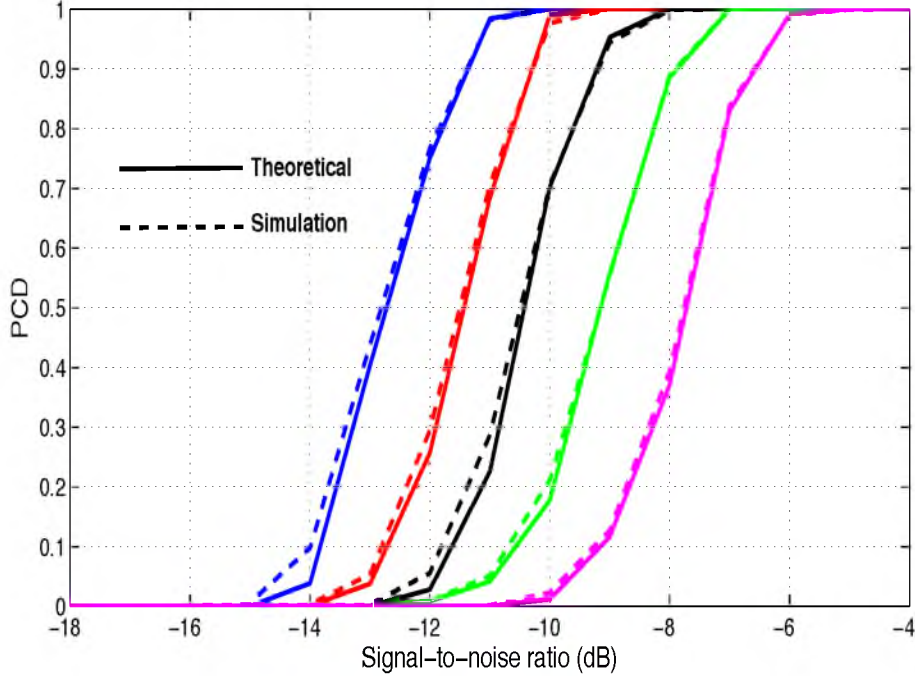
Figure 3.7: Probability of detection versus signal-to-noise ratio by the bank of filters under the matching case for threshold $12\sigma_m$.

filters, the chirp slopes with maximum mismatches within the chirp rate interval would be $\{\kappa_1/\sqrt{\Delta}, \kappa_2/\sqrt{\Delta}, \kappa_3/\sqrt{\Delta}, \kappa_4/\sqrt{\Delta}, \kappa_5/\sqrt{\Delta}, \kappa_5\sqrt{\Delta}\}$. Fig. 3.8 shows the probability of detection by the bank of filters for these chirp slopes. This figure demonstrates the expected degradation of detection performance with the increase of chirp rate. As observed, the maximum degradation observed corresponds to the chirp rate $\kappa_5\sqrt{\Delta}$. Comparing the results of Fig. 3.7 and Fig. 3.8, one finds that this degradation is about 2 dB. Clearly, this can be reduced by increasing the number of matched filters in the bank, or, to lesser extent by rearranging the positions of the five matched filters.

Next, we fix the slope of the chirp signal to be matched to the first filter ($\kappa_1 = -1.1161$ MHz/μs) and test the detection performance under different threshold levels. Fig. 3.9 presents PCD plots as a function of SNR for threshold levels ($7\sigma_1, 10\sigma_1, 13\sigma_1$). As observed, the curves shift to the right 2 to 3 dB each time the threshold is increased by $3\sigma_1$ units. It is also interesting to note that the PCD of the chirp signal with rate $\kappa_2/\sqrt{\Delta}$ is higher than that of the chirp signal with rate $\kappa_1/\sqrt{\Delta}$, although the former chirp rate is higher. This happens due to the fact that the detection of the chirp signal with the rate $\kappa_2/\sqrt{\Delta}$ is dominated by two matched filters (those with the chirp rates of κ_1 and κ_2), while the detection of the chirp signal with the rate $\kappa_1/\sqrt{\Delta}$ is dominated by only one matched
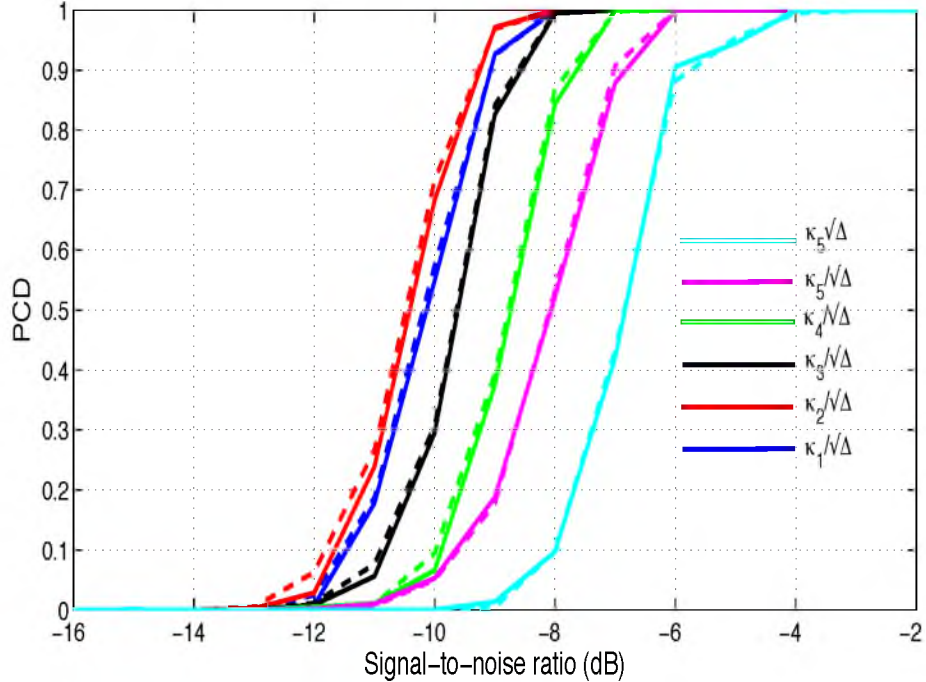
Figure 3.8: Probability of correct detection of different chirp signals versus signal-to-noise ratio by a bank of filters for threshold $12\sigma_m$.

filter (the one with the chirp rate κ_1).

3.5.3 Receiver Operating Characteristic

Fig. 3.10 shows the receiver operating characteristic (ROC) curves for the proposed detector. This set of curves show the calculated PCD of a linear chirp signal, with the rate of -1 MHz/μs, versus the FAR of the HT-based detector for a number of low received SNR values (-8 dB,-10 dB,-12 dB). Each point on each of the ROC curves corresponds to a specific threshold level. As depicted in the figure, we can find a range of threshold values $[6.5\sigma_m, 7\sigma_m]$ where FAR is in order of 10^{-2}, few events per hour, or lower and at the same time, we can get almost complete probability of detection for the transmitted chirp at SNR of -12 dB.
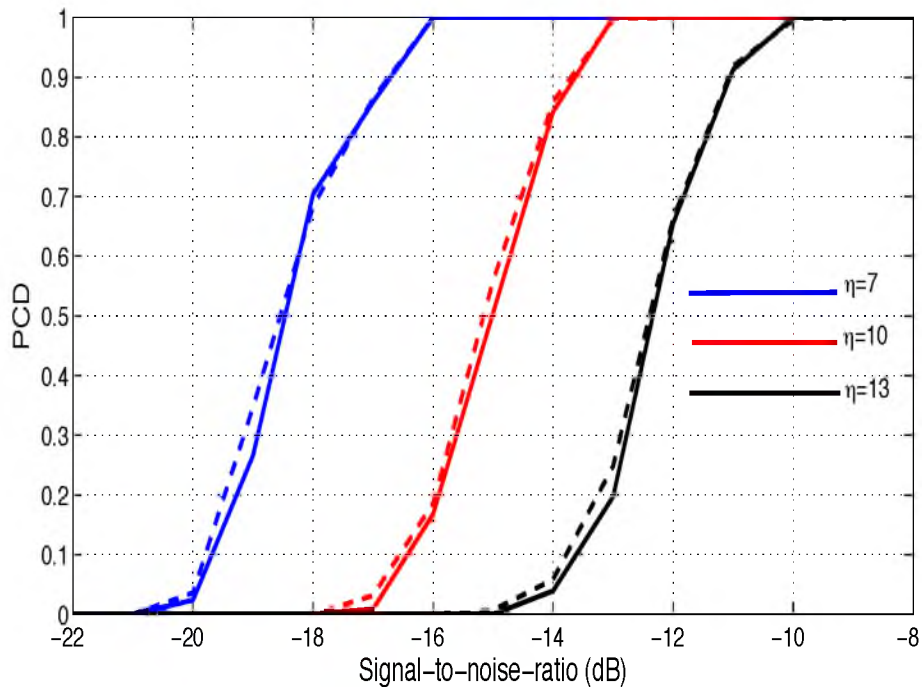
Figure 3.9: Probability of correct detection of -1.1161 MHz/μs versus signal-to-noise ratio by a matched filter under different threshold levels.
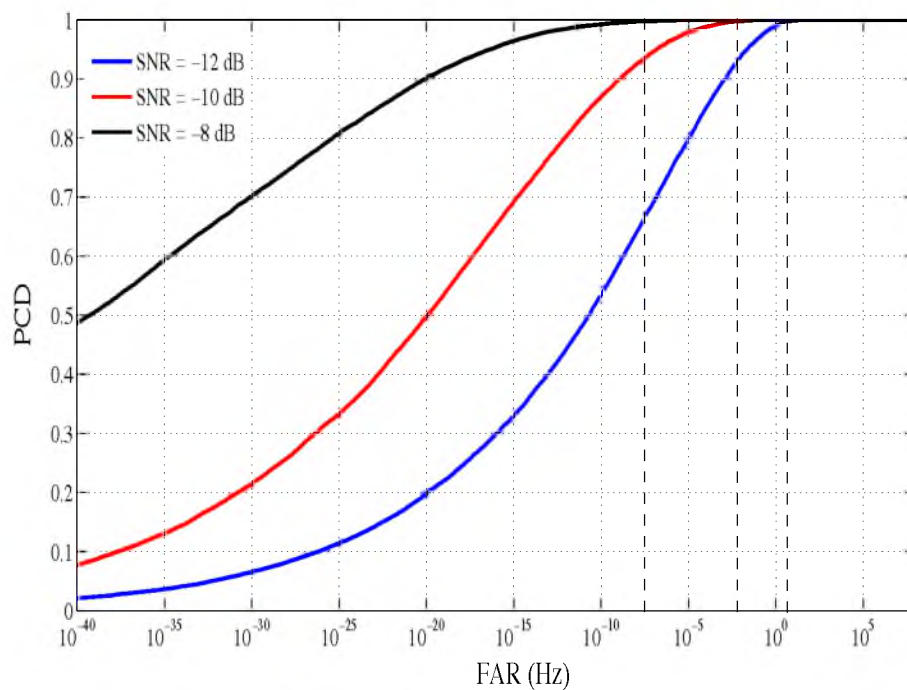
Figure 3.10: Probability of correct detection and false-alarm rate versus normalized threshold (η) under various SNR values.

CHAPTER 4

EXPERIMENTAL RESULTS

4.1 Radar Experiment Setup

The Telescope Array RAdar (TARA) project utilizes a bistatic radar technique to detect radar echoes from the ionization trails of ultra-high energy cosmic rays (UHECR) as they pass through the earth's atmosphere [10]. Fig. 4.1 shows the structural block diagram of the bistatic radar system. TARA is considered the largest and most ambitious attempt yet at detecting UHECR via their radar signature. TARA is co-located with the Telescope Array, the largest conventional cosmic ray detector in the Northern Hemisphere, in radio-quiet Western Utah.

TARA employs a very high frequency (VHF) continuous wave (CW) transmitter station at Millard county in Delta, Utah. This transmitter station, operating under FCC license, illuminates the sky with 40 kW of power above the Telescope Array surface detectors with a continuous 54.1 MHz carrier signal. We make use of analog television transmitters donated to the University of Utah by Salt Lake City's KUTV Channel 2 and ABC4 [5].

The TARA receiver antenna site is located at the Telescope Array Long Ridge Fluorescence Detector site, 40 km distant from the transmitter site. Receiver antennas are dual-polarized log periodic dipole antennas (LPDA) designed to match the expected radar echoes frequency characteristics. Due to noise below 30 MHz and the FM band above 88 MHz, the effective band is reduced to 40 to 80 MHz. There are three dual-polarization antennas at the receiver site, two of which are currently connected to the data acquisition system (see Appendix D). As depicted in Fig. 4.1, the outputs of the receiving antennas pass through the receiver RF front-end which consists of a bank of RF limiters, FM filters and amplifiers (see Appendix E). The amplified and filtered RF signals are then fed to our receiver data acquisition (DAQ) system. The DAQ is designed to detect chirp echoes and confront the problem of a variable noise environment. Appendix F gives more details about expected chirp echoes from cosmic ray air showers.
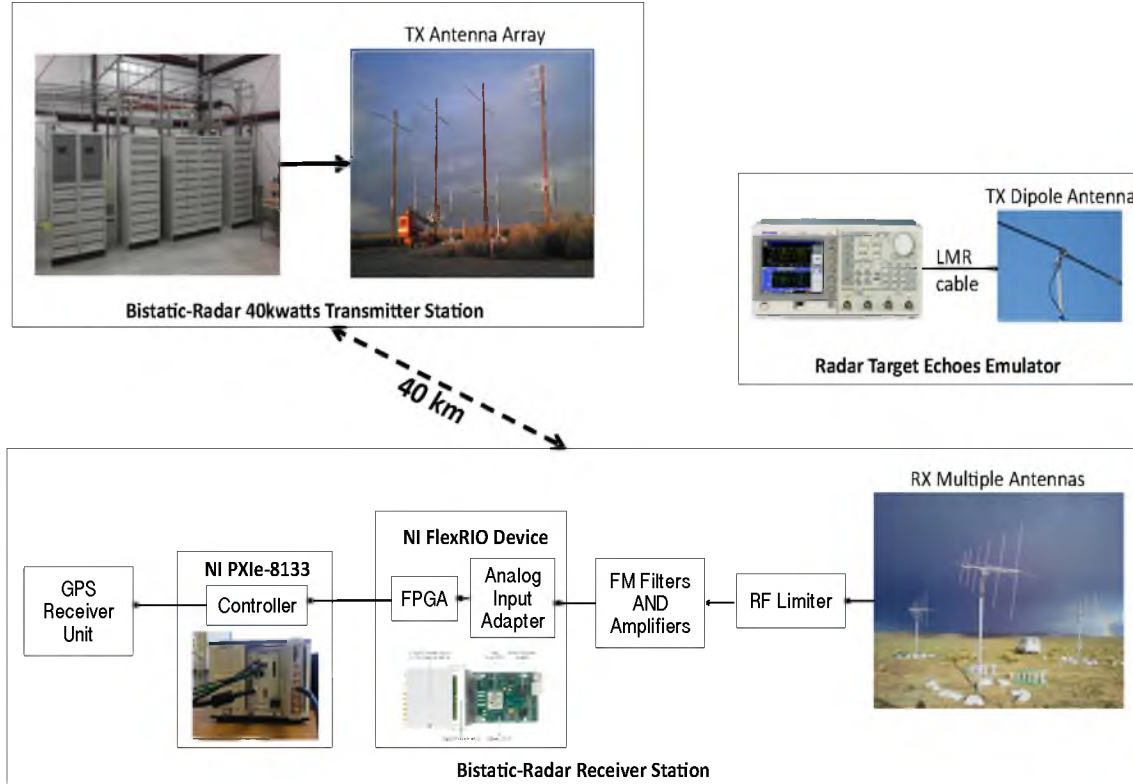
Figure 4.1: Elements of the bistatic radar system.

In our design, we use the National Instruments FlexRIO system which provides an integrated hardware and software solution for a custom software defined radio DAQ. At the input, we utilize the NI-5761 adapter module with a sample rate (F_s) 250 million samples per second (MSPS). Our system-on-chip design is implemented over a Virtex-5 FPGA which is integrated with PXIe interface for host connectivity. A description of receiver DAQ's subsystems along with the DAQ implementation details are discussed in Appendix G.

In this chapter, we study the performance of the proposed rake-like receiver. For receiver testing, we conduct two basic performance tests through a series of radar measurements. First, we evaluate the performance of the proposed detector under the existing non-Gaussian environment. The goal from this test is to measure the average false-alarm rate (FAR) acquired by the proposed detector. Second, we assess the detection performance of the proposed detector for a typical chirp signal versus SNR under a specified threshold level that corresponds to a proper level of false-alarm rate.

Before we proceed with the presentation of the performance results, we make the following observation. It is clear that the system performance, for each SNR value, depends on the chosen threshold level. The FAR decreases as the threshold increases. Also, PCD increases

as the the threshold decreases. Our goal from the performed analysis in this chapter is to design our system with low FAR and almost complete PCD, for a given low SNR. This can be achieved by choosing a threshold that results in a compromise between a low FAR, while not missing detection of air shower incidents at a specified SNR level.

As mentioned before, our radar system receives multiple undesirable frequency tones which might originate from different sources around the receiver unit, including the radar carrier signal (54.1 MHz). These persistent tones are powerful, specifically the carrier signal, and thus, lead to a high misleading RMS at the output of the matched filters. However, the observed tones can be easily filtered out. In our design, we implement a digital band-pass filter at the input stage of our detector (before the amplitude limiter) that only keeps the band of interest.

4.2   Performance Evaluation

Detection performance of the rake-like receiver has been evaluated under two test signal conditions: noise only or signal plus noise. The ability to detect a received chirp signal in background noise depends on the ratio of the signal power to the background noise power. Radar carrier power dominates the background so two quantities are used to describe the background noise. First, we define the ratio of the test chirp signal power to the radar carrier power over the time interval that chirp presents as the signal-to-carrier ratio (SCR). Second, we define the ratio of the test chirp signal power to the noise power at the input of the rake-like receiver, after filtering out the radar carrier, as the signal-to-noise ratio (SNR), viz.,

$$\text{SNR} = \frac{P_c}{\sigma_\nu^2}, \tag{4.1}$$

where P_c is the chirp signal power and σ_ν is the standard deviation of the background noise after filtering out the carrier signal.

4.2.1   False-Alarm Rate

Fig. 4.2 depicts the average false-alarm rate versus a range of normalized threshold values. We define η as the normalized threshold level. For high threshold values ($\eta > 7$), we can see that false-alarm rates are relatively high. Based on our current DAQ settings, FAR of 10 Hz leads to storing 130 GB of data every day; this is very high storage and would correspond to excessive postprocessing. In order to achieve a 2 Hz false-alarm rate, η has a value of 9.5; this is a high threshold level and shall cause a degradation in chirp detection performance.
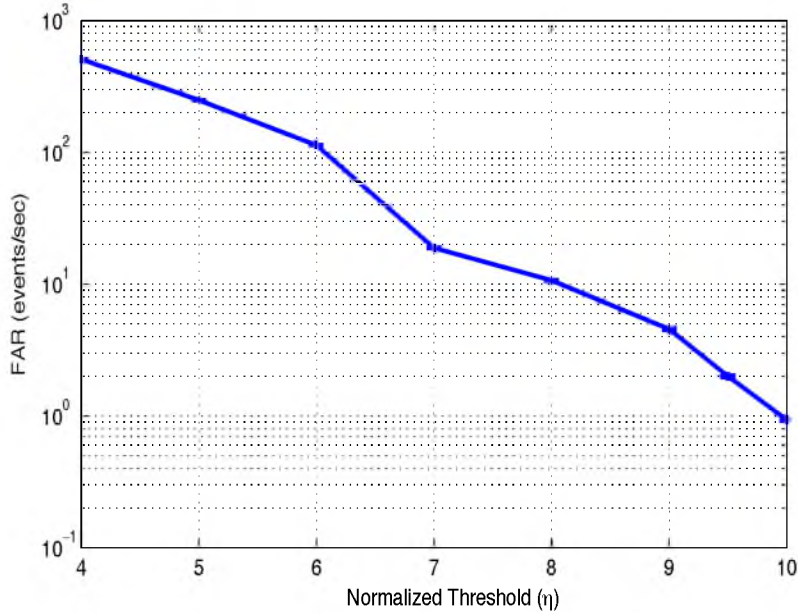
Figure 4.2: False-alarm rate versus normalized threshold (η units of the standard deviation at each filter output).

4.2.2 Probability of Correct Detection

The second test applies a theoretical chirp signal with various chirp rates and SNR values that correspond to a reasonable false-alarm rate. Based on data storage and postprocessing computational requirements, we have decided that a false-alarm rate of ~ 2 Hz is reasonable. Due to scarceness of real events, we alternatively placed artificially-generated chirp signals in the same background for evaluating the detection performance. Artificially generated chirp signals are transmitted *in situ* to the receiving antennas by an arbitrary waveform generator (AFG 3101; Tektronix, Inc.) and a dipole antenna.

A periodic, linear chirp with -1 MHz/μs rate is embedded in a real receiver site background wave form. Fig. 4.3 shows the spectrogram of a chirp embedded with -10 dB SNR and -40 dB SCR value.

Fig. 4.4 shows detection performance for a 2 Hz false-alarm rate. As seen, the minimum SNR for which complete detection is achieved is 2.5 dB. This poor performance is expected due to the high threshold level.

To better understand the reason behind the significant amount of false-alarm rates at lower threshold levels, we carefully analyze the background noise components. Fig. 4.5 shows a sample of the acquired data at the field using our receiver, where FM radio signal range and noise below 30 MHz is filtered out. From the time-frequency representation, we can deduce that the background noise is punctuated with deceptive single-frequency tones
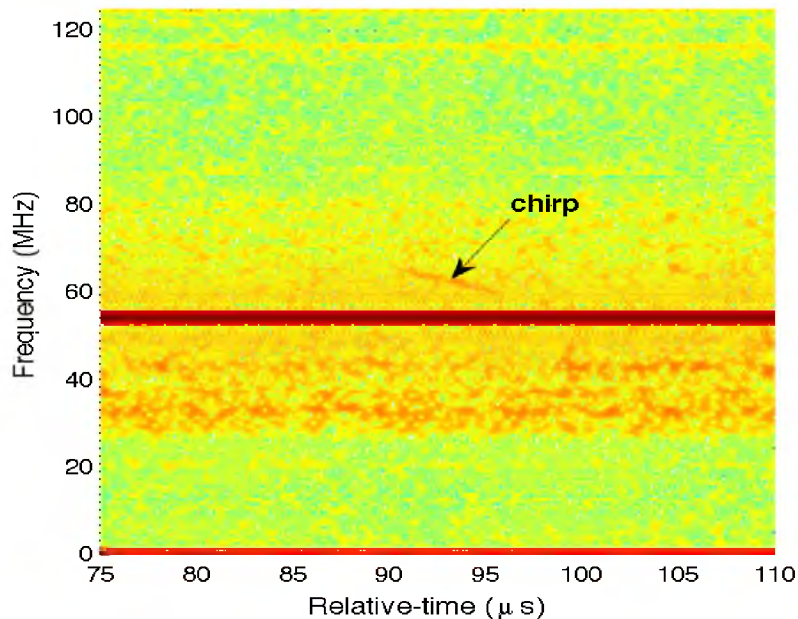
Figure 4.3: Time-frequency (spectrogram) representation of a linear, -1 MHz/μs, -10 dB SNR received chirp signal as recorded by the DAQ system.

and random noise spikes. The major source of false-alarm is the sudden noise spikes as they cover wide frequency bands and arrive at random instants of time. These spurious signals cause an erroneous radar detection decision by exceeding the detection threshold and thus, lead to high and variable false-alarm rates, even at high threshold levels.

To confront this challenge, a robust signal processing technique is needed to filter the random noise spikes and thus, we would be able to bring the threshold lower and enhance the detection performance. In the next two chapters, we work out two different solutions for this problem. In Chapter 5, we introduce a simple technique that alleviates the effect of transient background and thus, significantly enhances the detection performance of nondeterministic chirp signals. In Chapter 6, we introduce a smart time-frequency domain method that can efficiently filter the existing non-Gaussian components to a great extent.
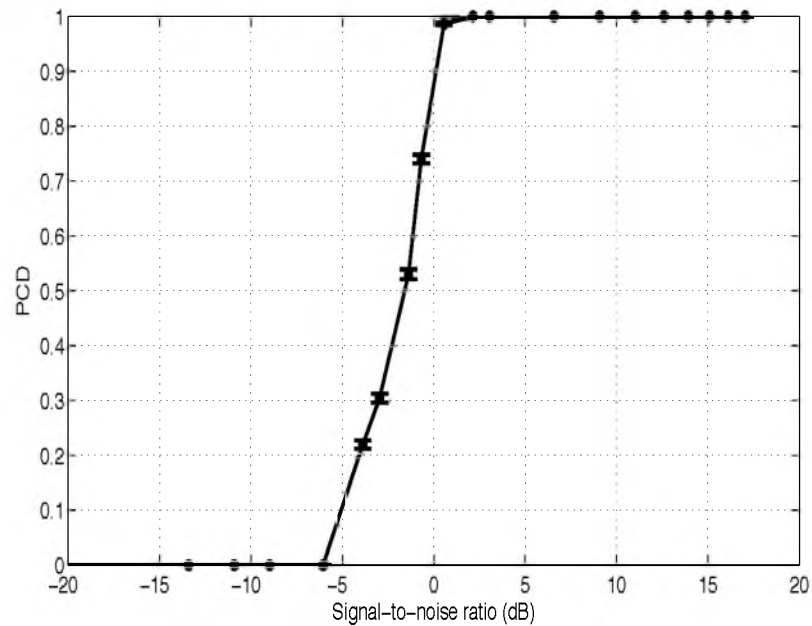
Figure 4.4: Probability of correct detection for the rake-like receiver with $\eta = 9.5$ and false-alarm rate of ~ 2 Hz.
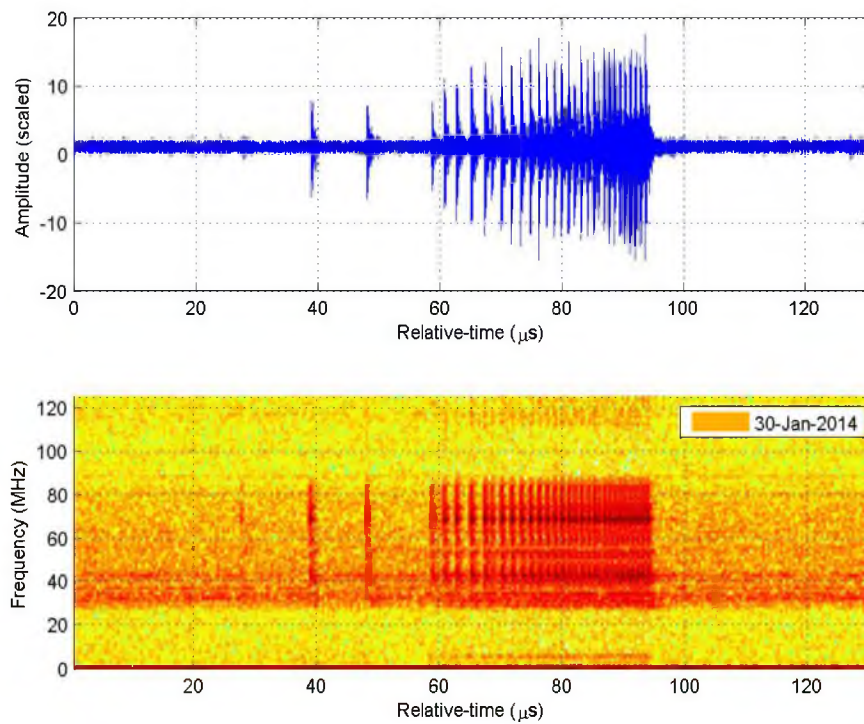
Figure 4.5: Spectrogram of background noise sample at the field.

CHAPTER 5

AMPLITUDE LIMITER FOR TRANSIENT
BACKGROUND ALLEVIATION

In our radar application, we strive to extract every bit of performance that we are able to coax from our system. A few dB additional gain of signal-to-noise ratio (SNR) is possible to achieve with a significant increase in transmitted power. In this chapter, we study the influence of amplitude limiting the noisy signal prior to the rake-like receiver to alleviate the effect of the high amplitude spikes. This simple technique would allow us to set the detection threshold as low as possible and enhance the ability of detecting signals of signal-to-noise ratio (SNR) in negative dB range.

5.1 Proposed Amplitude Limiter

The background signal of our radar receiver is observed to be impulsive or spiky. These predominant spikes represent the main source of false-alarms due to their coverage of wide frequency bands. Consequently, the threshold of our proposed detector must be raised in order to keep the desired level of false-alarm rate sufficiently low. This challenge gives rise to the need for smart analysis to reduce false-alarms while keeping the detection threshold as low as possible to avoid miss-detection of the rare events. Optimally, impulsive noise should be removed. This can be achieved through complete knowledge of the distinct features of the transient signals in time and frequency domains. However, in our application, impulsive noise statistics are observed to have time and frequency varying characteristics. Thus, we resort to a suboptimal approach that would mitigate the effect of noise spikes and significantly reduce the number of false-alarms.

In this section, we propose adding an amplitude limiter that filters out the high-amplitude spikes for reducing the number of false-alarms. In the context of this dissertation, we consider the case in which clipping is performed at an arbitrary level.

As shown in Fig. 5.1, we assume that the amplitude limiter clips the amplitude of the received signal to a factor k of its root mean square (RMS) value before clipping. The
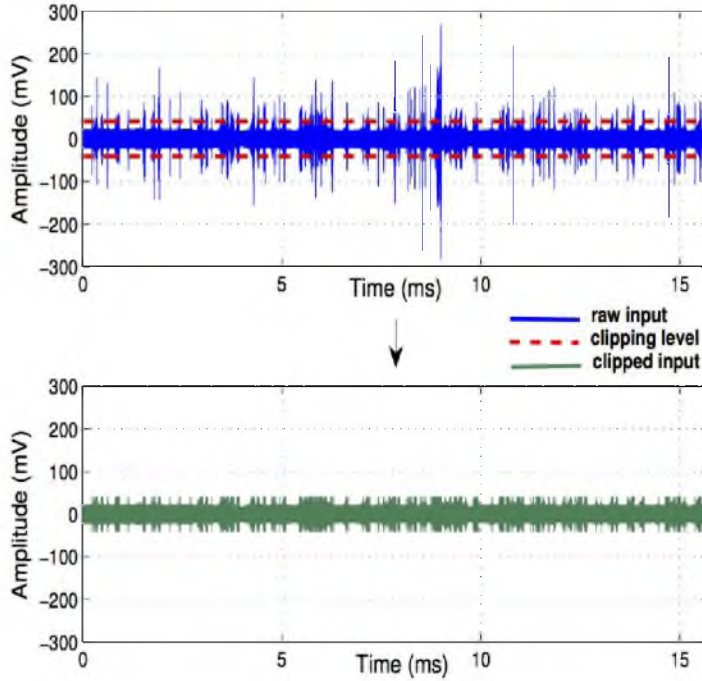
Figure 5.1: Clipping at an arbitrary level of raw input signal.

amplitude limiting process can be mathematically modeled as

$$\begin{cases} y = x, & |x| < k\sigma_s \\ y = k\sigma_s, & x > k\sigma_s \\ y = -k\sigma_s, & x < -k\sigma_s, \end{cases} \tag{5.1}$$

where x is the raw input, y is the amplitude limited output, and σ_s is the RMS value of the signal before clipping. Obviously, the use of the limiter circuit results in reducing the relative power ratio of the transient signals. In addition, clipping lowers the signal RMS or the mean-square amplitude.

In the next section, we repeat our experimental results and conduct two basic performance tests through a series of radar measurements. First, we evaluate the performance of the proposed detector under the existing non-Gaussian environment. The goal from this test is to measure the average false-alarm rate (FAR) acquired by the proposed detector and evaluate the expected improvement that could be achieved by varying the clipping level of the proposed amplitude limiter. Second, we assess the detection performance of the proposed detector for a typical chirp signal versus SNR under a specified threshold level that corresponds to a proper level of FAR. The FAR is expected to decrease as the amplitude limiter level decreases. Our goal from the performed analysis in this section is to design our

system with low FAR and almost complete PCD, for a given low SNR. This can be achieved by choosing a threshold and amplitude limiter level that results in a compromise between a low FAR, while not missing detection of air shower incidents of a specified SNR level.

5.2 Intuitive Understanding of the Amplitude Limiter's Impact

In our analysis, we consider the case of clipping the amplitude of chirp signals at an arbitrary level above the level of the noise, i.e., $k > 1$. This corresponds to clipping chirp signals with positive SNR values. In this section, we study the impact of the amplitude limiter on chirp detection performance.

We design our system to achieve complete PCD, for a given low SNR, with a low and fixed FAR. In order to achieve this criteria, we would need to set our detection threshold as low as possible to avoid missing detection of air shower incidents at a specified SNR level. From our reported results in Chapter 3, this corresponds to $\eta < 8$, where η is the normalized threshold level. Clearly, for these low threshold values, our rake-like receiver is able to detect negative SNR chirps and thus, clipping positive SNR chirps should still result in complete PCD.

Fig. 5.2 demonstrates the effect of clipping a chirp signal on the correlation sum at the output of the filter. Although the signal is clipped (less energy), it still matches the polarity of the original chirp signal and that results into a high peak value sufficient to exceed nominal threshold values.

To better understand the amplitude limiter's impact, consider receiving a positive SNR chirp signal (10 dB) of a 5 MHz bandwidth and -1 MHz/μs rate. We carefully look at the output of the first matched filter in the rake-like receiver whose slope is κ equals -1 MHz/μs.

Fig. 5.3 (a) shows the time-domain representation of a chirp signal before and after applying the amplitude limiter. Clearly, the limiter distorts the chirp signal and, hence, we expect a smaller correlation/signal peak at the filter output. Fig. 5.3 (b) shows the output of the filter due to the chirp and its clipped version. As depicted, the peak value of the filter's output due to clipped chirp is still significantly higher than the set threshold ($\eta = 8$). In Fig. 5.4, we repeat the same test for a lower clipping level ($k = 1$) and yet, we see the amplitude limiter does not degrade detection performance of chirp signals, although hard-clipping is performed.

In the next section, we study the influence of the amplitude limiter on the transient background and how it can efficiently remove the high amplitude transients.
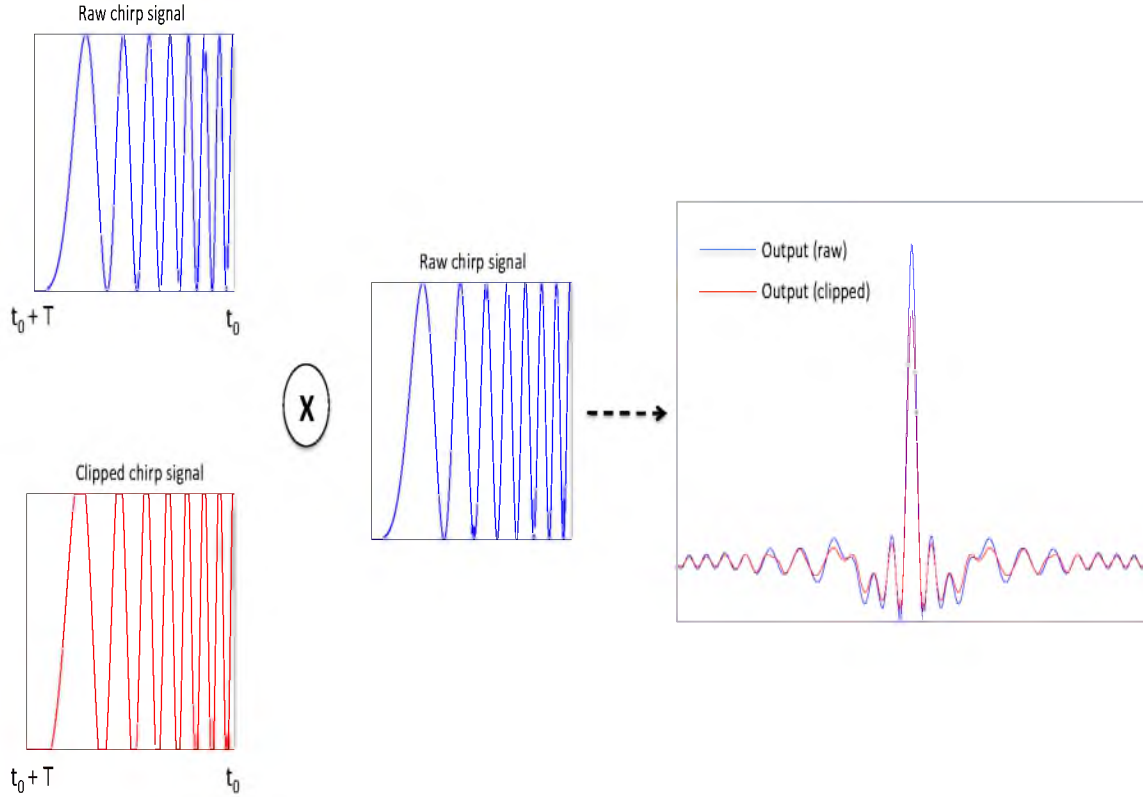
Figure 5.2: Demonstration of the amplitude limiter's effect on the correlation sum at the filter output. Raw chirp signal (blue) and clipped chirp signal (red), each is correlated with a raw chirp signal. The plot at the right shows the correlation result due to the raw chirp signal (blue) and the clipped chirp signal (red).

5.3   Performance Evaluation

Consider the following observations about performance analysis. First, it is clear that system performance depends on the chosen threshold level η (user defined, a multiple of σ_m as defined previously) for each SNR value. False-alarm rate is expected to decrease as the threshold level increases, at the expense of detection efficiency of low SNR chirp signals.

Conversely, detection efficiency increases as the threshold decreases. Second, the false-alarm rate is expected to decrease as the amplitude limiter level decreases because high amplitude transients are effectively removed. To this date, radar echoes from cosmic ray air showers have not been detected, so it is unlikely that the EAS cross section is large enough to produce such large amplitude impulses. Therefore such signals are dismissed *a priori*. Our strategy is to choose the threshold and amplitude limiter level that gives high detection efficiency for a given SNR and low false-alarm rate.

In this section, we study the performance of the proposed detector along with the amplitude limiter to understand the influence of the limiter circuit on the transient signals.
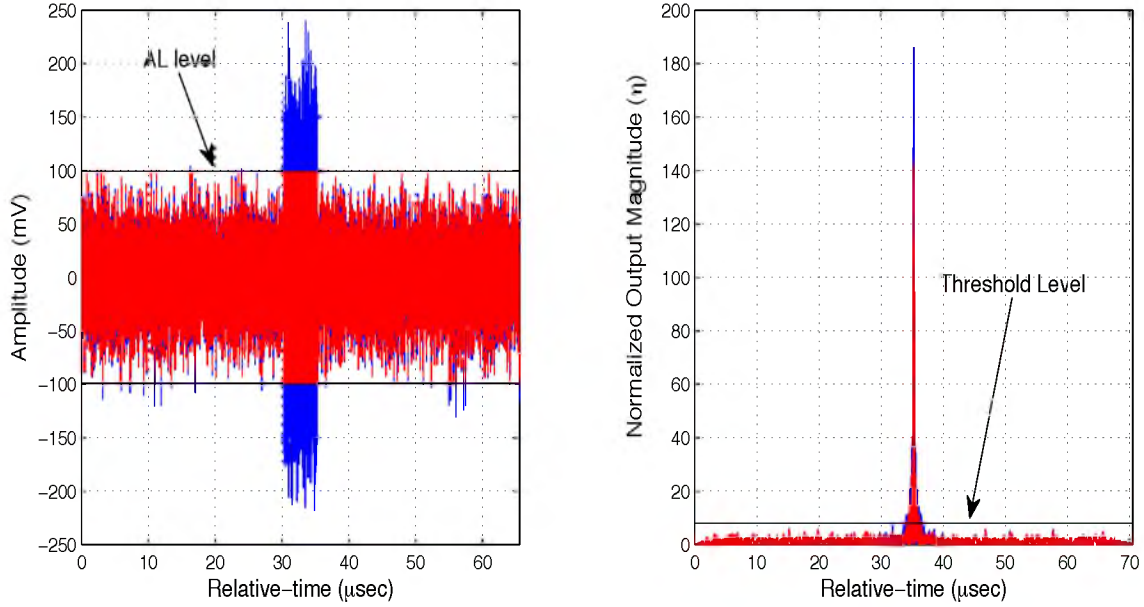
Figure 5.3: Impact of amplitude limiter ($k = 3$) on the peak value of the matched filter output. (a) Time-domain representation of a 5 MHz linear chirp with -1 MHz/μs rate before amplitude limiter (blue) and after amplitude limiter ($k = 3$) (red). (b) Normalized matched filter output due to chirp signal before clipping (blue) and after clipping (red). Threshold level (8η) is the black solid line.

We conduct two basic performance tests through a series of radar measurements to determine the ideal amplitude limiter level and the efficiency as a function of MF threshold. First, we evaluate the performance of the proposed detector under the existing non-Gaussian environment. The goal of this test is to measure the average false-alarm rate of the non-Gaussian noise environment and evaluate the improvement that could be achieved by adding the amplitude limiter and varying the clipping level. Second, we assess the detection performance for a typical chirp signal versus SNR under a specified threshold level that corresponds to a proper level of false-alarm rate.

As mentioned before, our radar system receives multiple undesirable frequency tones which might originate from different sources around the receiver unit, including the radar carrier signal (54.1 MHz). These persistent tones are powerful, specifically the carrier signal, and thus, lead to a high misleading RMS at the output of the matched filters. However, the observed tones can be easily filtered out. In our design, we implement a digital band-pass filter at the input stage of our detector (before the amplitude limiter) that only keeps the band of interest.

Fig. 5.5 depicts the false-alarm rate versus a range of threshold values for different settings of the amplitude limiter. We would typically prefer to have our detector set where
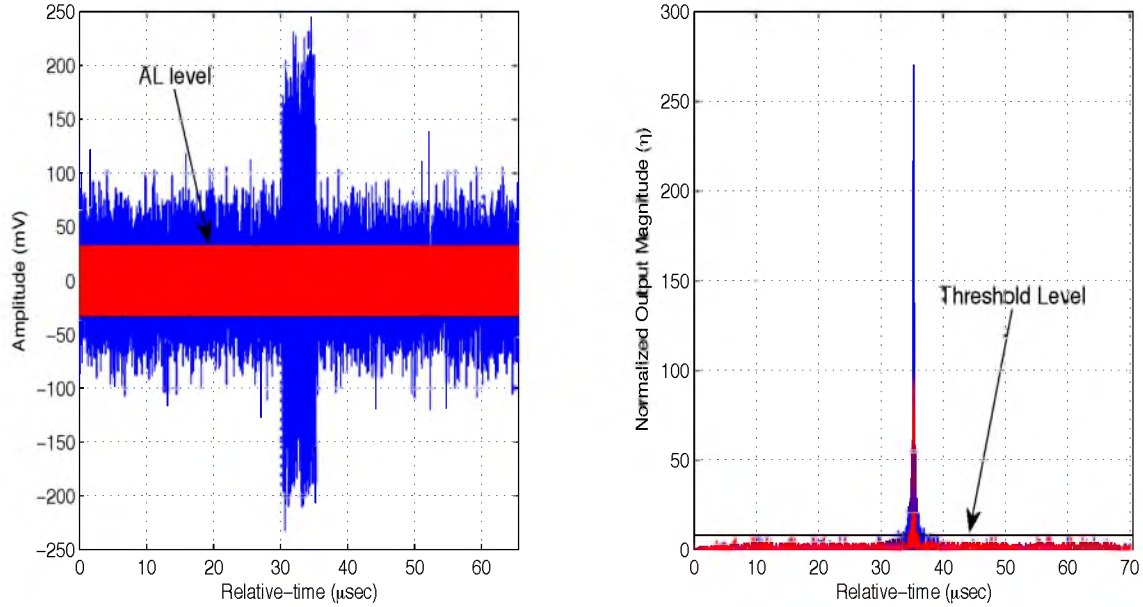
Figure 5.4: Impact of amplitude limiter ($k = 1$) on the peak value of the matched filter output. (a) Time-domain representation of a 5 MHz linear chirp with -1 MHz/μs rate before amplitude limiter (blue) and after amplitude limiter ($k = 1$) (red). (b) Normalized matched filter output due to chirp signal before clipping (blue) and after clipping (red). Threshold level (8η) is the black solid line.

the false-alarm is as low as reasonably achievable. We can see that the level of the amplitude limiter has a significant effect on reducing the false-alarm rate as a result of reducing the relative power ratio of the embedded spikes. Efficiency curves for different amplitude limiter levels (described in the next paragraphs) show that the amplitude limiter does not *decrease* detection performance of chirp signals, although they are also clipped. Results are shown in Fig. 5.5 for three different amplitude limiter levels. Consider the following interpretation of Fig. 5.5. In order to achieve a 2 Hz false-alarm rate, η has a value of six for $k = 3$ and 9.5 for $k = 10$ (black dashed line). Thus, detection thresholds can be decreased which enhances positive detection of low SNR signals.

The second test applies a theoretical chirp signal with various chirp rates and SNR values that correspond to a reasonable false-alarm rate. Based on data storage and postprocessing computational requirements, we have decided that a false-alarm rate of ~ 2 Hz is reasonable. Due to scarceness of real events, same as in the previous chapter, we alternatively placed artificially-generated chirp signals in the same background for evaluating the detection performance. Artificially generated chirp signals are transmitted *in situ* to the receiving antennas by an arbitrary waveform generator (AFG 3101; Tektronix, Inc.) and a dipole
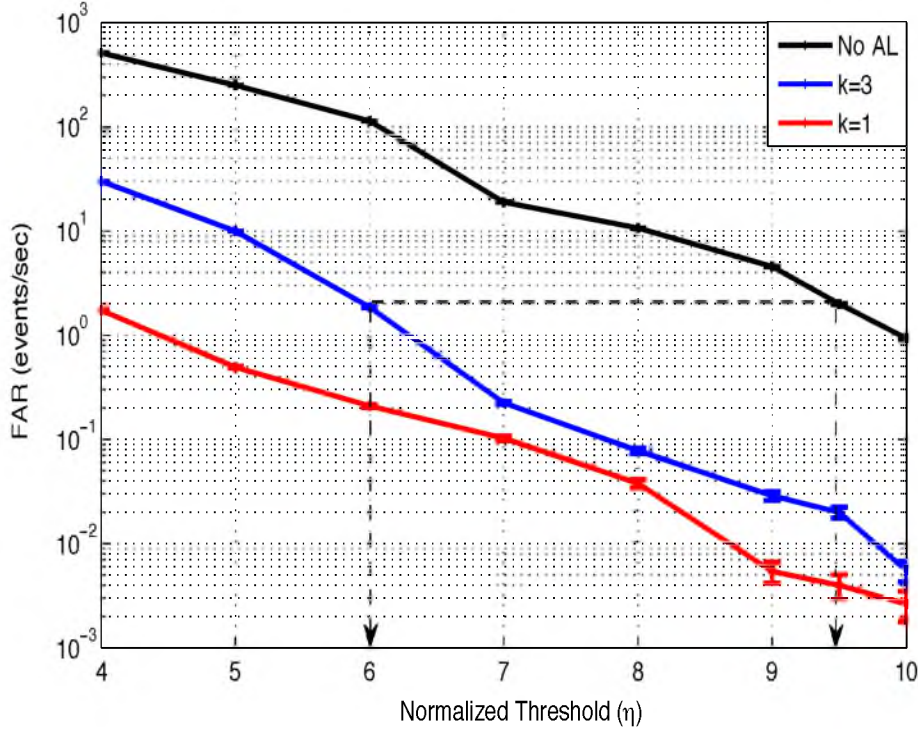
Figure 5.5: False-alarm rate versus relative threshold (η units of the standard deviation at each filter output) for different amplitude limiter levels.

antenna. Both linear chirp signals and a simulated radar echo are used in measuring detection performance.

5.3.1 Linear Chirp Signal

A periodic, linear chirp with -1 MHz/μs rate is embedded in a real receiver site background wave form. Fig. 4.3 shows the spectrogram of a chirp embedded with -10 dB SNR and -40 dB SCR value.

Fig. 5.6 shows detection performance for a 2 Hz false-alarm rate. Efficiency is shown for cases where the amplitude limiter is removed and at two different levels that result in the same false-alarm rate, each with different threshold levels. The minimum SNR for which complete detection is achieved is 5 dB when no amplitude limiter is applied, 0 dB for $k = 10$ (*soft clipping*), -6 dB for $k = 3$ (*hard clipping*). These results imply that by using the amplitude limiter, high detection performance can be achieved with low complexity. To maximize detection ability, the amplitude limiter is currently fixed at $k = 3$.
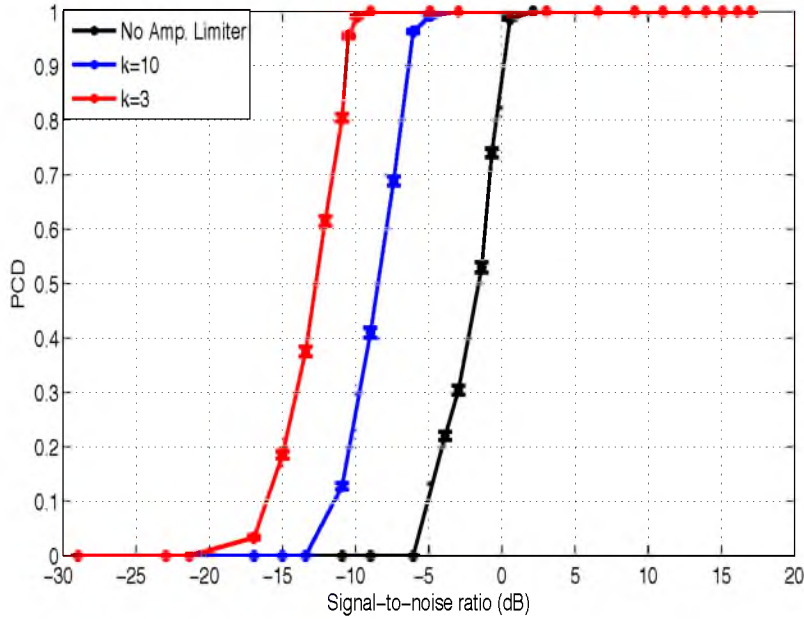
Figure 5.6: Probability of detection for the rake-like receiver.

5.3.2 Simulated Air Shower

In a more realistic test, a simulated radar echo from a 10 EeV air shower inclined 30°
out of the $TX \rightarrow RX$ plane and located midway between the transmitter and receiver
is scaled and transmitted to the receiving antennas using a function generator. Fig. 5.7
shows a spectrogram of the received waveform with 5 dB SNR and -25 dB SCR. The echo
is broadband (about 25 MHz) and short in duration (10 μs). Detection efficiency of the
emulated chirp is shown in Fig. 5.8. The minimum SNR for which complete detection is
achieved is -7 dB.
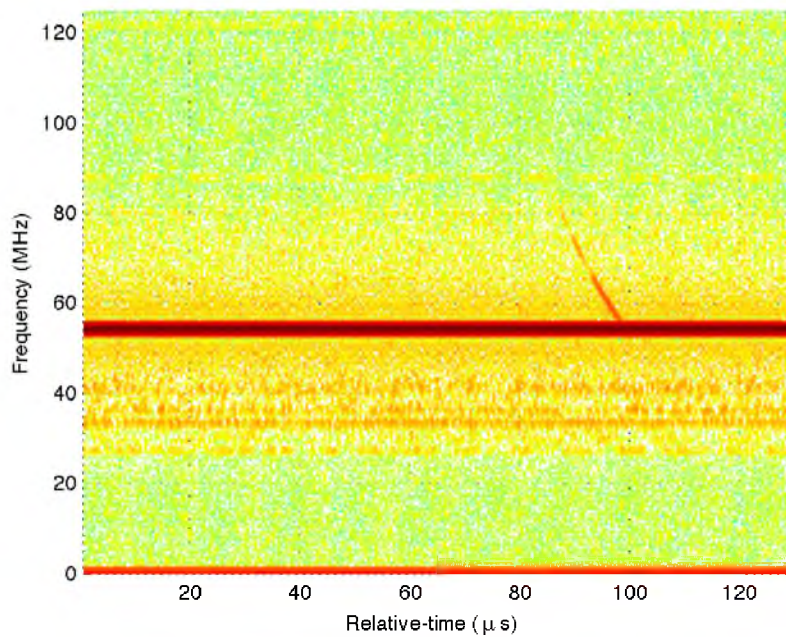
Figure 5.7: Spectrogram of simulated air shower radar echo with 5 dB SNR. The radar echo is from a simulated shower inclined 30° out of the $TX \rightarrow RX$ plane and located midway between the transmitter and receiver.
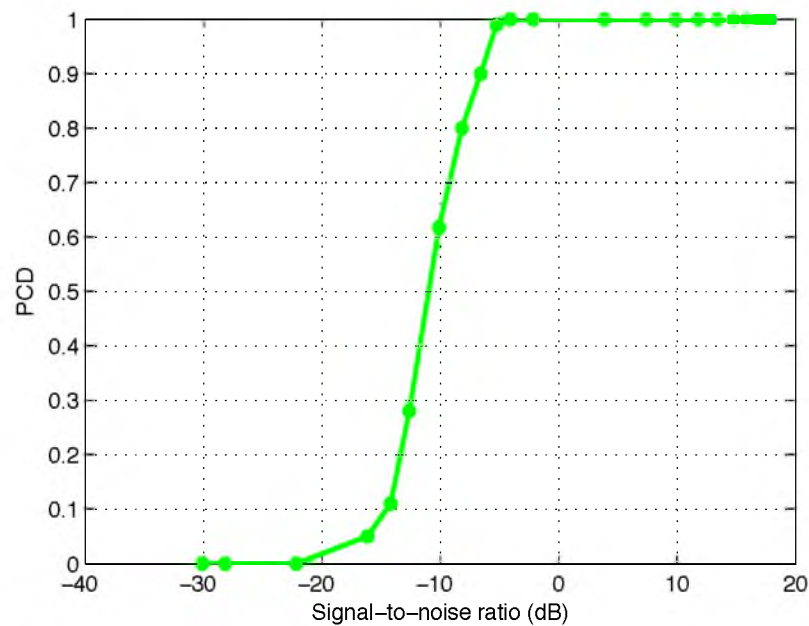
Figure 5.8: Probability of correct detection for the rake-like receiver using $\eta = 6$ for a simulated air-shower echo that is scaled and emulated with a function generator.

CHAPTER 6

HOUGH TRANSFORM-BASED CHIRP DETECTOR

In our detection problem, two different signal spaces are considered. The first space is obtained by applying DFT to segments of the received signal. This is referred to as *TF-space*. The second space is obtained by applying Hough-transform to points in TF-space, hence termed as *HT-space*. We note that here we are dealing with discrete-time signals in both TF-space and HT-space. Accordingly, for each sample set, TF-space and HT-space are represented by a pair of matrices. For clarity of presentation, we refer to the elements of TF-space matrix as *points*, and to the elements of HT-space matrix as *cells*.

In processing TF-space points, we introduce a *TF-threshold* γ and only points which exceed γ are Hough-transformed. We also introduce an *HT-threshold* ζ and whenever the amplitude of a cell in the HT-space exceeds ζ, signal detection is declared.

In this chapter we evaluate the detection performance of the proposed detector. A false-alarm is declared when in the absence of a chirp signal, one of the cells in the HT-space exceeds ζ, and *probability of false-alarm* (PFA) is measured accordingly. The average number of false detections per unit of time is defined as the false-alarm rate (FAR). In presence of a linear chirp, when the amplitude of at least one of the cells in HT-space exceeds ζ, we say a correct detection has occurred, and accordingly define the *probability of correct detection* (PCD). The complement of PCD is termed *probability of missed-detection* (PMD).

6.1   HT-Based Detection Algorithm

Hough transform (HT) is a pattern detection technique that is commonly used in digital signal and image processing. It is frequently used as a robust method for finding lines in noisy backgrounds [40, 47]. The main premise of the technique is transforming the spatial image pattern into a space of possible parameter values [48]. In that sense, HT converts a complex pattern detection problem in time-frequency space "*TF-space*" into a simple

peak detection problem in Hough-transform space *"HT-space."* In the following context we focus, in particular, on using HT for linear chirp detection. TF-space in this case is the time-frequency representation of the received signal samples, and the variables of HT-space are those used to determine the linear variation of the instantaneous frequency in TF-space, viz., chirp parameters.

The TF-space is represented by (t,f), where t is the time and f is the frequency; see Fig. 6.1(a) . The HT-space, on the other hand, is represented by (κ,c), where κ is the linear chirp slope and c is the chirp intercept (the intercept of the line with the c axis in the (κ,c) plane) or the initial frequency.

In our analysis, we use short time Fourier transform (STFT) as a mean of signal evaluation in time-frequency plane. The incoming data samples, symbolized in vector format as $\mathbf{x}$, are divided into overlapping data blocks in time. Each data block "segment" is chosen to be short enough so that the signal can be considered stationary within the segment. The choice of the data block size is based on a tradeoff between temporal and frequency resolution. For each data block, a windowing function $\mathbf{w}$ is applied to localize the signal energy in time and then N-point DFT is applied to each windowed segment.

The N-point discrete-time STFT at time m can be described mathematically as [49]

$$X_{n,m} = \sum_{i=0}^{N-1} x_i w_{i-m} e^{-j2\pi n \frac{i}{N}}, \quad n = 0, 1, \ldots, N-1 \tag{6.1}$$

where n and m denote the corresponding frequency index and data-block index, respectively. The window sequence w_m is assumed to be nonzero in the interval $[0,N\text{-}1]$, where N is the number of window samples.

In our application, expected radar echoes lie within a specific frequency band. We take advantage of this feature by only considering the bandwidth of interest. We denote the indices of the *start* frequency and the *end* frequency as n_1 and n_2, respectively, and we note that $N_b = n_2 - n_1 + 1$ is the number of frequency indices that cover the band of interest.

Complex values $X_{n,m}$ are considered as elements of a matrix $\mathbf{X}$, known as spectrum matrix, that we refer to as

$$\mathbf{X} = [X_{n,m}], \quad n = n_1, n_1 + 1, \ldots, n_2; m = 0, 1, \ldots, M - 1 \tag{6.2}$$

where M defines the number of recorded time-blocks. The magnitude squared of the elements of $\mathbf{X}$ yields to the TF-space matrix

$$\mathbf{S} = [|X_{n,m}|^2], \quad n = n_1, n_1 + 1, \ldots, n_2; m = 0, 1, \ldots, M - 1. \tag{6.3}$$
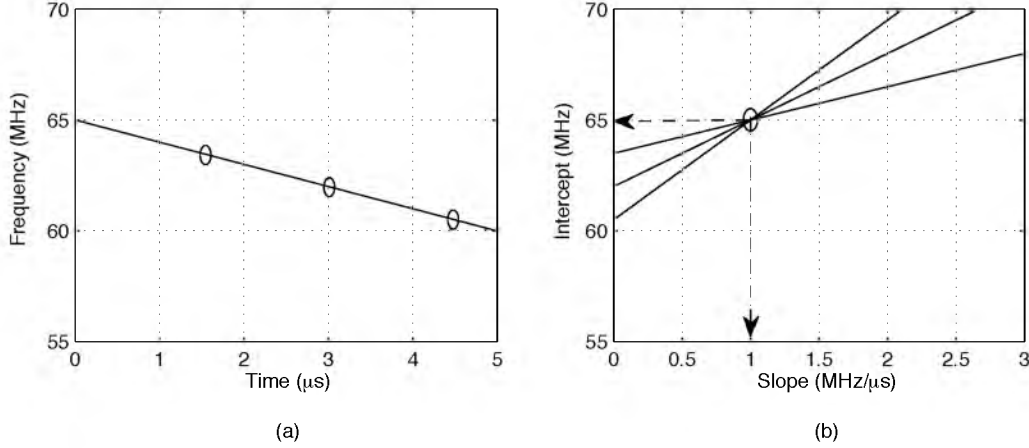
Figure 6.1: Illustration of HT for a linear downward chirp with slope -1 MHz/μs, start frequency 65 MHz, and bandwidth 5 MHz.

Each element in **S** is compared to the *TF-threshold* γ. We choose γ as γ_0 times η, where η is the mean of the entries of **S**. The parameter γ_0, thus, may be thought as the normalized version of γ with respect to the background noise. This way, the HT scheme that we adopt is capable of tracking the noise level. Time-frequency points that exceed γ, signified by the parameters (t_m, f_n), known as seed points, are transformed into the following lines in HT-space

$$c_k = f_n - t_m \kappa_k. \tag{6.4}$$

Moreover, each line is weighted by the amplitude of its corresponding seed point in the TF-space matrix. The mapped lines to HT-space are then integrated to form the *accumulator-matrix*, which is initially reset to zero. For more clarity, equation (6.4) can be manipulated in the following form

$$f_i = \kappa_k t_i + c_k, \quad i = n_1, n_1 + 1, \ldots, n_2 \tag{6.5}$$

which shows that a single cell (κ_k, c_k) in the HT-space corresponds to a single straight line in the TF-space. Accordingly, lines of the HT-space that are mapped from collinear points in the TF-space all intersect at a common cell in the HT-space resulting in a local peak as shown in Fig. 6.1(b). If the peak is detected, the corresponding line in TF-space can be easily located.

In the case of deterministic chirp detection, the cell in HT-space at which the peak happens is known. However, in our case, we are interested in detecting a linear chirp signal with unknown parameters and thus, the local peak detection problem is translated to a

peak searching over a range of locations. Detection occurs when the amplitude of any of the accumulator-matrix cells exceed ζ. We choose $\zeta = \zeta_0 \gamma$, where ζ_0 may be thought as a normalized version of ζ. Also, recalling the relationship $\gamma = \gamma_0 \eta$, one may note that the choice of ζ also relates to the level of the background noise, hence, the method adopted in this chapter has a noise tracking capability. We consider an incremental advance of the spectrum matrix for each accumulator-matrix computation. The step size of the incremental advance can be defined as the sampling-period of the TF-space T_s, whose minimum value is 1 time-sample. If T_s is set to its minimum value, the accumulator-matrix can be efficiently computed from the results of the previous accumulator-matrix without missing any possible detection and effectively reducing the number of possible false-alarms. On the other hand, if a chirp exists, the corresponding detection instant is variable and occurs for an indefinite received-percentage of the chirp. Fig. 6.2 shows the advance of a linear chirp signal in time that conveys the stated observation. In this chapter, we consider the detection to be declared from the first detection instant then we start observing the TF-space for future chirps after skipping M samples.

6.2   Image Space Properties

The choice of the window function and its related parameters plays an important role in the localization of the signal in the time-frequency plane and thus, minimizing spectrum leakage. In the following subsections, we shed more light on the window related parameters.

6.2.1   Window Type

The window function is selected to localize the signal energy in time and avoid time discontinuities. The window type is chosen to trade off the width of its main lobe and attenuation of its side-lobes.
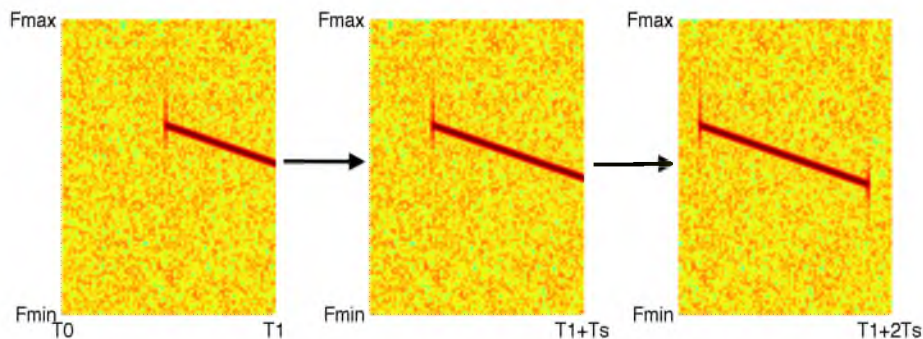
Figure 6.2: Advance of chirp signal in time.

The rectangular window is defined as

$$w_i = \begin{cases} 1, & 0 \leq i \leq N_w - 1 \\ 0, & \text{otherwise.} \end{cases} \tag{6.6}$$

The two signals x_i and w_i are multiplied in the time-domain where the corresponding operation in the frequency domain is a circular convolution of the spectra. Despite being the simplest window, rectangular window has very strong side-lobes and thus, poor localization in the frequency domain.

6.2.2 Window Length

The choice of window length of the spectrogram is crucial as it should be selected during the time in which the spectral characteristics are nearly constant. It provides a compromise between temporal and frequency resolution: a shorter window size means more temporal localization but less spectral discrimination. In other words, if the selected window is too short, STFT introduces significant smearing of temporal and spectral information (blurring) which can distort the spectral information over time [50]. However, for a too long window, STFT fails in capturing the rapid changes of the spectral content. For a linear chirp signal of constant amplitude, using a rectangular window, the optimal window length is given by [51]

$$T_w = \sqrt{\frac{2}{|\kappa|}} \quad \text{seconds.} \tag{6.7}$$

6.2.3 Window Overlapping Percentage

In our detection problem, we aim to obtain the maximum possible number of collinear points using the minimum possible number of computations. The choice of the amount of overlapping between successive windows can be seen as a trade-off between the number of collinear points and the number of time-blocks per a single spectrum matrix.

6.3 Radar Background Challenges

In our application, radar events are very rare, probably a few events per week, and occur at random instants of time. Thus, noise reception is expected to be dominant. This challenge gives rise to the need for smart background analysis to reduce false-alarms while keeping the detection threshold as low as possible to avoid miss-detection of the rare events. Fig. 6.3 shows a sample of acquired data at the field, where FM radio signal range is filtered out. From the time-frequency representation we can deduce that the noise background is
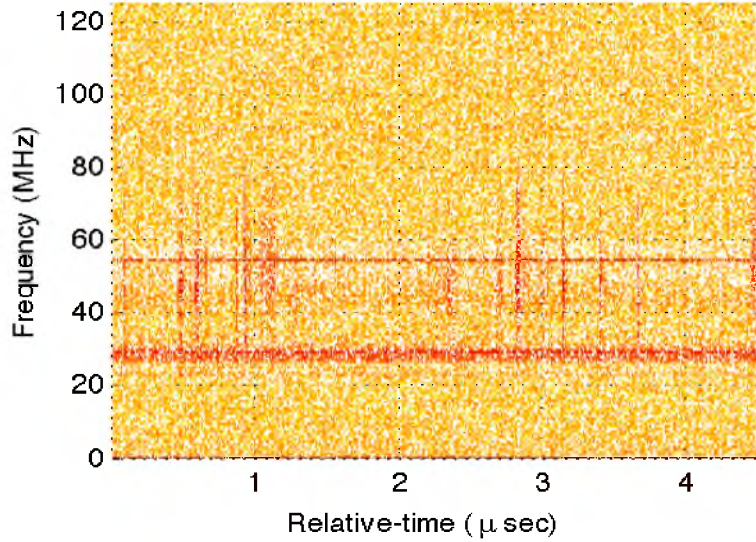
Figure 6.3: Spectrogram of background noise at the receiver site. Frequency and time are on the vertical and horizontal axes, respectively, with color representing the power in a particular frequency component. The carrier signal is represented by the horizontal line at 54.1 MHz. Broadband transients are the vertical lines and stationary noise sources are the horizontal band near 30 MHz.

rich with multiple undesirable components, including stationary signals as the persistent frequency tones located at 28.5MHz and 54.1MHz as well as the broadband transient signals that are randomly located in time-domain. In this section, we investigate the background signal components and explore some additions to the HT detector for reducing the number of false-alarms, speeding-up the detection test, yet without degrading the detection efficiency.

6.3.1 Powerful Tones

When frequency-tones are received within the band of interest, they share the linear variation in time-frequency plane with the expected linear-chirps, but with a zero slope. These tones can be easily discerned in the HT-space and their effect can be alleviated by neglecting their corresponding local-peaks located at $(\kappa = 0)$ cells so that other peaks can be investigated using the same procedure. However, the strength of powerful tones lies beyond their misleading local-peaks as they also result in a grid of high-variance cells that may accumulate in time and result in false peaks that are randomly located. Thus, we identify the presence of powerful tones for each computed TF-space matrix, then the detected components are excluded from the test simply by forcing them to zero, so that other time-frequency points are investigated.

6.3.2   Noise Spikes

Transient signals "spikes" are very common in our scenario and they represent the main source of false-alarms due to their coverage of wide frequency bands. Consequently, the threshold of our proposed detector must be raised in order to keep the desired level of false-alarm rate sufficiently low. This challenge gives rise to the need for smart analysis to reduce false-alarms while keeping the detection threshold as low as possible to avoid miss-detection of the rare events. Narrow spikes are also featured by their high slopes in time-frequency plane (almost vertical lines). After Hough transformation, they produce local-maxima in the accumulator-matrix, which shall be collocated at the maximum slope-points. Consequently, they can be neglected due to the prior knowledge of the expected range of chirp-slopes and then searching process for chirps continues.

6.4   Detection Analysis

In the previous section, we explored the time-frequency domain features that efficiently filter the undesirable noise components, and hence, our radar problem is reduced to signal detection in a white-Gaussian noise background.

First, we note that the signal of interest has the form of

$$c_i = \text{rect}\left(\frac{i}{N_c}\right)\cos\left(\theta_i\right), \quad i = 0, 1, \ldots, N_c - 1 \tag{6.8}$$

where rect($\cdot$) denotes the rectangular function, i denotes the time index, N_c denotes the number of chirp signal samples, and the time-varying phase θ_i is expressed as

$$\theta_i = 2\pi f_\text{C} i - \pi \kappa i^2, \quad i = 0, 1, \ldots, N_c - 1 \tag{6.9}$$

where f_C denotes the chirp center frequency, f_H start (high) frequency and f_L end (low) frequency.

The received signal x_i, thus, is modeled as

$$x_i = c_i + \nu_i, \quad i = 0, 1, \ldots, N_c - 1 \tag{6.10}$$

where ν_i is an additive white-Gaussian noise (AWGN). For our radar application, we consider two received signal hypotheses: either noise only (H_0) or signal-plus-noise (H_1). As mentioned in Section 6.1, a detection is declared when the amplitude of any of the accumulator-matrix cells exceed the HT-threshold.

For H_0, we wish not to detect anything and thus, minimize false-alarms. However, for H_1, we wish to detect the chirp signal with a high probability, when it exists. In other

words, we wish to choose the pair of thresholds (γ, ζ) such that, for a given signal-to-noise ratio (SNR), leads to a PCD close to one, while keeping a reasonably low value of PFA. The pair of thresholds' selection is subject to a compromise between aiming at high detection efficiency to avoid missing real radar events and maintaining a low level of false-alarms to keep storage low and, hence, accelerating the offline processing of the stored data.

6.4.1 H_0: Chirp Signal Absence

We assume the Gaussian noise samples ν_i have a zero mean, are independent and identically distributed, and have a variance of $\sigma_\nu^2 = 1$. Thus, one can deduce that the corresponding elements of the TF-space matrix $\mathbf{S}$ are exponentially distributed [52]. Hence, the probability of each element of $\mathbf{S}$ exceeding the TF-threshold γ is obtained as

$$
\begin{aligned}
P_{\mathrm{n}} &= P(s > \gamma) \\
&= \int_\gamma^\infty e^{-s} ds \\
&= e^{-\gamma}, \qquad 0 < \gamma < \infty
\end{aligned} \tag{6.11}
$$

Here, the subscript "n" is to signify that the probability term arises from noise only. Each time-frequency point exceeding γ contributes to a number of cells in the HT-space. We denote the maximum number of time-frequency points that can participate in a given cell in the HT-space as L_j, where j is the cell index. We note that L_j varies from one cell to another.

6.4.1.1 Single Cell

First, we focus our interest on studying a given cell in the HT-space that corresponds to an arbitrary chirp intercept with index n_0 and chirp rate with index k_0. In this case, L_j equals L_0. Consider the case where l seed points out of L_0 to have exceeded the TF-threshold and use s_i to denote the corresponding elements of $\mathbf{S}$. The accumulated cell value in the HT-space is then given by

$$
a_0 = \sum_{i=1}^l s_i \, . \tag{6.12}
$$

Next, we note that

$$
P(a_0 > \zeta | H_0) = \sum_{l=1}^{L_0} P(\forall i : s_i > \gamma | H_0) P(a_0 > \zeta | \{\forall i : s_i > \gamma\}) \tag{6.13}
$$

where, here, $\forall i$ is the shorthand notation for "for all values of i in the range of 1 to l." Using (6.11), the first probability on the right-hand side of (6.13) is calculated as

$$P(\forall i : s_i > \gamma | H_0) = \binom{L_0}{l} P_{\mathrm{n}}^l (1 - P_{\mathrm{n}})^{L_0 - l}. \tag{6.14}$$

The second probability term on the right-hand side of (6.13) can be evaluated as

$$P(a_0 > \zeta | \{\forall i : s_i > \gamma\}) = \int_\zeta^\infty P(a_0 | \{\forall i : s_i > \gamma\}) . \tag{6.15}$$

Since all the s_is are independent random variables then the probability distribution of their sum, a_0, is the result of convolving the probability distributions of individual s_i. The probability density function (PDF) of a single random variable s_i given that s_i exceeded γ is

$$
\begin{aligned}
P(s_i | s_i > \gamma) &= \frac{P(s_i)}{P(s_i > \gamma)}, \quad s_i \in [\gamma, \infty) \\
&= \frac{P(s_i)}{P(s_i > \gamma)} u(s_i - \gamma) \\
&= e^{-(s_i - \gamma)} u(s_i - \gamma) \tag{6.16}
\end{aligned}
$$

where $u(\cdot)$ denotes the unit step function. We note that the convolution of l exponential variates leads to a chi-squared distribution with $2l$ degrees of freedom [53]. Hence,

$$P(a_0 | \{\forall i : s_i > \gamma\}) = \frac{(a_0 - l\gamma)^{l-1}}{(l-1)!} e^{-(a_0 - l\gamma)} u(a_0 - l\gamma). \tag{6.17}$$

Using the PDF in (6.17), one will obtain the following result

$$
\begin{aligned}
P(a_0 > \zeta | \{\forall i : s_i > \gamma\}) &= \int_\zeta^\infty \frac{(a_0 - l\gamma)^{l-1}}{(l-1)!} e^{-(a_0 - l\gamma)} u(a_0 - l\gamma) \, da_0 \\
&= \int_{\max(\zeta, l\gamma)}^\infty \frac{(a_0 - l\gamma)^{l-1}}{(l-1)!} e^{-(a_0 - l\gamma)} \, da_0 \\
&= \int_{\max((\zeta - l\gamma), 0)}^\infty \frac{z^{(l-1)}}{(l-1)!} \, dz \\
&= \begin{cases} 1, & \zeta < l\gamma \\ \dfrac{\Gamma(l, \zeta - l\gamma)}{(l-1)!}, & \zeta > l\gamma \end{cases} \\
&= u(l\gamma - \zeta) + \frac{\Gamma(l, \zeta - l\gamma)}{(l-1)!} u(\zeta - l\gamma). \tag{6.18}
\end{aligned}
$$

Substituting (6.14) and (6.18) in (6.13), we get

$$
\begin{aligned}
P(a_0 > \zeta | H_0) = \sum_{l=1}^{L_0} \binom{L_0}{l} P_{\mathrm{n}}^l (1 - P_{\mathrm{n}})^{L_0 - l} \bigg(& u(l\gamma - \zeta) \\
& + \frac{\Gamma(l, \zeta - l\gamma)}{(l-1)!} u(\zeta - l\gamma) \bigg) \tag{6.19}
\end{aligned}
$$

where $\Gamma(x, y)$ is the incomplete gamma function, defined as, ([43], pp. 899, Eq. (8.352))

$$\Gamma(x, y) = (x - 1)! \, e^{-y} \sum_{k=0}^{x-1} \frac{y^k}{k!} \tag{6.20}$$

6.4.1.2 HT-space Matrix

In the actual problem, a number of cells out of the whole accumulator-matrix are compared against the HT-threshold ζ. A false-alarm is declared if the amplitude of any of these cells, a_j, exceeds ζ. We denote the number of cells of interest as N_s, and assume that they are indexed from 1 to N_s. This leads to the following equation for the probability of false-alarm:

$$\text{PFA} = 1 - \prod_{j=1}^{N_s} P(a_j < \zeta | H_0) \tag{6.21}$$

where

$$P(a_j < \zeta | H_0) = 1 - P(a_j > \zeta | H_0). \tag{6.22}$$

Next, we need to evaluate L_j for each cell j in the accumulator-matrix to be able to obtain $P(a_j < \zeta | H_0)$ for each. In order to do so, we follow a numerical method similar to the one introduced in [54].

Consider all points in the TF-space ($N_b \times M$) to be equally weighted (unit amplitude) and to have exceeded TF-threshold. Each TF-space point is then transformed into K cells in the HT-space. Without loss of generality, we consider our radar application as an appropriate example to understand and visualize the variation of L_j along the accumulator-matrix. For the echoes being reflected from cosmic ray induced air showers, the chirp rates of interest belong to the interval $\mathcal{K} = [-3, 0]$ MHz/μs. Also, the expected chirp intercept lies in the interval $[55, 70]$ MHz. In applying STFT, we consider 256-point DFT size with rectangular windowing and no overlapping between windows. Fig. 6.4 depicts the corresponding accumulator-matrix for the case of five nonoverlapping data blocks ($M = 5$) and $N_b = 17$. As observed, the contributions received by accumulator-matrix cells vary as the chirp slope varies, as well as the chirp intercept. We can see that accumulator-matrix cells receive less contributions as the chirp slope increases or the chirp intercept decreases, where for both cases less collinear points constitute the linear chirp in the TF-space.

As observed, this contribution varies from 1 to M. The cells that receive minimum contribution, $a_j = 1$, correspond to lines in TF-space that cannot exist so contribution results from one point. However, cells that receive maximum contribution, $a_j = 5$, correspond to lines with maximum number of collinear points in the TF-space. This is the number of time-blocks (M) per a single TF-space matrix.
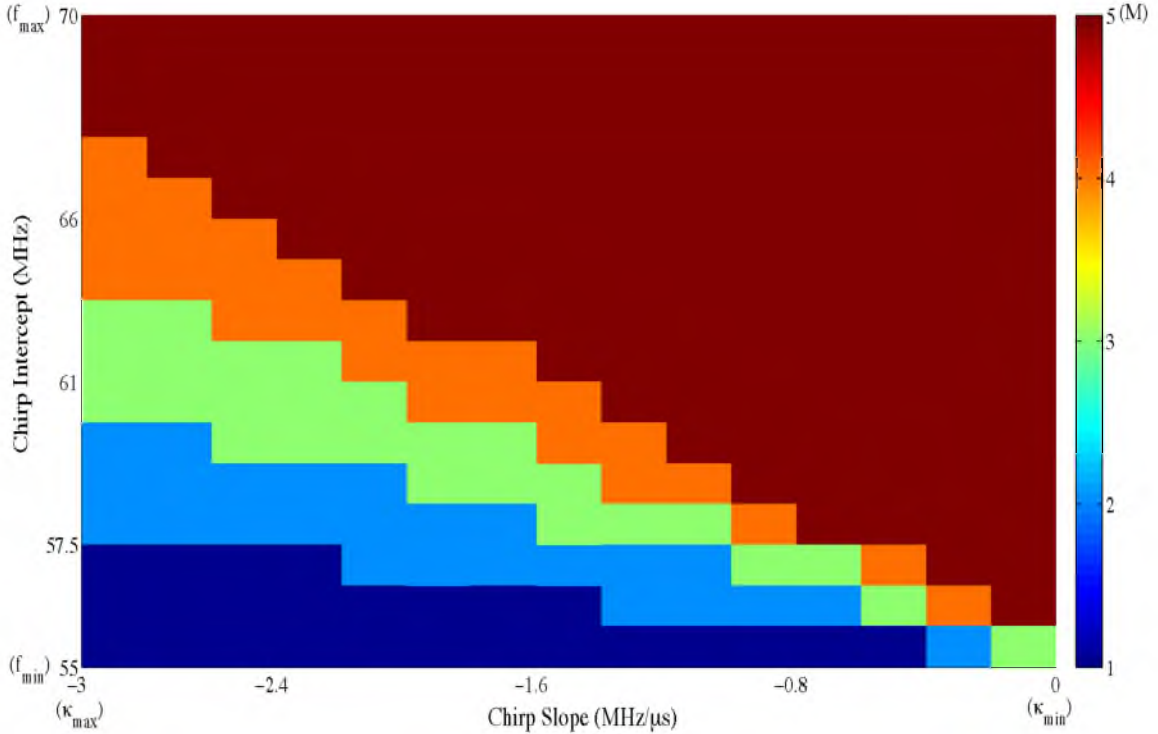
Figure 6.4: Accumulator-matrix for all points transformed from TF-space. Chirp intercept lies in the interval [55, 70] MHz and chirp rates of interest belong to the interval $\mathcal{K} = [-3, 0]$ MHz/μs. Two hundred and fifty six (256)-point DFT is used in generating the STFT.

For our detection system, as well as in other real-time applications, system user is more interested in evaluating the false-alarm rate (FAR) instead of the probability of false-alarm. FAR defines the average number of false detections, under chirp signal absence, per unit of time. Since we assume nonoverlapping TF-space matrices, FAR can be directly evaluated through the knowledge of probability of false-alarm simply by multiplying PFA and the number of processed TF-space matrices per second.

6.4.2 H_1: Chirp Signal Presence

In our analysis, we consider a particular chirp signal with known start and end frequencies f_H and f_L, respectively, and known chirp slope κ_c. We assume the time length of the TF-space matrix to be approximately the same as the chirp duration. Also, for a given range of the frequencies f_L to f_H, and the specified DFT length, the corresponding frequency indices assumed to be k_1 to k_2.

First, we wish to study the PDF of the amplitude peaks in the TF-space. Using a

rectangular window, the squared spectrum amplitude for the mth data block is

$$|X_n|^2 = |\sum_{i=0}^{N-1} x_{i,m} e^{-j2\pi n \frac{i}{N}}|^2, \quad n = k_1, k_1 + 1, \ldots, k_2 \qquad (6.23)$$

where $x_{i,m}$ contains the chirp signal $c_{i,m}$ and the additive noise $\nu_{i,m}$. Let C_n denote the DFT output due to $c_{i,m}$ and ν_n denote the DFT output due to $\nu_{i,m}$, hence, $X_n = C_n + \nu_n$. To arrive at a simple expression that facilitates the subsequent analysis of this section, we note that

$$\begin{aligned} \mathbb{E}\{|X_n|^2\} &= \mathbb{E}\{|C_n + \nu_n|^2\} \\ &= |C_n|^2 + \mathbb{E}\{|\nu_n|^2\} \end{aligned} \qquad (6.24)$$

where $\mathbb{E}\{\cdot\}$ denotes expectation. We replace the terms with the expectation sign on them by their instantaneous values. This leads to the approximation

$$|X_n|^2 \approx |C_n|^2 + |\nu_n|^2, \quad n = k_1, k_1 + 1, \ldots, k_2. \qquad (6.25)$$

We note that $|C_n|^2$ is determined by the known chirp signal. For a chirp signal, this is approximately a constant over the duration of the chirp [23]. We denote this constant by d. We also note that $|\nu_n|^2$ is a random variable with an exponential distribution, as discussed in Section 6.4.1.

Now we need to calculate the probability of a single-point's amplitude exceeding the TF-threshold, γ. For any given point of TF-space that is impacted by both noise and a chirp signal, one finds that

$$\begin{aligned} P_{\mathrm{d}} &= P(s > \gamma) \\ &= P((\nu + d) > \gamma) \\ &= \begin{cases} \int_{\gamma-d}^{\infty} e^{-\nu} d\nu, & \gamma > d \\ 1, & \text{otherwise.} \end{cases} \\ &= \begin{cases} e^{-(\gamma-d)}, & \gamma > d \\ 1, & \text{otherwise.} \end{cases} \end{aligned} \qquad (6.26)$$

In the TF-space matrix, of the M points that are affected by the chirp, l of them may exceed γ, in amplitude, and thus each is transformed to a line in the HT-space and, accordingly, accumulated. The location of the peak in the HT-space is determined through

the knowledge of the chirp intercept f_H and rate κ_c. The probability of the corresponding accumulator-matrix cell a_c exceeding ζ defines PCD and is evaluated as

$$
\begin{aligned}
\text{PCD} &= P(a_c > \zeta) \\
&= \sum_{l=1}^{M} P(\forall i : s_i > \gamma | H_1) \ P(a_c > \zeta | \{\forall i : s_i > \gamma\}).
\end{aligned}
\tag{6.27}
$$

Similar to (6.14), the first probability term can be written as

$$
P(\forall i : s_i > \gamma | H_1) = \binom{M}{l} P_d^l (1 - P_d)^{M-l}.
\tag{6.28}
$$

The second probability term can be evaluated as

$$
P(a_c > \zeta | \{\forall i : s_i > \gamma\}) = \int_{\zeta}^{\infty} P(a_c | \{\forall i : s_i > \gamma\}).
\tag{6.29}
$$

As in (6.16), the PDF of a single random variable s_i given that it has been affected by a chirp signal and exceeds γ may be written as

$$
\begin{aligned}
P(s_i | s_i > \gamma) &= \frac{P(s_i)}{P(s_i > \gamma)}, \quad s_i \in [\gamma, \infty) \\
&= \begin{cases} e^{-(s_i - \gamma)} u(s_i - \gamma), & \gamma > d \\ e^{-(s_i - d)} u(s_i - \gamma), & \text{otherwise.} \end{cases}
\end{aligned}
\tag{6.30}
$$

For a_c, similar to the noise analysis, we evaluate the convolution of l exponential variates which leads to a chi-squared distribution with $2l$ degrees of freedom.

$$
P(a_c | \{\forall i : s_i > \gamma\}) = \begin{cases} \dfrac{(a_c - l\gamma)^{l-1}}{(l-1)!} e^{-(a_c - l\gamma)} u(a_c - l\gamma), & \gamma > d \\[3mm] \dfrac{(a_c - ld)^{l-1}}{(l-1)!} e^{-(a_c - ld)} u(a_c - l\gamma), & \text{otherwise.} \end{cases}
\tag{6.31}
$$

Using the calculated PDF, the second probability term can be also computed as

$$P(a_c > \zeta | \{\forall i : s_i > \gamma\}) = \int_\zeta^\infty \begin{cases} \dfrac{(a_c - l\gamma)^{l-1}}{(l-1)!} e^{-(a_c - l\gamma)} u(a_c - l\gamma) \, da_c, & \gamma > d \\ \dfrac{(a_c - ld)^{l-1}}{(l-1)!} e^{-(a_c - ld)} u(a_c - l\gamma) \, da_c, & \text{otherwise.} \end{cases}$$

$$= \int_{\max(\zeta, l\gamma)}^\infty \begin{cases} \dfrac{(a_c - l\gamma)^{l-1}}{(l-1)!} e^{-(a_c - l\gamma)} \, da_c, & \gamma > d \\ \dfrac{(a_c - ld)^{l-1}}{(l-1)!} e^{-(a_c - ld)} \, da_c, & \text{otherwise.} \end{cases}$$

$$= \begin{cases} \displaystyle\int_{\max(\zeta - l\gamma, 0)}^\infty \dfrac{z^{l-1}}{(l-1)!} e^{-z} \, dz, & \gamma > d \\ \displaystyle\int_{\max(\zeta - ld, 0)}^\infty \dfrac{z^{l-1}}{(l-1)!} e^{-z} \, dz, & \text{otherwise.} \end{cases}$$

$$= u(\gamma - d) \left(u(l\gamma - \zeta) + u(\zeta - l\gamma) \frac{\Gamma(l, \zeta - l\gamma)}{(l-1)!} \right) +$$
$$u(d - \gamma) \left(u(ld - \zeta) + u(\zeta - ld) \frac{\Gamma(l, \zeta - ld)}{(l-1)!} \right) \tag{6.32}$$

Substituting (6.28) and (6.32) in (6.27), we get

$$\text{PCD} = \binom{M}{l} P_\text{d}^l (1 - P_\text{d})^{M-l} \left[u(\gamma - d) \left(u(l\gamma - \zeta) + u(\zeta - l\gamma) \frac{\Gamma(l, \zeta - l\gamma)}{(l-1)!} \right) + \right.$$
$$\left. u(d - \gamma) \left(u(ld - \zeta) + u(\zeta - ld) \frac{\Gamma(l, \zeta - ld)}{(l-1)!} \right) \right] \tag{6.33}$$

6.5 Numerical Analysis

Our objective in this section is to demonstrate the detection performance of the proposed detector. In addition, we present numerical results that confirm the validity of our formulated analytical expressions by comparing them with simulation results. In our study, two separate tests are performed. First, we evaluate the performance of the proposed detector under white-Gaussian noise. The goal from this test is to measure the probability of false-alarm acquired by the HT-based detector. Second, we measure the detection performance of the detector for different expected linear chirp signals versus SNR under a certain probability of false-alarm.

Before we proceed with the presentation of our numerical results, we make the following observations. It is clear from (6.21) and (6.33) that the detection performance of the proposed detector is a function of the pair of thresholds (γ, ζ). In designing our detector, we follow the constant false-alarm rate (CFAR) criterion by using an adaptive pair of thresholds (γ, ζ) that keep track of noise variations. Accordingly, (γ, ζ), in (6.21) and (6.33) expressions, can be replaced by their normalized pair (γ_0, ζ_0). Basically, a detection is declared, either

due to noise only or signal plus noise, whenever the accumulation sum of an HT-space's cell exceeds the defined HT-threshold ζ, while at least one TF-space cell has to have exceeded the defined TF-threshold γ.

System parameters are chosen as follows. The sample rate is 250 mega samples per second (MSPS). The choice of window length of the spectrogram is crucial as it provides a compromise between temporal and frequency resolution: a shorter window size means more temporal localization but less spectral discrimination. For a linear chirp signal of constant amplitude, using a rectangular window, the optimal window length is given by [51]

$$T_w = \sqrt{\frac{2}{|\kappa|}} \quad \text{seconds.} \tag{6.34}$$

In order to relate the mentioned formula to our application, we define the expected range of chirp slopes through the physical simulation of our radar target. We focus our interest on the most probabilistic interval [-3,-1] MHz/μs. Hence, replacing κ by its average value in (6.34). This leads to $T_w = 10^{-6}$. Given the sampling rate of 250 MSPS, this corresponds to 250 samples, which we round to 256 (the nearest power of 2). We consider the full frequency range for the intercept [0,125] MHz and [-3,-1] MHz/μs for the chirp slope with a step size of 0.2 MHz/μs. In addition, we consider signals of interest with fixed bandwidth 5 MHz, centered at 62.5 MHz. We present results of PFA and PCD for different SNR values in the range of [-25,10] dB.

6.5.1 Probability of False-Alarm (PFA)

Equation (6.21) provides an expression for the overall probability of false-alarm. As seen, it is a function of the maximum number of time-frequency points, L_j, TF-threshold $\gamma = \gamma_0 \eta$, and HT-threshold $\zeta = \zeta_0 \gamma$. Since L_j varies from one cell to another, probability of false-alarm per cell is cell dependent.

We plot probability of false-alarm for a single-cell case, which can be directly extended to the cell-matrix case or the whole accumulator-matrix. Fig. 6.5 shows the simulated and analytical result of PFA for a single-cell that corresponds to chirp intercept 65 MHz and chirp slope -1 MHz/μs. We see that the simulation results match the theoretical results perfectly for the single-cell case.

6.5.2 Probability of Correct Detection (PCD)

We start by looking at the detection efficiency of chirp signals with different chirp slopes. Fig. 6.6 presents the probability of detection versus SNR, for two distinct chirp slopes: -1 MHz/μs and -1.6 MHz/μs. Simulation results are plotted along with theoretical results
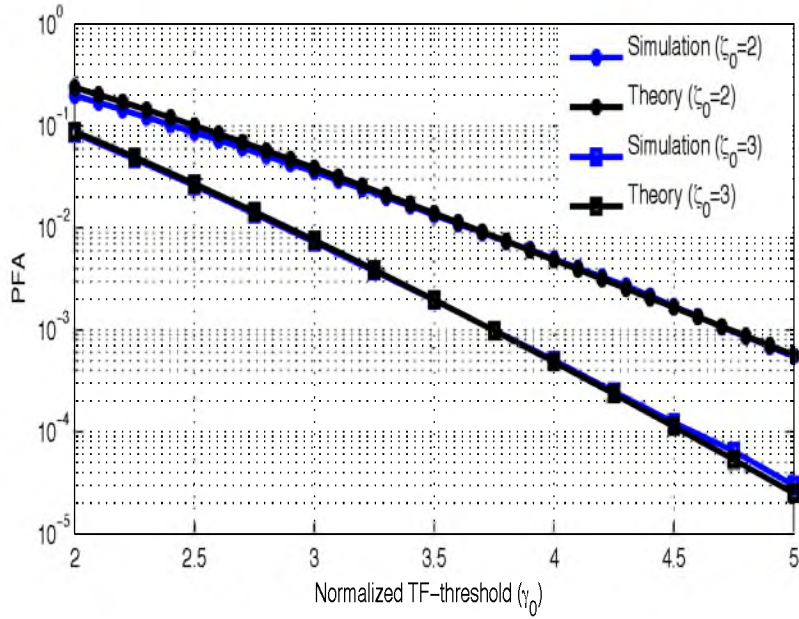
Figure 6.5: Probability of false-alarm for a single cell in the accumulator-matrix versus a range of TF-threshold values under two different HT-threshold values. Simulated and analytical results are plotted over white-Gaussian noise.
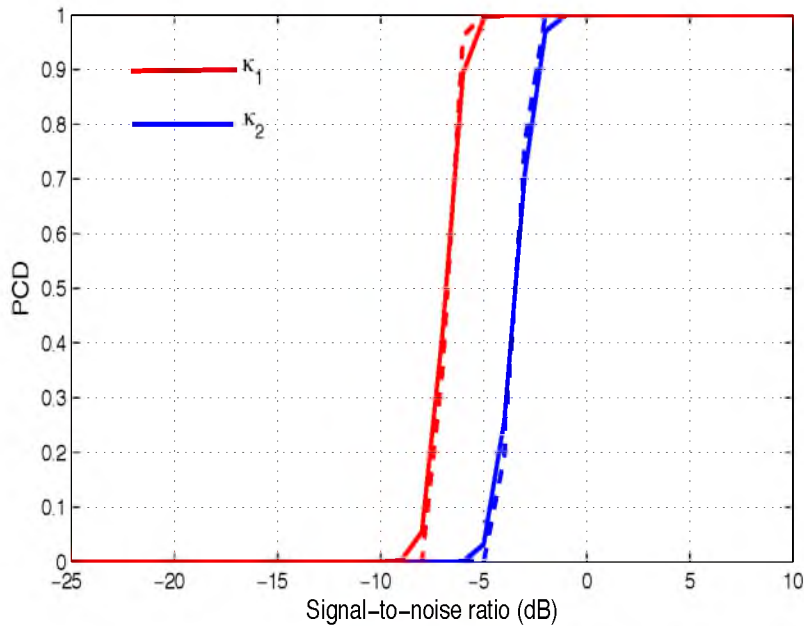
Figure 6.6: Probability of correct detection versus SNR for two distinct chirp slopes, where (κ_1, κ_2) equals (-1,-1.6) MHz/μs, respectively, under γ_0 equals 12 and ζ_0 equals 10. Simulated (dotted line) and analytical (solid line) results are plotted over AWGN.

based on the expression given in (6.33). These results clearly prove the validity of our theoretical calculations. Furthermore, we observe that PCD decreases as the chirp slope increases. This observation can be understood by noting that the higher the chirp slope is, the less will be the seed points that contribute to formation of the local peak in the accumulator-matrix.

Next, we perform two separate tests to understand the effect of varying the TF-threshold and the HT-threshold on the detection performance. First, we evaluate the detection performance of a linear chirp signal with a fixed slope (-1.6 MHz/μs) under different TF-threshold levels and a fixed HT-threshold level. The goal here is to estimate the expected deterioration in detection performance by raising the TF-threshold value. Fig. 6.7 presents PCD plots as a function of SNR for TF-threshold levels (7η,10η,13η) and fixed HT-threshold level (10γ). Again, these results show that theoretical calculations can perfectly track simulation results. As observed, the curves shift to the right 2 dB for each 3η units increase in the TF-threshold.

On the other hand, we evaluate the detection performance of a linear chirp signal with a fixed slope (-1.6 MHz/μs) under different HT-threshold levels and a fixed TF-threshold level. Fig. 6.8 presents PCD plots as a function of SNR for HT-threshold levels (7γ,10γ,13γ) and fixed TF-threshold level (10η). As observed, the curves shift to the right only 1 dB for
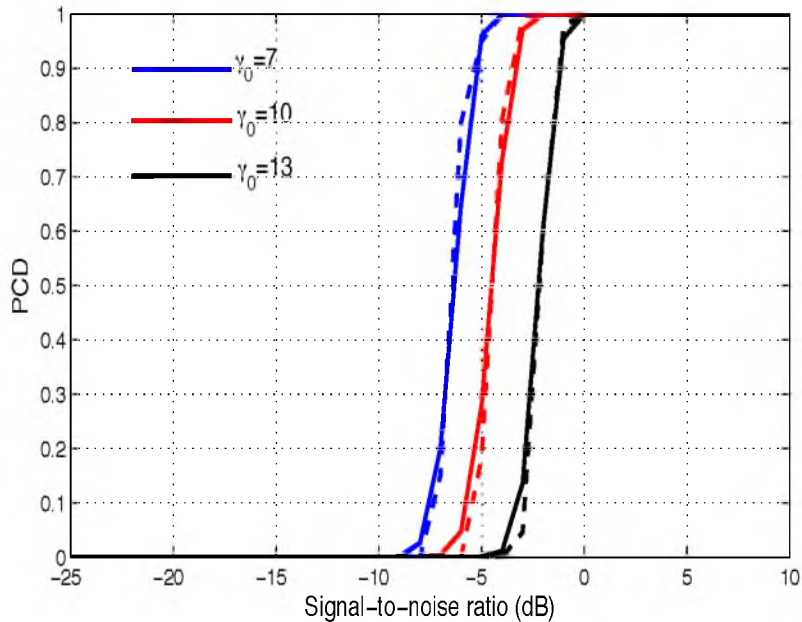
Figure 6.7: Probability of correct detection versus SNR for three different TF-threshold levels (7η,10η,13η) and fixed HT-threshold level (10γ). Simulated (dotted line) and analytical (solid line) results are plotted over AWGN.
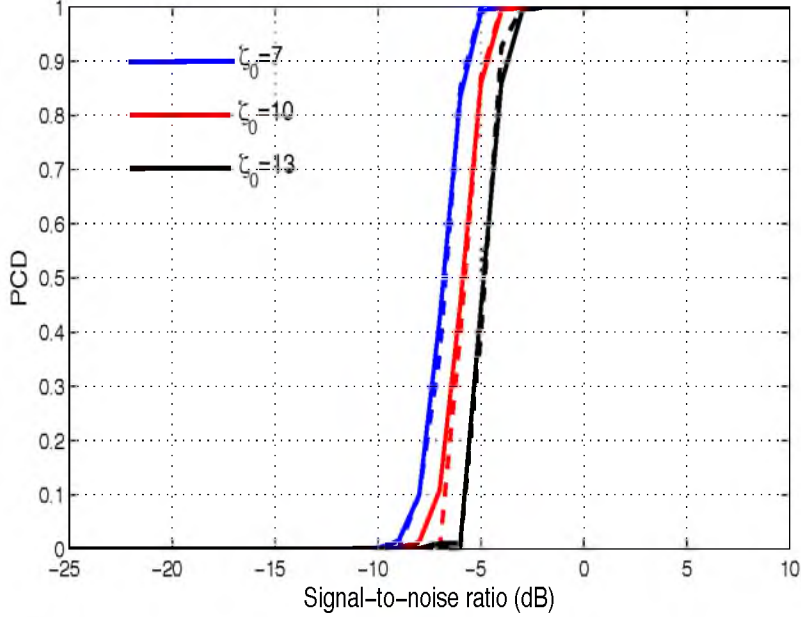
Figure 6.8: Probability of correct detection versus SNR for three different HT-threshold levels (7γ,10γ,13γ) and fixed TF-threshold level 10η. Simulated (dotted line) and analytical (solid line) results are plotted over AWGN.

each 3γ units increase in the HT-threshold. These results show that the TF-threshold has a larger effect on PCD than the HT-threshold.

6.5.3   Receiver Operating Characteristic

Fig. 6.9 shows the receiver operating characteristic (ROC) curves for the proposed detector. This set of curves show the calculated PCD of a linear chirp signal, with the rate of -1.6 MHz/μs, versus the FAR of the HT-based detector for a number of low received SNR values (-6 dB,-7 dB,-8 dB). Each point on each of the ROC curves corresponds to a specific pair of TF-threshold and HT-threshold values. In the plotted curves, the HT-threshold is fixed to 5γ and the TF-threshold is varied within [3η,15η].

As depicted in the figure, we can find a range of TF-threshold values [4.5η,6.5η] where FAR is in order 10^{-3} few events per hour or less, and at the same time, we can achieve complete probability of detection for the transmitted chirp at SNR of -7 dB.

6.6   Radar System Performance

Fig. 4.1 shows the basic elements of our bistatic radar system, located in Delta county, Utah. In building the transmitter station, we make use of analog television transmitters donated to University of Utah by Salt Lake City's KUTV Channel 2 and ABC4 [5]. The
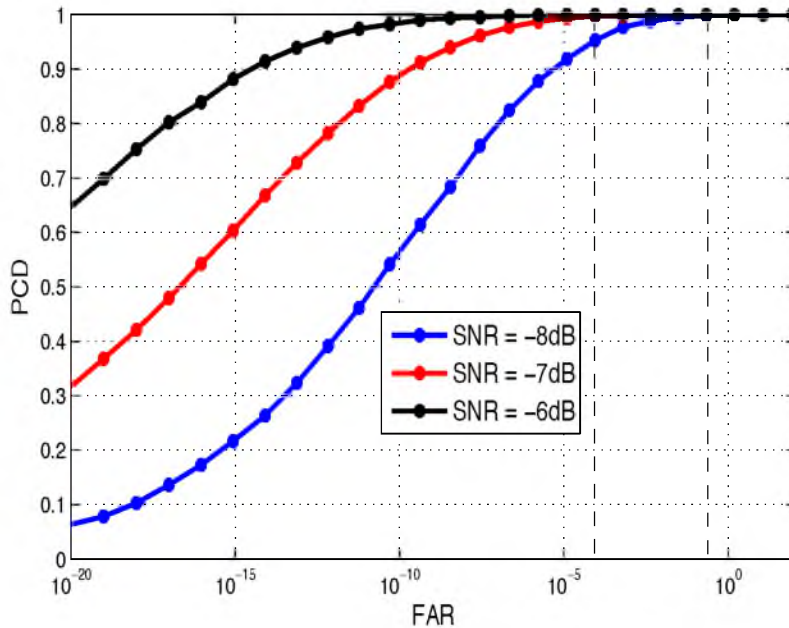
Figure 6.9: Empirical receiver operating characteristic (ROC) curves. Probability of correct detection is plotted versus false-alarm rate for different numbers of signal-to-noise ratio (SNR) levels.

transmitter station, operating under FCC license, broadcasts a continuous 54.1 MHz carrier signal with a 40 kW of power above the Telescope Array surface detectors. Also, our radar receiver station is placed at Long Ridge, 40 km distant from the transmitter site. We utilize the NI-5761 adapter module with a sample rate (F_s) equals 250 million samples per second (MSPS). Our system-on-chip design is implemented over the high performance Virtex-5 FPGA which is integrated with the fast PXIe interface for host connectivity. In our study, we consider experimental data acquired at the field using our bistatic radar receiver. We compare the performance of the proposed detector to our previously introduced rake-like receiver. For the rake-like receiver, we use an amplitude limiter to get rid of the impulsive noise. The amplitude limiter clips the amplitude of the received signal to a factor of k to its root mean square (RMS) value before clipping. This would allow us to bring the detection threshold of the LRT detector lower and thus, challenge the detection performance of the proposed HT-based detector.

For radar system testing, we conduct two basic performance tests through a series of radar measurements. First, we evaluate the performance of the proposed detector under the existing non-Gaussian environment. The goal from this test is to measure the probability of false-alarm (PFA) acquired by the HT-based detector. Second, we assess the detection performance of the proposed detector for a typical chirp signal versus SNR under a specified

pair of thresholds (γ, ζ) that corresponds to a reasonable level of PFA.

As we noted before, our radar system receives multiple undesirable frequency tones that might originate from different sources around the receiver unit, including the powerful radar carrier signal (54.1 MHz). Using the smart features of our detector, these persistent tones can be filtered out. In addition, since we know the band of interest, we apply a digital band-pass filter (60-65) MHz at the input stage of our detector for noise reduction and carrier suppression. Fig. 6.10 depicts the probability of false-alarm versus the TF-threshold γ for various HT-threshold values. In our second test, and due to rarity of radar echoes, we alternatively placed artificially-generated chirp signals in the same background for evaluating the detection performance. Fig. 6.11 depicts a sample of the acquired data after embedding a linear chirp signal of a typical slope (-1 MHz/μs) and -10 dB SNR value. For a fair comparison, we compare the detection performance of both detectors under PFA equals 10^{-3} and for a fixed bandwidth (5 MHz) chirps with center frequency, f_C, equal to 62.5 MHz. Fig. 6.12 shows performance comparison of both detectors. As depicted in Fig. 6.12, the minimum SNR for which complete detection is achieved is -4 dB for the HT-based detector and 8 dB for the LRT detector. This implies that HT significantly enhances detection by a factor of 14 dB. Using the amplitude limiter, the detection performance of the LRT detector is enhanced to a great extent, yet the HT-based detector outperforms by 2 dB.

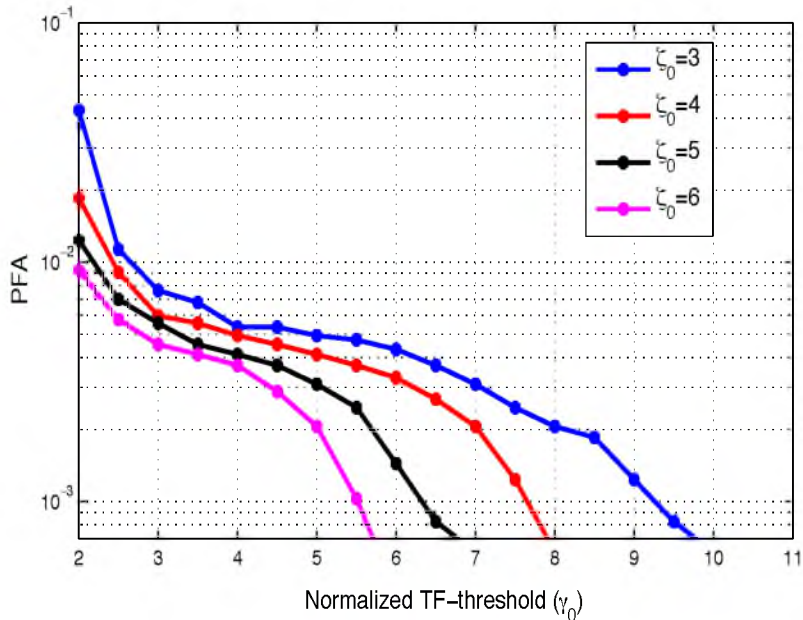**Figure 6.10**: HT detector: probability of false-alarm versus relative TF-threshold (γ_0 units of the averaged standard deviation of the entries in the TF-space matrix).
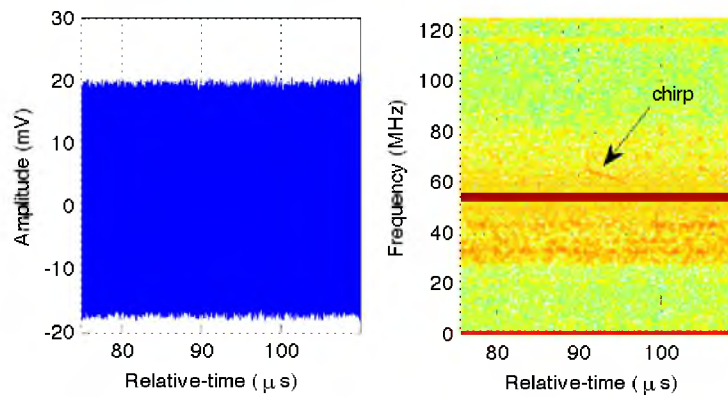
Figure 6.11: Linear chirp signal added to background noise.
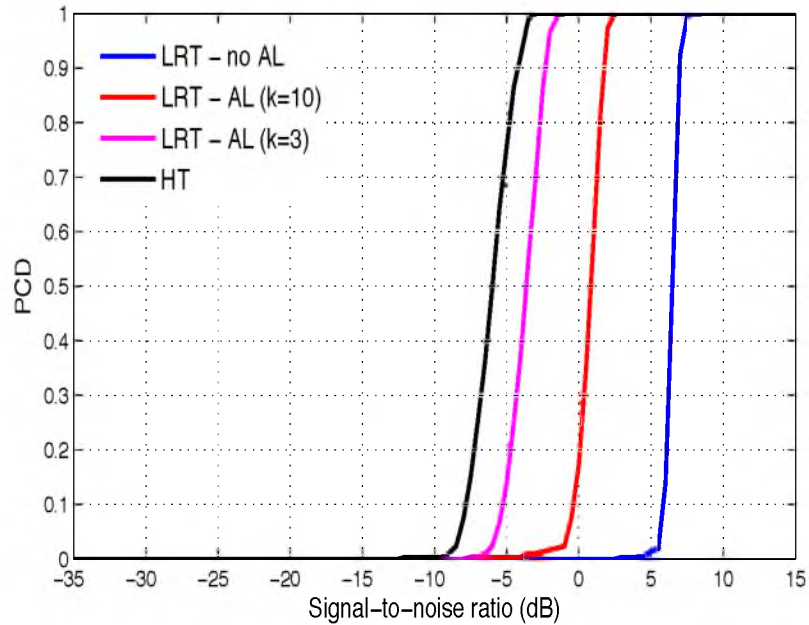
Figure 6.12: Probability of correct detection for HT-based detector and LRT detector with and without amplitude limiter under PFA equals 10^{-3}.

CHAPTER 7

CONCLUSIONS AND FUTURE WORK

In this final chapter, we present a summary for the contributions of this dissertation then we discuss future research directions that could provide the next steps along the path of this project.

7.1   Conclusions

Bistatic radar is a promising candidate as a remote-sensing technique for the observation of the highest energy cosmic-rays. These air showers are characterized by their wide bands (serveral tens of MHz), short duration ($\sim 10~\mu s$), and scarcity. This dissertation focuses on the problem of detection of reflected chirp echoes from the air showers. In this dissertation, we presented our research contributions.

We presented the detection of expected radar echoes using a rake-like receiver that consists of a bank of matched filters, matched to different chirp rates, in the range of interest. We also developed a mathematical framework for the design and analysis of the proposed detector. The noise background of the receiver is observed to be impulsive; this is considered a major source of positive false-alarms. In this regard, we introduced adding an amplitude limiter before the bank of matched filters to filter out the high amplitude spikes and thus, enable us to bring the threshold lower for an enhanced detection. Our results show that the system gains 6 dB of detection performance for a false-alarm rate of 2 Hz, by decreasing the amplitude limiter level by a factor of 3.

In addition, we presented a second detection method, based on Hough transform for detecting our radar received echoes that can also deal with the existing receiver environment which contains different spurious noises and nonstationary sources. We examined the detection capability of the detection structure through theoretical and numerical analysis.

Our introduced detection algorithms were implemented over a Virtex-5 FPGA. National Instruments modules were used as a high-performance custom hardware. Due to rarity of received echoes, we emulated the expected radar echoes to evaluate the system performance.

The detection performance of the emulated echoes was examined using the implemented receiver at the field. Also, we compared the resulting performance of both detectors.

As a member of TARA collaboration, I participated in the construction of the world's first bistatic radar observatory for Ultra-High Energy Cosmic Rays (UHECR). The TARA project represents the most ambitious effort to date to detect the radar signature of cosmic ray induced atmospheric ionization. The TARA detector is designed to search for unique cosmic ray radar echoes with very small radar cross sections (RCS). Specifically, the following key characteristics strongly reduce the minimum detectable RCS: high transmitter power (40 kW), high gain transmitting antenna, low noise radio frequency environment, broadband receiver antenna, and robust detection technique (rake-like receiver) that permits detection of signals 7 dB below the noise.

7.2   Future Work

A number of open problems still remain in our project. These problems suggest a variety of research directions that can be pursued in the context of the bistatic radar, which we are developing for remote sensing of cosmic ray induced air showers.

7.2.1   Transient Background

Background noise at the receiver site turns out to be impulsive and thus of a non-Gaussian nature. The main reason for this is that signal background may get disturbed by external interference sources with an impulsive nature that is well above the background level. These sources could be either natural such as lightening strikes, or man-made such as power-line communications or electric motors. In radar applications, the detection threshold may be raised in order to avoid the excess false-alarms that deteriorate the detection performance of the radar receiver. In this dissertation, we tackled this problem by either alleviating the effect of the transient background using an amplitude limiter or efficiently remove them from background using Hough transform. However, up till this point, we have not identified the source of the transient background which can help us in characterizing the nature of the major source of false-alarms. This future aspect could help us in achieving a lower level of false-alarms to keep storage low (from several gega bytes a day to several mega bytes a day) and thus, speed up offline processing of stored events.

7.2.2   Remote Receiver Station

In our bistatic radar application, remote receiving stations at several kilometers from the main primary receiver site are required. These remote sites would add stereoscopic

measurement capabilities which theoretically allow unique determination of air shower geometry and its core location. One of the major challenges when designing a remote station is power consumption, specifically when power stations may not be available. A typical solution is using solar energy which is expensive and may not even be feasible for higher power consumption systems. The current receiver DAQ system draws an average of 150 Watts which is relatively high and thus, cannot be used as a basis for building a remote receiver station. This would lead us to use a less efficient receiving units with lower power consumption, which shall degrade the efficiency of radar echoes detection. One future direction is power optimization of the current receiver DAQ system and probably moving towards a simpler embedded system that can help us in deploying remote stations.

7.2.3   Chirp Parameter Estimation

In the current phase of this project, we focus our interest on the detection of the received chirp echoes produced by cosmic ray induced air showers. However, once radar echoes are identified, the estimation of their parameters should be tackled. Since the related parameters of the received echoes are tied to the physical parameters of the air showers, this would give us an understanding to the air showers characteristics and the physics behind this high energy astrophysical phenomena.

APPENDIX A

FAR DERIVATION

By rearranging terms in (3.19), we get

$$r(t) = \cos\left(2\pi f_\mathrm{C} t\right) \frac{\sin\left(\kappa t \left(T_\kappa - |t|\right)\right)}{\pi \kappa t T_\kappa}. \tag{A.1}$$

Since we evaluate the second derivative of $r(t)$ around zero, (A.1) can be approximated as follows

$$r(t) \approx \cos\left(2\pi f_\mathrm{C} t\right) \frac{\sin\left(\kappa t T_\kappa\right)}{\pi \kappa t T_\kappa} \tag{A.2}$$

Using Taylor series expansion, (A.2) can be written as

$$r(t) = \left(\frac{1}{\pi \kappa t T_\kappa}\right) \left(1 - \frac{\left(2\pi f_\mathrm{C} t\right)^2}{2} + \cdots\right) \left(\pi \kappa t T_\kappa - \frac{\left(\pi \kappa t T_\kappa\right)^3}{6} + \cdots\right). \tag{A.3}$$

Hence, we are interested in evaluating the second derivative, higher order terms are neglected

$$r(t) = 1 - \frac{\left(2\pi f_\mathrm{C} t\right)^2}{2} - \frac{\left(\pi \kappa t T_\kappa\right)^2}{6} + \cdots \tag{A.4}$$

Thus

$$r''(t) = -\left(2\pi f_\mathrm{C} t\right)^2 - \frac{\left(\pi B\right)^2}{3} + \cdots \tag{A.5}$$

where $B = |\kappa| T_\kappa$.

APPENDIX B

GENZ INTEGRATION METHOD

Alan Genz [45] provided an integration method that simplifies the integral in (3.27). We follow his integration steps to transform the integration region to a unit hypercube $[0, 1]^{2N_0+1}$. We quote the integration steps from [45] and present it here in the text.

Since $\mathbf{R}$ is a covariance matrix, we can use Cholesky decomposition factorization $\mathbf{R} = \mathbf{L}\mathbf{L}^T$ and apply the change of variable $\mathbf{u} = \mathbf{L}^{-1}\mathbf{z}$ to simplify (3.27) as

$$\text{PMD} = \frac{1}{(2\pi)^{(2N_0+1)/2}} \int_{\alpha_{-N_0}}^{\beta_{-N_0}} e^{-u_{-N_0}^2/2} \cdots \int_{\alpha_{N_0}}^{\beta_{N_0}} e^{-u_{N_0}^2/2} d\mathbf{u} \tag{B.1}$$

where $d\mathbf{u}$ is the shorthand notation for $du_{N_0} \cdots du_0 \cdots du_{-N_0}$. $\mathbf{L}$ is a lower triangular matrix, and can be expressed as

$$\mathbf{L} = [l_{i,j}], \quad i = -N_0, \ldots, 0, \cdots, N_0; j = -N_0, \ldots, 0, \cdots, N_0. \tag{B.2}$$

Also

$$\alpha_i = \left(-\gamma - y_{c,i} - \sum_{j=-N_0}^{i-1} l_{i,j} u_j \right) / l_{i,i}, \quad i = -N_0 + 1, \ldots, 0, \cdots, N_0 \tag{B.3}$$

and

$$\beta_i = \left(\gamma - y_{c,i} - \sum_{j=-N_0}^{i-1} l_{i,j} u_j \right) / l_{i,i}, \quad i = -N_0 + 1, \ldots, 0, \cdots, N_0 \tag{B.4}$$

where

$$\alpha_{-N_0} = \left(-\gamma - y_{c,-N_0} \right) / l_{-N_0,-N_0} \tag{B.5}$$

and

$$\beta_{-N_0} = \left(\gamma - y_{c,-N_0} \right) / l_{-N_0,-N_0}. \tag{B.6}$$

Letting

$$s_i = \Phi(u_i) = \frac{1}{\sqrt{2\pi}} \int_{-\infty}^{u_i} e^{-\zeta^2/2} d\zeta, \quad i = -N_0, \ldots, 0, \cdots, N_0. \tag{B.7}$$

and using the Leibniz integral rule [55], we obtain

$$ds_i = \frac{1}{\sqrt{2\pi}} e^{-u_i{}^2/2} du_i, \quad i = -N_0, \ldots, 0, \cdots, N_0. \tag{B.8}$$

Using (B.7) and (B.8) in (B.1), we get

$$\text{PMD} = \int_{a_{-N_0}}^{b_{-N_0}} \int_{a_{-N_0+1}(s_{-N_0})}^{b_{-N_0+1}(s_{-N_0})} \cdots \int_{a_{N_0}\left(s_{-N_0},\cdots,s_{N_0-1}\right)}^{b_{N_0}\left(s_{-N_0},\cdots,s_{N_0-1}\right)} d\mathbf{s} \tag{B.9}$$

where $d\mathbf{s}$ is the shorthand notation for $ds_{N_0} \cdots ds_0 \cdots ds_{-N_0}$. Also,

$$a_i = \Phi\left(\left[-\gamma - y_{c,i} - \sum_{j=-N_0}^{i-1} l_{i,j}\Phi^{-1}(s_j)\right] / l_{i,i}\right), \quad i = -N_0+1, \ldots, 0, \cdots, N_0 \tag{B.10}$$

and

$$b_i = \Phi\left(\left[\gamma - y_{c,i} - \sum_{j=-N_0}^{i-1} l_{i,j}\Phi^{-1}(s_j)\right] / l_{i,i}\right), \quad i = -N_0+1, \ldots, 0, \cdots, N_0 \tag{B.11}$$

where

$$a_{-N_0} = \Phi\left((-\gamma - y_{c,-N_0})/l_{-N_0,-N_0}\right) \tag{B.12}$$

and

$$b_{-N_0} = \Phi\left((\gamma - y_{c,-N_0})/l_{-N_0,-N_0}\right). \tag{B.13}$$

Finally, in order to put the integrals into a constant limit form, the change of variable $s_i = b_i + (a_i - b_i)c_i$ is introduced. This reduces (B.9) to (3.28).

APPENDIX C

MONTE CARLO INTEGRATION
METHOD

The numerical computation of a multivariate normal probability is considered as a difficult computational problem. The reason behind the complexity of computation is attributed to dimensionality of the multivariate integral. In order to simplify the multivariate integral, we use Genzs integration methods [45]. These methods simplify the integration region and transform it to a unit hypercube, as we show in Appendix B.

Let us consider an integral I in N dimensions over volume V where V is an N-dimensional unit hypercube $[0,1]^N$. The basic premise is generating M random vectors $\mathbf{x}_i$ from flat distribution ($0 \leq \mathbf{x}_i \leq 1$), where $\mathbf{x}_i$ is an N-dimensional vector that samples the hypercube space. As M goes to ∞

$$\frac{V}{M} \sum_{i=1}^{M} f(\mathbf{x}_i) \to I \tag{C.1}$$

In our analysis, we use the subregion adaptive numerical integration algorithm, where a random vector $\mathbf{x}_i$ is generated for each loop iteration for a maximum number of iterations M or until the error of the Monte Carlo integration achieves a predefined tolerated value. The choice of M is a tradeoff between the integration accuracy and the computation time. Based on this method, the error is proportional to $(1/\sqrt{M})$ and independent of the dimensionality of the integral. The steps of the algorithm are presented in Table 3.1.

APPENDIX D

TARA RECEIVER ANTENNA

TARA expects signal with frequency less than 100 MHz. Due to noise below 30 MHz and the FM band above 88 MHz, the effective band is reduced to 30 to 88 MHz. This will be received by dual-polarized log periodic dipole antennas (LPDA). Each antenna channel is comprised of a series of five $\lambda/2$ dipoles. The ratio of successive dipole lengths is equal to the horizontal spacing between two dipoles (the defining characteristic of LPDA units), with the longest elements farthest from the feed-point to mitigate large group delay across the passband. Fig. D.1 shows a schematic of the receiver LPDA.

Receiver antenna gain is a factor in the bistatic radar equation that affects detection threshold. Numerical Electromagnetic Code was used in simulating the radiation pattern of the antenna to confirm directionality (see Fig. D.2). Simulated forward gain is 12.6 dBi and the vertical beam width is 23° at the carrier frequency, 54.1 MHz.
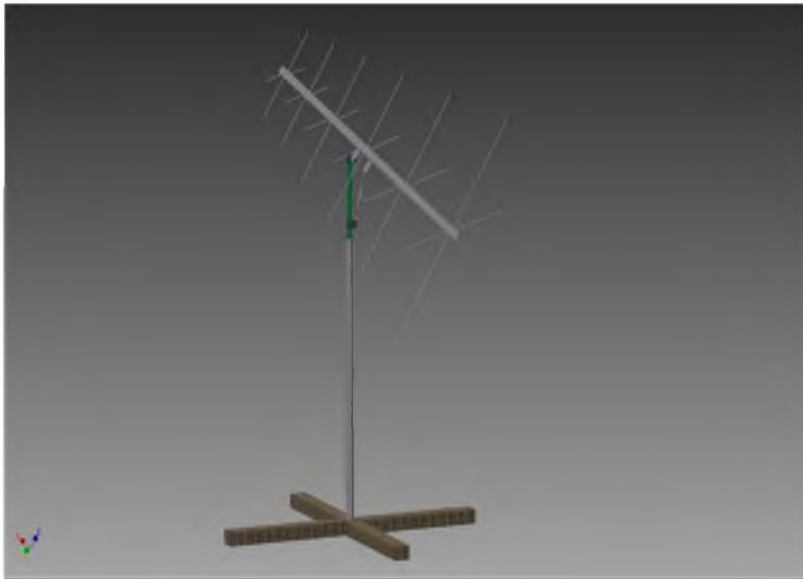

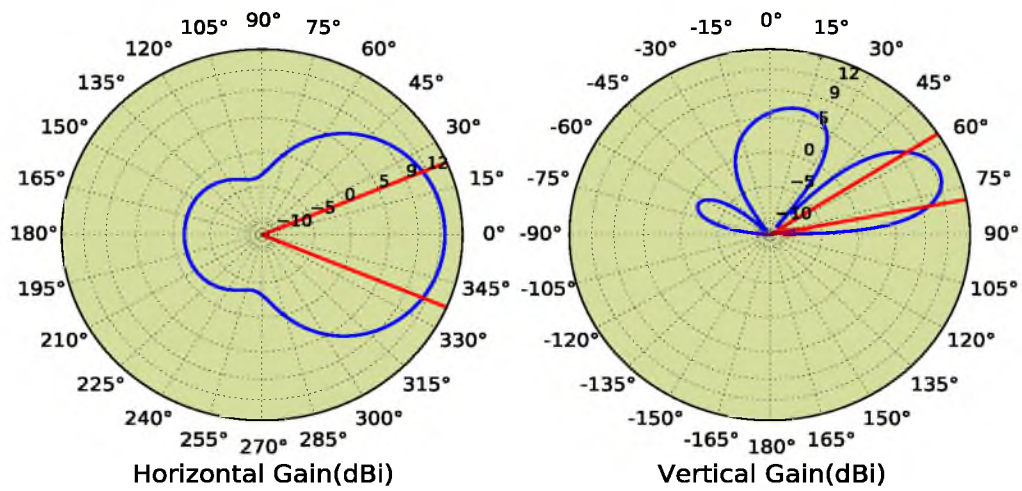**Figure D.1**: Dual polarized TARA log periodic dipole antenna.

Figure D.2: Simulated horizontal (left) and vertical (right) radiation patterns of a horizontally polarized TARA LPDA at the transmitter sounding frequency of 54.1 MHz. Beamwidths (3 dB below peak gain) are shown with red lines. Peak gain is 12.6 dBi.

APPENDIX E

TARA RF FRONT-END

There are three dual-polarization antennas at the receiver site, two of which are currently connected to the DAQ. RF signal from the antennas pass through a bank of filters and amplifiers. The components include an RF limiter (VLM-33-S+; Mini-Circuits), broad band amplifier, low pass filter (NLP - 100+; Mini-Circuits), high pass filter and an FM band stop filter (NSBP-108+; Mini-Circuits). Both polarizations from one antenna are filtered (41 MHz High Pass Filter, SHP-50+; Mini-Circuits) and amplified (40 dB, ZKL-1R5+; Mini-Circuits) at the antenna, where a bias tee (ZFBT-4R2G+; Mini-Circuits) is used to bring DC power from the control room. The second antenna's channels are filtered (27.5 MHz High Pass Filter, NHP-25+; Mini-Circuits) and amplified (30 dB, ZKL-2R5+; Mini-Circuits) inside the control room. The lightning arrestor (LSS0001; Inscape Data) minimizes damage to sensitive amplifiers by electric potentials that accrue during thunderstorms. The RF limiter prevents damage by transient high amplitude pulses.

Signal conditioning in the amplifier/filter banks is characterized by the transmission coefficient (Fig. E.1), known as S_{21}. Impedance mismatch relative to a 50 Ω transmission line, insertion loss for the various devices and gain from the amplifiers are combined in the S_{21} data. Of note in Fig. E.1 is the flat, high-gain (30 dB), broadband ($\simeq$ 40 MHz) pass-band necessary for Doppler-shifted radar echoes.
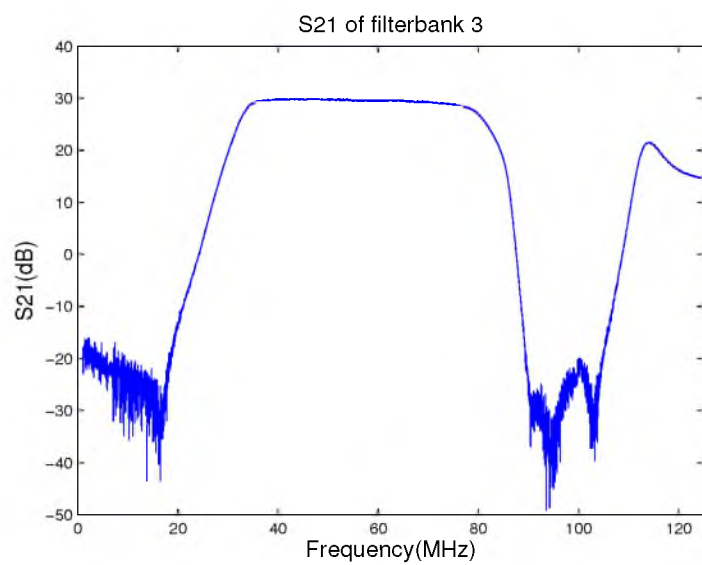
Figure E.1: S21 of Filterbank 3. Filterbank 3 is connected to the triggering channel of the FlexRIO.

APPENDIX F

RADAR ECHOES OF COSMIC RAY AIR SHOWERS

Cosmic rays (CR) with energies per nucleon in excess of $\approx 10^{14}$ eV [56,57] create cascades of particles with electromagnetic and hadronic components in the atmosphere, known as extensive air showers (EAS). Conventional cosmic ray experiments detect events through coincident shower front particles in an array of surface detectors or through fluorescence photons in the sky that radiate from the shower core [58–60].

As the shower core ionizes the atmosphere, liberated charges form a plasma with plasma frequency $\nu_p = (2\pi)^{-1}\sqrt{n_e e^2/m_e \epsilon_0}$, where n_e is the electron number density, e is the charge of the electron, and m_e is the electron mass. A shower is denoted *under-dense* or *over-dense* relative to the sounding frequency ν depending on whether n_e corresponds to $\nu_p > \nu$ or $\nu_p < \nu$. The radar cross-section (RCS) of the under-dense region is expected to be greatly attenuated due to collisional damping [61]. Therefore, we expect the dominant contribution to EAS RCS to be the over-dense case, which is modeled as a thin-wire conductor [62]. Fig. F.1 displays a typical EAS echo from simulation, where standard shower models of particle production and energy transport have been assumed.

The mechanism of radar echo detection of EAS differ from other radio applications. The target is small, and moving near the speed of light. Fig. F.2 depicts the bistatic radar geometry. We see that the radar echo has a phase shift because the total path length $L = R_T + R_R$ evolves slowly with time. The time-dependence of the path length causes the phase of the echo to evolve, while the transmitter maintains a constant frequency. The result is an echo that has a time-dependent frequency – a *chirp* signal [63] (Fig. F.1).

Chirp signals are ubiquitous in nature, although CR radar echos have very unique signatures. A simulation [64] has been designed that inputs CR energy, geometry and transmitter and receiver details, and which evolves an EAS while tracking the phase and amplitude of the radar echo. The simulation indicates that CR radar echoes are short
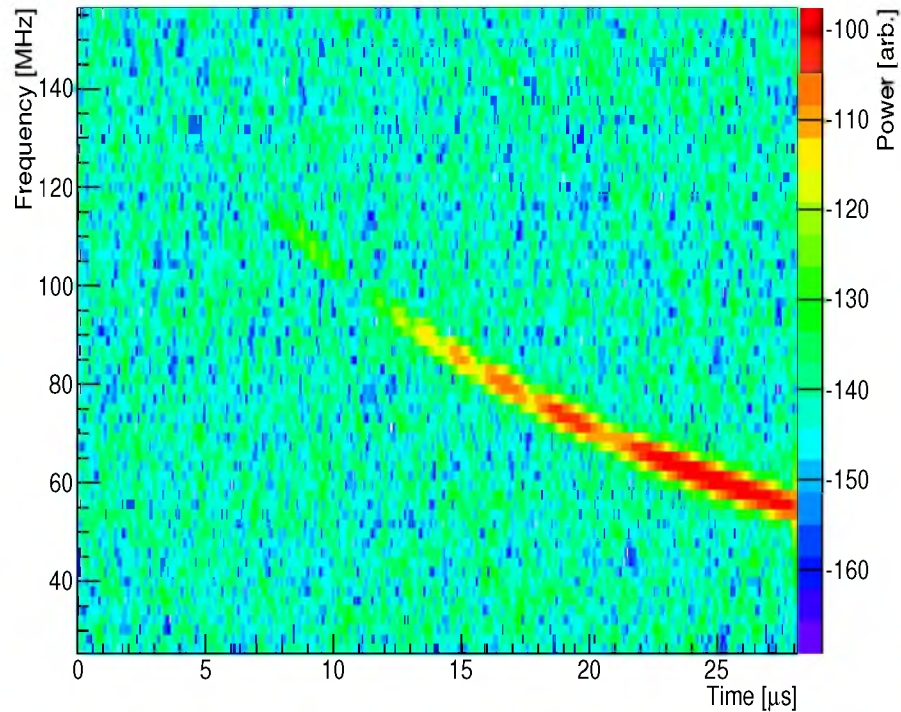
Figure F.1: Spectrogram of a chirp signal produced by the radar echo simulation for an EAS located midway between the transmitter and receiver with a zenith angle of 30° out of the transmitter-receiver plane. A weighted fit of this signal gives a -2.3 MHz/μs chirp slope. Color scale is power spectral density (PSD) given as dBm/Hz.

in duration (comparable to the shower life-time, $\approx$ 10 μs), have large chirp rates ($\approx$ -1 MHz/μs) and span a bandwidth of tens of MHz (see Fig. F.3 and Fig. F.4).

The energy and geometry of a distribution of 10000 cosmic rays detected at the TA surface detector array have been simulated. Fig. F.3 and Fig. F.4 show distributions of the chirp rate and duration for these events. Data obtained from the simulation have been used to guide the design of the receiver system, transmitter system and receiver antennas.
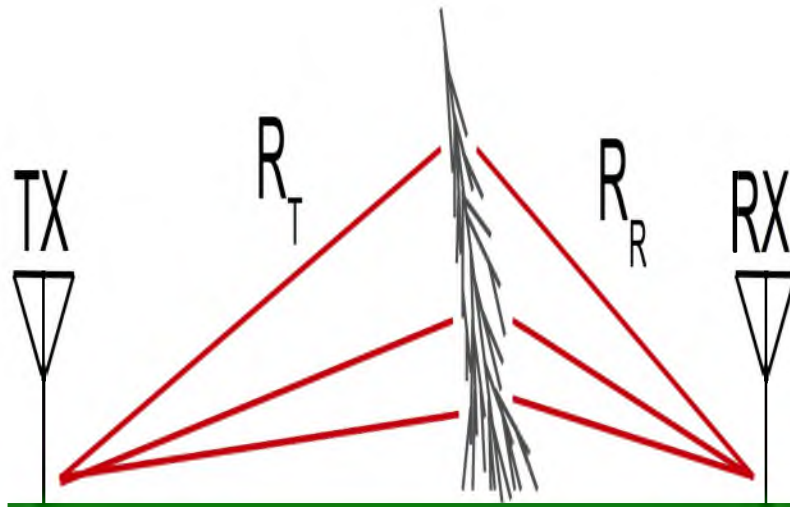
Figure F.2: Bistatic geometry of a radar sounding wave interrogating an EAS. R_T and R_R are the distances from transmitter (TX) to shower and shower to receiver (RX), respectively. The TX/RX antenna symbols represent location only. Actual antenna sizes are smaller than a pixel if represented to scale.
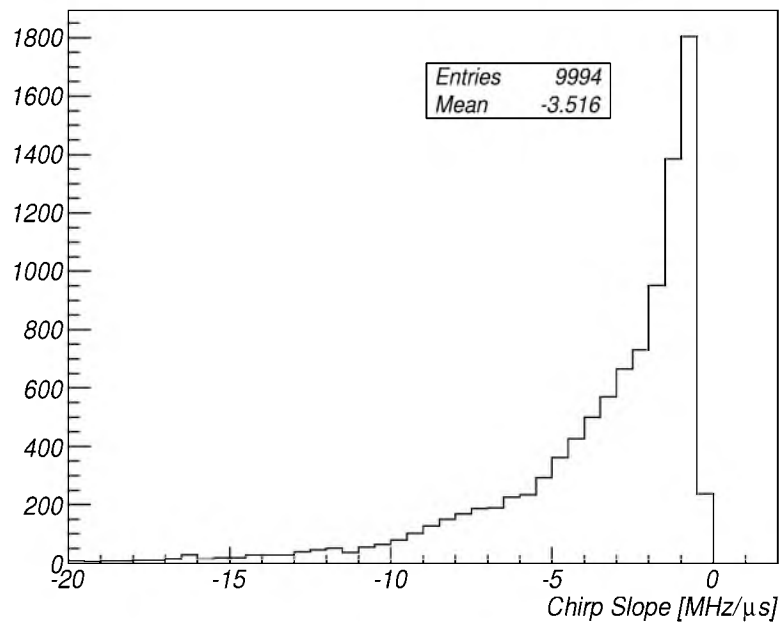
Figure F.3: Simulated chirp rate distribution from a set of 10000 TA cosmic ray events.
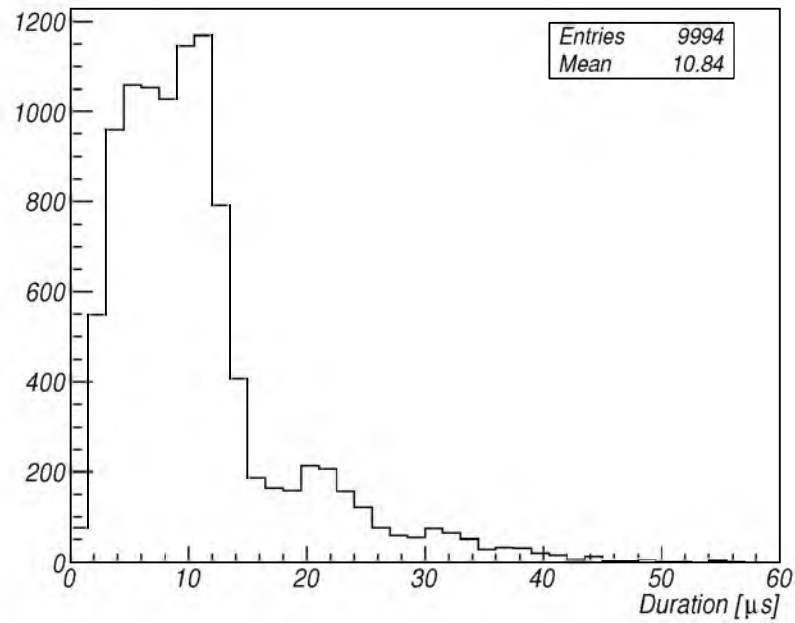
Figure F.4: Chirp duration distribution from a set of 10000 simulated radar echoes from TA cosmic ray events. Duration is defined as $d = t_1 - t_0$, where t_0 is the time when the maximum power is received and t_1 is the later time when the received power drops by 20 dB below the maximum, which approximates the end of the shower.

APPENDIX G

TARA RECEIVER DAQ

The receiver data acquisition (DAQ) system is a part of the Telescope Array RAdar (TARA) bistatic radar observatory for Ultra-High-Energy Cosmic Rays (UHECR). TARA is co-located with the Telescope Array, the largest conventional cosmic ray detector in the Northern Hemisphere, in radio quiet Western Utah. TARA employs an 8 MW effective radiated power (ERP) VHF transmitter and smart receiver system based on a 250 MS/s data acquisition system in an effort to detect the scatter of sounding radiation by UHECR-induced atmospheric ionization.

The National Instruments FlexRIO system provides an integrated hardware and software solution for a custom software defined radio DAQ. It is composed of three basic parts: adapter module, FPGA module and host controller (as shown in the lower box of Figure G.1). A description of each of these subsystems follows.

- Adapter Module

  The NI-5761 RF adapter module is a high-performance digitizer that defines the physical inputs and outputs of the DAQ system. It digitizes four analog input channels at a rate of 250 MS/s with 14-bit resolution. Eight TTL I/O lines are available for additional control, some of which are used in custom DAQ triggering schemes.

- FPGA Module

  The NI-7965R FPGA module is based on the PXI express platform that uses a Xilinx Virtex-5 FPGA with 128MB on board DRAM. FPGA design provides accurate timing and intelligent triggering. The PXI-express platform has a high-speed data link to the host controller.

- Host Controller

  The host controller is connected to the development machine, a Windows based computer, that uses the LabVIEW environment to design and compile FPGA code.
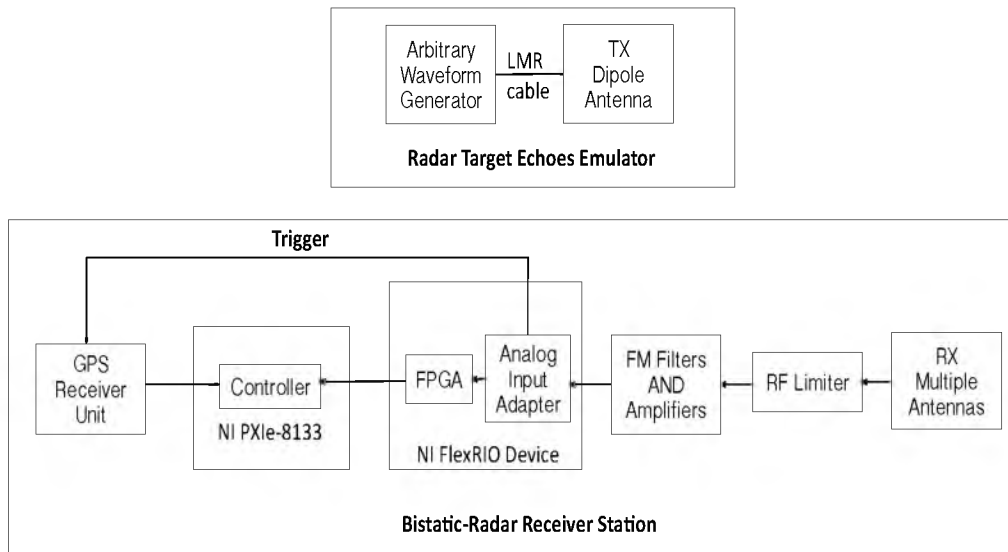
Figure G.1: Elements of the radar receiver station.

A host controller application, also designed in LabVIEW, runs on the development machine. It provides communication between the user space and the FPGA. In addition, a control application acquires data whenever received from FPGA and stores the data on disk.

G.1 DAQ implementation

The DAQ is designed to detect chirp echoes and confront the problem of nonstationary noise environment. Two antennas feed the DAQ's four input channels. Each antenna is a dual-polarized LPDA with one output channel each for horizontal and vertical polarization. Data are collected simultaneously from each of the four analog channels with one horizontal channel considered the triggering channel, then each channel is sampled using a 250 MS/s ADC (Texas Instruments; ADS62P49). Analog to digital conversion is followed by fast digital memory storage on the FPGA chip, which stores the incoming samples from each channel sequentially, in a 131 μs (32744 sample) continuous circular buffer such that data in each buffer are continually overwritten. Three distinct trigger modes are implemented: "snapshot trigger," "Fluorescence Detector (FD) external trigger," and "self-trigger." The details of each trigger are discussed in the following sections.

When a trigger occurs, the circular buffer information is sent to the host controller to be permanently stored on the computer's disk. A 320 μs dead-time is required to account for FPGA-host data transfer limitations, during which the DAQ cannot accept triggers. As depicted in Figure G.2, pre/posttrigger acquisition is set to 95 μs and 36 μs, respectively,
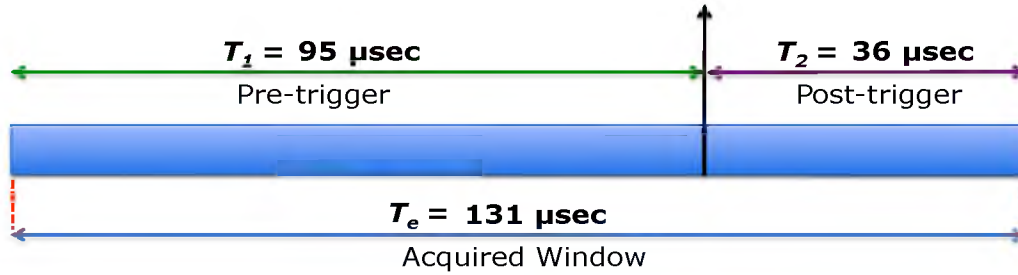
Figure G.2: Position of the triggering pulse within the data window that is written to disk.

to allow for jitter in the FD trigger timing (which turns out to be very small) and sufficient posttrigger data to see an entire echo wave form. A GPS time stamp is retrieved from a programmable hardware module [65] and recorded for each trigger with an absolute error of ±20 ns.

G.1.1 Snapshot Trigger

The snapshot trigger is an unbiased trigger scheme initiated once every minute that writes out an event to disk. The snapshot event will likely contain background noise only. These unbiased triggers are crucial for background noise estimation and analysis. A 125 MHz onboard clock is used to synchronize the snapshot triggers.

G.1.2 FD External Trigger

During active FD data acquisition periods, the Long Ridge FD (the location of the TARA receiver site) emits a NIM (nuclear instrumentation module) pulse for each low level trigger with a typical rate of ~ 3–5 Hz or much higher during FD calibration periods. The low level trigger is an OR of individual FD telescope mirror triggers. The FlexRIO is forced to trigger by each pulse received from the FD. Each FD run will result in hundreds of thousands of triggers which can be narrowed to ~ 100 events that coincide with real events found in reconstructed TA data. Dead time due to high FD-trigger rates are as high as several milliseconds during calibration periods. This does not reduce data acquisition time significantly because these periods occur only for several minutes and less than half a dozen times per FD data acquisition period. Further, FD operation only amounts to 10% duty cycle on average. The FlexRIO is forced to trigger by each pulse received from the FD. Each FD run will result in many thousands of triggers which can be narrowed to several events that coincide with real events found in reconstructed TA data.

G.1.3 Self-Trigger

For this trigger, one of the two presented methods in this dissertation is used as a solution for the problem of detecting radar chirp echoes in the non-Gaussian receiver background.

REFERENCES

[1] T. K. Gaisser, *Cosmic Rays and Particle Physics*, 1st ed. Cambridge University Press, January 1991.

[2] H. Tokuno, Y. Murano, S. Kawana, Y. Tameda, A. Taketa, D. Ikeda, S. Udo, S. Ogio, M. Fukushima, and R. Azuma, "On Site Calibration for New Fluorescence Detectors of the Telescope Array Experiment," *Nuclear Instruments and Methods in Physics Research Section A: Accelerators, Spectrometers, Detectors and Associated Equipment*, vol. 601, no. 3, pp. 364–371, 2009. [Online]. Available: http://linkinghub.elsevier.com/retrieve/pii/S0168900208021232

[3] Telescope array project. [Online]. Available: www.telescopearray.org

[4] J. J. Beatty, "The Pierre Auger Observatory Surface Detector Array," *Proc. SPIE 4858, Particle Astrophysics Instrumentation*, pp. 131–136, 2003. [Online]. Available: + http://dx.doi.org/10.1117/12.458541

[5] M. A. B. Othman, C. Allen, J. Belz, D. Besson, B. Farhang-Boroujeny, D. Ikeda, I. Kravchenko, S. Kunwar, J. Lundquist, I. Myers, T. Nakamura, H. Sagawa, P. Sokolsky, H. Takai, T. Terasawa, G. B. Thomson, and T. T. A. Collaboration, "Bistatic Radar Detection of UHECR with TARA," in *33rd International Cosmic Ray Conference*, Rio de Janeiro, 2013.

[6] N. J. Willis, *Bistatic Radar*, 2nd ed. SciTech Publishing, March 2005.

[7] M. A. B. Othman, J. Belz, and B. Farhang-Boroujeny, "Analysis of Matched Filter Performance in Detection of Nondeterministic Linear Chirp Signals," submitted to *IEEE Transactions on Aerospace and Electronic Systems*, forthcoming.

[8] M. A. B. Othman, I. Myers, J. Belz, and B. Farhang-Boroujeny, "Alleviating the Effect of Spurious Background for Detection Enhancement of Nondeterministic Chirp Signals," in *Radar Conference (RADAR), 2014 IEEE*, 2014, pp. 1–6.

[9] M. A. B. Othman, I. Myers, J. Belz, and B. Farhang-Boroujeny, "On Radar Detection of Chirp Signals with nondeterministic Parameters in Challenging Noise Background," in *Radar Conference (RADAR), 2013 IEEE*, 2013, pp. 1–6.

[10] R. Abbasi, M. A. B. Othman, C. Allen, L. Beard, J. Belz, D. Besson, M. Byrne, B. Farhang-Boroujeny, A. Gardner, W. Gillman, W. Hanlon, J. Hanson, C. Jayanthmurthy, S. Kunwar, S. Larson, I. Myers, S. Prohyra, K. Ratzlaff, P. Sokolsky, H. Takai, G. Thomson, and D. Von-Maluski, "Telescope Array Radar (TARA) Cosmic Ray Observatory," submitted to *Nuclear Instruments and Methods in Physics Research*, reviewed and accepted.

[11] M. A. B. Othman, J. Belz, and B. Farhang-Boroujeny, "Detection of Linear Chirps in non-Gaussian Noise Using Hough Transform," submitted to *IEEE Transactions on Aerospace and Electronic Systems*, forthcoming.

[12] M. A. B. Othman, C. Allen, J. Belz, D. Besson, B. FarhangBoroujeny, D. Ikeda, S. Kunwar, J. P. Lundquist, I. Kravchenko, I. Myers, T. Nakamura, H. Sagawa, P. Sokolsky, H. Takai, T. Terasawa, and G. B. Thomson, "Air Shower Detection by Bistatic Radar," *AIP Conference Proceedings*, vol. 1367, no. 1, 2011.

[13] M. A. B. Othman, C. Allen, J. Belz, D. Besson, B. Farhang-Boroujeny, D. Ikeda, I. Kravchenko, S. Kunwar, J. Lundquist, I. Myers *et al.*, "Radar Detection of UHECR Air Showers at the Telescope Array," *32nd International Cosmic Ray Conference, Beijing*, 2011.

[14] Belz, J., Othman, M. Abou Bakr, Allen, C., Barcikowski, E., Besson, D., Farhang-Boroujeny, B., Ikeda, D., Hanlon, W., Kunwar, S., Lundquist, J.P., Kravchenko, I., Larson, S., Myers, I., Nakamura, T., Rankin, J.S., Sagawa, H., Sokolsky, P., Takai, H., Terasawa, T., Thomson, G.B., and the TARA Collaboration, "TARA: Forward-Scattered Radar Detection of UHECR at the Telescope Array," *EPJ Web of Conferences*, vol. 53, p. 08012, 2013. [Online]. Available: http://dx.doi.org/10.1051/epjconf/20135308012

[15] R. Altes, "Echolocation as Seen from the Viewpoint of Radar/Sonar Theory," in *Localization and Orientation in Biology and Engineering*, ser. Proceedings in Life Sciences, D. Varj and H.-U. Schnitzler, Eds.   Springer Berlin Heidelberg, 1984, pp. 234–244.

[16] B. Askeland, H. Hobaek, and R. Mjelde, "Semiperiodic Chirp Sequences Reduce Autocorrelation Side Lobes of Pulsed Signals," *Geophysics*, vol. 73, no. 3, pp. Q19–Q27, 2008.

[17] M. Palmese, G. Bertolotto, A. Pescetto, and A. Trucco, "Experimental Validation of a Chirp-Based Underwater Acoustic Communication Method," *Proceedings of Meetings on Acoustics, Acoustical Society of America*, vol. 4, p. 6, 2008.

[18] P. D. Gupta, "Workshop on Gravitational Waves and Relativistic Astrophysics," *Indian Academy of Sciences - Journal of Physics*, vol. 63, no. 4, pp. 877–882, 2004.

[19] M. Barbu, E. Kaminsky, and R. Trahan, "Fractional Fourier Transform for Sonar Signal Processing," in *OCEANS, 2005. Proceedings of MTS/IEEE*, vol. 2, sept. 2005, pp. 1630 –1635.

[20] M. B. Charles E. Cook, *Radar Signals: An Introduction To Theory And Application.* Academic Press, 1967.

[21] A. Springer, W. Gugler, M. Huemer, L. Reindl, C. Ruppel, and R. Weigel, "Spread Spectrum Communications using Chirp Signals," in *EUROCOMM 2000. Information Systems for Enhanced Public Safety and Security. IEEE/AFCEA*, 2000, pp. 166 –170.

[22] M. Kowatsch and J. Lafferl, "A Spread-Spectrum Concept Combining Chirp Modulation and Pseudonoise Coding," *Communications, IEEE Transactions on*, vol. 31, no. 10, pp. 1133 – 1142, oct 1983.

[23] R. N. M. John C. Curlander, *Synthetic Aperture Radar: Systems and Signal Processing.* Wiley-Interscience, 1992.

[24] J. Xu, L. Durand, and P. Pibarot, "Nonlinear Transient Chirp Signal Modeling of the Aortic and Pulmonary Components of the Second Heart Sound," *Biomedical Engineering, IEEE Transactions on,* vol. 47, no. 10, pp. 1328 –1335, oct. 2000.

[25] J. Xu, Y. Peng, and X.-G. Xia, "Parametric Autofocus of SAR Imaging - Inherent Accuracy Limitations and Realization," *Geoscience and Remote Sensing, IEEE Transactions on,* vol. 42, no. 11, pp. 2397 – 2411, nov. 2004.

[26] P. H. Eichel, D. C. Ghiglia, and J. C. V. Jakowatz, "Speckle Processing Method for Synthetic-Aperture-Radar Phase Correction," *Optical Letters,* vol. 14, pp. 1–3, January 1989.

[27] O. Machhi and N. Bershad, "Adaptive Recovery of a Chirped Sinusoid in Noise. I. Performance of the RLS Algorithm," *Signal Processing, IEEE Transactions on,* vol. 39, no. 3, pp. 583 –594, mar 1991.

[28] N. Bershad and O. Macchi, "Adaptive Recovery of a Chirped Sinusoid in Noise. II. Performance of the LMS Algorithm," *Signal Processing, IEEE Transactions on,* vol. 39, no. 3, pp. 595 –602, mar 1991.

[29] P. Tichavsky and P. Handel, "Two Algorithms for Adaptive Retrieval of Slowly Time-Varying Multiple Cisoids in Noise," *Signal Processing, IEEE Transactions on,* vol. 43, no. 5, pp. 1116 –1127, may 1995.

[30] P. Wei, J. Han, J. Zeidler, and W. Ku, "Comparative Tracking Performance of the LMS and RLS Algorithms for Chirped Narrowband Signal Recovery," *Signal Processing, IEEE Transactions on,* vol. 50, no. 7, pp. 1602–1609, 2002.

[31] S. To, B. Siahamis, and L. Sciacca, "Digital Implementation Issues in a Pulse Compression Radar System," in *Information, Decision and Control, 1999. IDC 99. Proceedings. 1999,* 1999, pp. 181–186.

[32] M. B. Charles E. Cook, *Radar Signals: An Introduction to Theory and Application,* 1st ed. Academic Press, 1967.

[33] S. M. Kay, *Fundamentals of Statistical Signal Processing, Volume II: Detection Theory,* 1st ed. Prentice Hall, 1998.

[34] S. A. Kassam and J. B. Thomas, *Signal Detection in Non-Gaussian Noise (Springer Texts in Electrical Engineering),* 1st ed. Springer, December 1987.

[35] C. R. Cahn, "A Note on Signal-to-Noise Ratio in Band-Pass Limiters," *Information Theory, IRE Transactions on,* vol. 7, no. 1, pp. 39–43, January 1961.

[36] M. Malanowski and K. Kulpa, "Robust Detection in Continuous-Wave Noise Radar - Experimental Results," in *Radar Symposium (IRS), 2010 11th International,* June 2010, pp. 1–4.

[37] J. Van Vleck and D. Middleton, "The Spectrum of Clipped Noise," *Proceedings of the IEEE,* vol. 54, no. 1, pp. 2–19, Jan 1966.

[38] B. Chen and P. Willett, "Detection of Hidden Markov Model Transient Signals," *Aerospace and Electronic Systems, IEEE Transactions on*, vol. 36, no. 4, pp. 1253 – 1268, October 2000.

[39] T. Luginbuhl and P. Willett, "Tracking a General, Frequency Modulated Signal in Noise," in *Decision and Control, 1999. Proceedings of the 38th IEEE Conference on*, vol. 5, 1999, pp. 5076 –5081.

[40] B. Carlson, E. Evans, and S. Wilson, "Search Radar Detection and Track with the Hough transform. I. System Concept," *Aerospace and Electronic Systems, IEEE Transactions on*, vol. 30, no. 1, pp. 102 –108, January 1994.

[41] J. Roger L. Easton, A. J. Ticknor, and H. H. Barrett, "Two-Dimensional Complex Fourier Transform via the Radon Transform," *Appl. Opt.*, vol. 24, no. 22, pp. 3817–3824, Nov 1985. [Online]. Available: http://ao.osa.org/abstract.cfm?URI=ao-24-22-3817

[42] J. Xu, J. Yu, Y.-N. Peng, and X.-G. Xia, "Radon-Fourier Transform for Radar Target Detection, I: Generalized Doppler Filter Bank," *Aerospace and Electronic Systems, IEEE Transactions on*, vol. 47, no. 2, pp. 1186–1202, 2011.

[43] I. Gradshteyn and I. Ryzhik, *Table of Integrals, Series, and Products*, 7th ed. Academic Press, 2007.

[44] M. R. Leadbetter, G. Lindgren, and H. Rootzén, *Extremes and Related Properties of Random Sequences and Processes*, 1st ed. Springer-Verlag, 1983.

[45] F. B. Alan Genz, *Computation of Multivariate Normal and t Probabilities*. Springer, 2009.

[46] J. Berntsen, T. O. Espelid, and A. Genz, "An Adaptive Algorithm for the Approximate Calculation of Multiple Integrals," *ACM Trans. Math. Softw.*, vol. 17, no. 4, pp. 437–451, Dec. 1991. [Online]. Available: http://doi.acm.org/10.1145/210232.210233

[47] J. Illingworth and J. Kittler, "A Survey of the Hough Transform," *Computer Vision, Graphics, and Image Processing*, vol. 44, no. 1, pp. 87 – 116, 1988. [Online]. Available: http://www.sciencedirect.com/science/article/pii/S0734189X88800331

[48] P. V. C. Hough, "A Method and Means for Recognizing Complex Patterns," *U.S. Patent 3,069,654*, 1962.

[49] S. H. Nawab and T. F. Quatieri, *Advanced Topics in Signal Processing*, J. S. Lim and A. V. Oppenheim, Eds. Upper Saddle River, NJ, USA: Prentice-Hall, Inc., 1987. [Online]. Available: http://dl.acm.org/citation.cfm?id=42739.42745

[50] D. Gabor, "Theory of Communication," *J. IEEE*, vol. 93(III), pp. 429–457, November 1946.

[51] B. Imberger, Jorg; Boashash, "Application of the Wigner-Ville Distribution to Temperature Gradient Microstructure: A New Technique to Study Small-Scale Variations," *J. of Physical Oceanography*, vol. 16, pp. 1997–2012, December 1986.

[52] A. Papoulis and S. Pillai, *Probability, Random Variables, and Stochastic Processes*, ser. McGraw-Hill series in electrical engineering: Communications and Signal Processing. Tata McGraw-Hill, 2002. [Online]. Available: http://books.google.com/books?id=g6eUoWOlcQMC

[53] H. O. Lancaster, *The Chi-squared Distribution.* John Wiley and Sons Inc, 1969.

[54] B. Carlson, E. Evans, and S. Wilson, "Search Radar Detection and Track with the Hough transform. II. Detection Statistics," *Aerospace and Electronic Systems, IEEE Transactions on*, vol. 30, no. 1, pp. 109–115, January 1994.

[55] M. Abramowitz and I. A. Stegun, *Handbook of Mathematical Functions with Formulas, Graphs, and Mathematical Tables*, 9th ed. New York: Dover, 1964.

[56] A A Watson, "High Energy Cosmic Rays and the Greisen-Zatzepin-Kuzmin Effect," *Reports on Progres in Physics*, vol. 76, no. 10, 2013.

[57] Kampert, K., Unger, M., "Measurements of the Cosmic Ray Composition with Air Shower Experiments," *Astroparticle Physics*, vol. 35, no. 10, 2012.

[58] T. Abu-Zayyad et. al., "The Surface Detector Array of the Telescope Array Experiment," *Nucl. Instr. Meth. Phys. Res. A*, vol. 689, no. 0, pp. 87 – 97, 2012.

[59] Budnev et. al, "The Tunka Experiment: Towards a 1-km-square EAS Cherenkov Light Array in the Tunka Valley," *International Journal of Modern Physics A*, vol. 20, no. 29, 2005.

[60] The Pierre Auger Collaboration, "Correlation of the Highest-Energy Cosmic Rays with Nearby Extragalactic Objects," *Science*, vol. 318, no. 5852, 2007.

[61] Vidmar, R.J., "On the Use of Atmospheric Pressure Plasmas as Electromagnetic Reflectors and Absorbers," *IEEE Transactions in Plasma Science*, vol. 18, no. 4, 2002.

[62] Gorham, P., "On the Possibility of Radar Echo Detection of Ultra-High Energy Cosmic Ray - and Neutrino - Induced Extensive Air Showers," *Astroparticle Physics*, vol. 15, no. 2, 2001.

[63] D. G. Underwood, "Large Doppler shift in Radar Detection of Ultra-High Energy Cosmic Rays," in *Radar Conference, 2008. RADAR '08. IEEE*, May 2008, pp. 1–5.

[64] H. Takai et. al., "Forward Scattering Radar for Ultra High Energy Cosmic Rays," in *Proceedings of the 32nd International Cosmic Ray Conference*, 2011.

[65] J. D. Smith, J. R. Thomas, S. B. Thomas, and et al., "GPSY2: A Programmable Hardware Module for Precise Absolute Time Event Generation and Measurement," *International Cosmic Ray Conference*, vol. 5, pp. 997–1000, 2008.